Medium Energy Gamma Rays Following Radiative Capture of Polarized Protons on Light Nuclei at Ep = 40, 50, and 65 MeV

Masaharu Noumachi

Radiative capture reactions are very powerful for studying nuclear properties and reaction mechanisms, since the electro-magnetic interaction involved in the process is simple and well known. So far low energy γ-rays with E_γ=10~30 MeV have extensively been studied mainly to investigate E1 giant resonances.

The present work is concerned with higher energy γ-rays with E_γ=30~80 MeV beyond the E1 giant resonance energy. Thus the radiation mechanism is considered to be a direct capture mechanism. Experimental study of the medium energy γ-rays has, so far, not been extensive since probability of emitting such γ-rays is very small.

Recently we had succeeded in developing a special NaI ensemble called HERMES (high energy gamma radiation measuring system). It gave fairly clean spectra for lower energy γ-rays (20~30 MeV). However in order to measure the medium energy γ-rays, some improvements were required on the data acquisition system and its data processing to derive clean spectra.

The new data acquisition system was successfully developed in this work. This system is very powerful not only for the HERMES but also for general uses for both multi-detector correlation measurements and multi-parameter detector measurements.

The neutron rejection, the cosmic ray rejection and the pile-up rejection were improved much so as to make the severe event selection possible. Thus sufficient energy resolution and S/N ratio were achieved for medium energy γ-ray measurements.

The medium energy radiative capture reactions on ^{11}B and ^{12}C were studied by using the polarized protons with Ep = 40-65 MeV. Discrete γ-rays

feeding the ground 0^+, 4.44 MeV 2^+, and 9.64 MeV 3^- states in ^{12}C were identified for the $^{11}B(p,\gamma)^{12}C$ reaction. The peaks corresponding to the ground $1/2^-$, and the doublet of 3.51 MeV $3/2^-$ and 3.55 MeV $5/2^+$ peaks in ^{13}N were identified for the $^{12}C(p,\gamma)^{13}N$ reaction. Since the spectrum was much improved in both the energy resolution and the S/N ratio, prominent γ-ray peaks feeding the 19 and 22 MeV excitation regions in ^{12}C were observed. The $d_{3/2}(p_{3/2})^{-1}$ component in ^{12}C at the excitation energy region around the 22 MeV was first observation in the (p,γ) reaction. The angular dependences of both the differential cross sections and the analyzing powers for these capture γ-rays with E_γ = 40-80 MeV were measured for the first time.

The angular distributions of these γ-rays show a similar forward-peaking pattern, being rather independent of the final state configurations. This fact is considered that the transition is mainly of the stretched E1 $(j+1\rightarrow j)$ multipole with appreciable admixture of the stretched E2 $(j+2\rightarrow j)$ multipole.

On the other hand the angular dependences of the analyzing powers are found to be much affected by the microscopic configurations of the final states. The radiative capture γ-rays feeding low-lying states with known configurations show following common features. The analyzing powers of the γ radiations to the j-upper particle states $(j=l+1/2)$ increase with the increasing detection angle θ_γ, while those to the j-lower particle states $(j=l-1/2)$ decrease with the increasing θ_γ. The angular dependences of the analyzing powers for highly excited states are consistent with what one would expect from the systematic feature observed for the γ-rays to the low-lying states and from the microscopic configurations of the highly excited states which are studied by other reactions and RPA calculations.

The author would like to thank Professor H. Ejiri for suggesting this work in the early stage. He also expresses his sincere gratitude to Professor H. Ejiri under whose guidance and encouragement this work was carried out. The author is deeply indebted to Dr. T. Shibata for valuable discussions and collaboration in all stages of the experiment. The author is also indebted Drs. K. Okada, T. Motobayashi and T. Kishimoto for their excellent collaborations and valuable discussions. The author would like to thank Dr. M. Sasao and Mr. K. Tsujita for the improvement of the HERMES and the collaboration in the early stage of this work. The author is deeply indebted to Mr. I. Sugai of INS for preparation of the ^{11}B target, Professor H. Kitazawa for the theoretical discussion, and Dr. F. Ohtani for the valuable discussion about a beam polarimeter and his collaboration.

The author is indebted to Professor H. Ogata, Dr. R. Hayano and Dr. J. Chiba for kindly supplying their soft-ware products and for discussion about data acquisition systems.

Thanks are due to all members of Ejiri's institute for many aspects of this work. Many thanks are also due to the RCNP cyclotron crew for the cyclotron operation under the program numbers 13A09, 14A16 and 15A14.

CONTENTS

1.1 Medium energy radiative capture reaction.

Radiative capture reactions have extensively been used to study nuclear properties. Since the electro-magnetic force is simple and a long wave-length approximation is valid for most of nuclear γ-rays, the interaction involved in the radiative capture process is well defined. Thus the study of the radiative capture reaction is useful for investigating properties of nuclear wave functions associated with both the initial and final states.

Low energy γ-rays with energies below about 30 MeV have extensively been studied(BR72, GL72, SN77, MA81, SA79) mainly to investigate the electric dipole giant resonance (E1-GR)(BR64). Detailed structure of E1-GR has been studied by measuring the excitation function of the radiative capture process. Electrostatic accelerators with good energy resolution are suitable for this study. In these measurements, lower partial waves dominate the entrance channel, because the spin of the low-lying final state is small and the γ-ray cannot take away a large angular momentum.

A simple radiative nucleon capture model assumes that the incoming nucleon undergoes a radiative transition from its scattering state into one of the single-particle orbits in the residual nucleus (see Fig. 1.1a). Thus the radiation is limited to a single particle transition in this simple direct capture model. However, the direct capture process only is not the major process for the radiative capture through the GR, because the E1-GR is a kind of collective states when the incident proton energy is allowed to excite the E1-GR by the radiative capture process. Thus more relevant model in that case is a direct-semidirect (DSD) model, where excitation of the GR is included as the intermediate stage of the process (see Fig. 1.1b).

Therefore, the highly excited state of the E1-GR excitation region are

studied as the entrance channel of the reaction by these measurements.

Medium energy γ-rays with energies of 40-100 MeV have not been well studied. Since the energy region is so far beyond the E1-GR energy, the radiative capture shows features of a direct reaction. Only a few works of the radiative capture reactions (KO79) have been made so far in the medium energy region of 40-80 MeV, although some relevant informations have been obtained from studies of the inverse reaction, namely the photonuclear reaction. The medium energy radiative capture process may show new features of γ radiation mechanism and single particle configurations of highly-excited states.

A simple direct capture (one-body capture) probability for incident nucleons into definite orbits decreases with the increasing energy of the incident nucleons, namely with the increasing capture γ-ray energy. This is because of the momentum mismatching between the incident nucleons and out-going γ-rays . On the other hand, energetic γ-rays may arise in terms of the momentum matching from a two-body effect following the collision of the incident nucleon with the target nucleon (see Fig. 1.1c). Such nucleon nucleon interaction effect or exchange current effect may be studied by investigating medium energy γ-rays. A recent theoretical work underscores the importance of such reaction mechanism in the medium energy radiative capture reactions (GA78). Photonuclear cross sections in the medium energy region show good agreement with theoretical calculations with the exchange current contribution (HE76).

Another important feature of studies of medium energy capture γ-rays is to investigate γ-radiations to highly excited region. Assuming that the feature of the radiation mechanism may be determined by the γ-ray energy (see Fig. 1.2), the γ radiation with the E_γ to highly-excited states can be

derived from the radiative capture with the similar E_γ into the low-lying states, which is well investigated by using low energy protons. Therefore, measurements of the radiative capture to the highly-excited states can give the particle configurations with less ambiguity of the reaction mechanism for the $E_\gamma > 30$ MeV region.

The medium energy radiative capture reaction feeds predominantly high spin (stretched configurations) final states. Since the target nucleus is treated as a spectator, the transition matrix element does not depend on the target spin direction in the direct capture process. Therefore, the single particle transition probability for the same single particle orbit of the final state is simply distributed to the final states according to statistical weight of their total spin.

Pioneer works of the medium energy radiative capture reaction have been carried out by Kovash et al.(K079). They demonstrated discrete γ-rays in (p,γ) reactions at Ep = 40-80 MeV. The γ-ray spectrum for the $^{11}B(p,\gamma)$ reaction showed a distinct peak at an excitation energy of 19.2± 0.6 MeV in ^{12}C. $d_{5/2}(p_{3/2})^{-1}$.

1.2 Medium energy gamma ray detector system

In nuclear reactions induced by energetic protons with Ep = 40-65 MeV, probability of emitting energetic γ-rays is several order of magnitude smaller than that of nucleon emission. Followings are necessary for a detector for measuring such medium energy γ-rays. i) Good energy resolution: In order to separate individual γ-rays feeding low-lying levels, a good energy resolution is required. ii) Neutron rejection: The γ-rays have to be picked up among huge flux of neutrons. Neutrons can be eliminated by a time of flight (TOF) measurement. Good timing signal is essential for the neutron rejection. iii) Cosmic ray rejection: The energy deposit of cosmic ray muons is as large as that of the medium energy γ-rays. The counting rate of cosmic ray muons is also same order of that of energetic capture γ-rays. Therefore, they must be rejected. iv) Good stability: Since the medium energy radiative capture reaction is rare event, a long data-taking term is needed to get an energy spectrum with good statistics. Therefore, the gain stability has to be good to get good energy resolution.

Single NaI crystals with large volume have been used for detecting energetic γ-rays in several laboratories (SU68, DI70, KE70, DA71, HA74). They are typically a 25 cm $\phi \times 25$ cm, which are surrounded by plastic scintillators as a Compton suppressor. The plastic scintillator can also reject cosmic ray muons.

Recently we have succeeded in developing a special NaI crystal ensemble called HERMES (high energy gamma radiation measuring system). It has been shown to give fairly clean spectra for medium energy γ-rays with E_γ = 20-35 MeV in our previous works of the radiative ^{3}He capture reactions (KI80). The spectrum has been much improved in both the energy resolution and the S/N

ratio. The HERMES consists basically of the 27.9 cm $\phi\times$ 27.9 cm (11"$\phi\times$11") NaI ensemble surrounded by the plastic scintillators as a Compton suppressor. The NaI ensemble is composed of the 15.2 cm $\phi\times$ 27.9 cm (6"$\phi\times$11") central NaI crystal and the 27.9 cm $\phi\times$ 27.9 cm (11"$\phi\times$11") annular NaI crystal. The annular one is divided into four segments. These segments and the central crystal are divided optically from each other. The division of the NaI ensemble improves the energy resolution and the S/N ratio because of following reasons.

i) Improvement of the energy resolution: Energetic γ-rays entering the central NaI are mainly converted to e^+-e^- pairs. Many bremsstrahlung photons, Compton γ-rays and e^+e^- annihilation γ-rays may follow the e^+-e^- pairs. Most of the incident γ energy is deposited on the central NaI and a small fraction of it leaks out the central NaI. Most of escaped photons are captured by the annular NaI crystal. Therefore, the energy resolution of the total system is determined by the energy resolution of the central NaI without losing the peak efficiency (see Fig. 3.4). The 6"$\phi\times$11" size is practically just adequate to get a good resolution crystal.

ii) Improvement of the S/N ratio: Smaller detectors are better than the larger detectors with respect to the S/N ratio. This is because many types of noise signals are roughly proportional to the volume of the detector. In the present case only the small 6"$\phi\times$11" NaI detector is sensitive to the noise signals, because we record events with large energy (> 14.5 MeV) deposit on the central crystal.

Consequently, we succeeded in getting low background γ-ray spectra with a fairly good energy resolution of 2.8 % for 22.5 MeV γ rays.

1.3 Purpose of the present work

For better measurement of the medium energy γ-rays (E_γ > 30 MeV), several improvements are inevitable. One of important points is to improve electronics and the data acquisition system so as to fit to the HERMES. At the higher γ-ray energy region, the event rate of the true high energy γ-ray detection rate becomes smaller in comparison to the noise event rate. Thus the true events must be selected out severely. A multiparameter data acquisition system and an elaborate data reduction algorithm are indispensable to select the true γ-ray events and to derive the γ-ray energy.

In the present thesis, the generalized multiparameter data acquisition system is described in chapter II. The results of the improvement of the electronics and the data reduction (on-line and off-line) algorithm are described in chapter III.

The medium energy (30 - 70 MeV) γ-rays following radiative capture reactions were studied by means of the improved γ-detection system. Analysing power of energetic γ-rays following radiative polarized proton capture reaction is crucial for investigating the spin direction of the nucleon associated with the transition. However, no measurement with a medium energy polarized proton beam has so far been reported. We report in chapter IV the first precise study of medium energy (30-75 MeV) γ-rays following radiative captures of polarized protons on ^{11}B and ^{12}C. The angular dependences of the differential cross sections and those of the analyzing powers for low-lying final states are related to their microscopic configurations. This relation is discussed in terms of the direct capture model. The observed angular dependences for the high-lying final states are discussed in view of their microscopic configurations, of which configurations are known from studies of

other reactions and RPA calculations. The energy dependences of the differential cross sections and the angular dependences of those are compared with the calculations (GA78, TS79) including the effect of the exchange current which may be important in medium high energy γ-rays.

2.1 Introduction

Recently, demands for a fast and multi-parameter data acquisition system have been increasing in view of two types of multi-parameter measurements.

i) **Correlation measurements**: Particle (nucleon, electron, photon, etc.) correlation measurements are useful for investigating nuclear properties as well as nuclear reaction mechanisms. These measurements need plural detectors. In some of recent experiments, the number of detectors required is quite large, and will increase rapidly in near future. Combination of the coincidence signals from these detectors becomes very complex. Thus handling of the multi-combination of signals from these detectors, which deal with multi-kinds of events, is a key point for efficient correlation measurements.

ii) **Measurements with a multi-parameter detector-ensemble**: A multi-wire proportional chamber (MWPC) ensemble used for high energy experiments is one of the examples. The ensemble consists of some sets of the MWPC's and other elements. Each element used for the detector-ensemble is a single parameter detector. Combination of these elements (detectors) is necessary to deduce, for example, energies of detected particles. A multi-parameter detector-ensemble has usually some redundancy for identifying the particles (the events). This redundancy helps one to improve the S/N ratio. Thus the multi-parameter detector-ensemble is very powerful to pick up true events among huge background events. It must be mentioned here that the HERMES used for the present work is a kind of multi-parameter detector-ensembles. Therefore the HERMES is a powerful detector to investigate energies of medium energy γ-rays, which are rather rare events and have to be selected out from huge backgrounds (neutrons etc.).

The CAMAC system is a digital data handling system. It is widely used

with a computer. At the beginning the CAMAC was developed for a multi-parameter detector-ensemble for high energy experiments. Since it can treat NIM fast signals directly, it is useful for fast data acquisition. A typical CAMAC module such as ADC, TDC etc. has several channels and a single input for trigger or gate signals. This makes it easy to handle the multi-parameter detector-ensemble. The CAMAC system, however, is not always adequate for the correlation measurements because a single trigger is not suitable for.

Many types of multi-parameter data acquisition systems have recently been developed. In the low energy nuclear physics experiments, many types of ADC interfaces, some using the CAMAC system as an interface to a computer, have been developed for correlation measurements. However the number of parameters handled by them is limited typically up to 8-16. Furthermore they can hardly treat more than one hundred types of events.

On the other hand, many types of data acquisition systems using the CAMAC system have been developed for the high energy experiments. They can treat up to several thousand words (parameters) for every events.

Our current demands for a data acquisition system arise from the HERMES, which is a multi-parameter detector-ensemble, and the correlation measurement. The correlation measurement for the GQR correlation study (OH82) used two sets of a position sensitive counter telescope for a detection of α particles, four neutron counters and two Ge(Li) γ detectors. Therefore we needed a data acquisition system so as to meet following requirements. i) The CAMAC system is used, since it can deal with NIM fast signals and it is adequate for the multi-parameter detector-ensemble. ii) The HERMES needs a system which can handle at least 14 parameters. The correlation measurement demands handling of at least 24 parameters. iii) The multi-detector

measurement needs a system which can control at least 2^7 types of events.

There is no data acquisition system which meets these demands for low energy nuclear physics experiments. System developed for high energy experiments using a synchrotron can not be used because of following reasons. Since the synchrotron is a pulsed accelerator with a beam pulse interval of about 1-2 sec, data is transferred rapidly to a computer memory within the flat top of the beam pulse and they are analyzed between the beam interval. It is not adequate for the nuclear physics experiments by using accelerators without any macroscopic time structure. Consequently we had to developed a new general data acquisition system so as to meet our demands in the nuclear physics experiments.

2.2 New data acquisition system

Experimental demands for the new data acquisition system are described in the last section. In this section, we discuss practical aspects of the new system.

Raw data processing and reduction of data are important functions of the data acquisition system. On-line data reduction, by which histograms are reduced from raw data, is necessary for on-line monitoring. The data acquisition itself may in principle be possible without the on-line monitoring. However, it is not practical because one needs on-line monitoring to find troubles in detectors and electronics during the data taking run. Proper data reduction may yield relevant results as well.

In order to prescribe the on-line data processing, two different methods were considered to design the new system. One is to use a simple computer language such as "C", "FORTH", or other new one. This method is very powerful and flexible. However, users are required to have the knowledge of this language. Since majority of low energy nuclear physicists are not yet familiar with such method, this method was thought to be not adequate for the new system. It is worth mentioning that this type of data processing will be necessary in near future.

Thus we had employed in this work another method with prescription menu. Here users select some in the menu. Data processing is carried out by combination of selections in the prescription menu.

The PDP-11/44 computer and the MBD-11 (Microprogramable Branch Driver) are used for the data acquisition. The MBD-11 is a very fast intelligent CAMAC branch driver. It has a function of the DMA (Direct memory access) transfer to the PDP-11. The intelligence and the DMA transfer are

indispensable for a fast data acquisition. However, the memory size of the MBD-11 is rather small, and its instruction set is very difficult to be understood. Thus it is almost impossible to carry out the flexible and easy prescription of the data processing with the MBD-11 unless the menu selection method. This is another reason of employing the menu selection method. We had to prepare some menu of data processing program for the MBD-11. The multi-task support operating system, RSX-11M, was employed for the new data acquisition system.

Fig. 2.1 shows a block diagram of the software for the new data acquisition system. It consists of three soft-ware processors. i) **Command processor**: This processor interprets the command from the key-board and controls the data processor. The display of a histogram is also processed in this part. ii) **Data processor**: This processor acquires the raw data through the MBD-11. Then it writes the data on a magnetic tape, and reduces them to histograms for monitoring according to the EDT (Event Descriptor Table), in which the selected prescription menu is described. iii) **Event descriptor table handling system (ETHS)**: This utility creates and modifies the EDT.

2.2.1 Command processor

A general purpose data acquisition software, which utilizes the PDP-11 and the Raw Data Processor (YA76,KA80i), had been developed by Ogata (OG80). It has been extensively used for multi-parameter measurements at the Research Center for Nuclear Physics (RCNP). It consists of the command processor ("COMND") and the data processor ("DATTAK"). The command used in this command processor is familiar for us, and its monitoring function satisfies our requirements. Thus this command processor, being modified a little, was used

as the command processor of our new data acquisition system.

2.2.2 Data processor

Based on the previous system of RCNP, the new data processor is developed for the data acquisition with the MBD-11. The EDT (Event descriptor table) has been modified also. Performance of the new data processor is tabulated in Table 2.1.

Since the data reduction for monitoring is processed by the CPU only when it is waiting for the next raw data buffer, the data acquisition speed is just the raw data processing speed. The conversion time (Tc) of the CAMAC ADC and TDC, the data processing time (Tb) at the MBD-11 and the data transfer time (Tm) to the magnetic tape (MT) determine the data acquisition speed. Tc is about 100 μsec, Tb is about 5 μsec for each parameter, and Tm is about 56 μsec for each parameter (45 inches per sec and 800 *bpi* per inch). The data transfer to the MT can be made while the conversion and the data processing are underway. Thus the time subject to the data processing time is Tc+Tb. For example, in case of 800 random events with 14 parameters every second, 80 msec and 56 msec are consumed every second at the CAMAC processing and the MBD-11 data processing, respectively. Thus 136 msec (14 %) dead time arises from the CAMAC + MBD-11 processing in every second. The time 630 msec consumed at the MT does not contribute to the dead time unless it exceeds one second, because the MT recording is made regularly.

2.2.3 Event descriptor table handling system

This part was not contained in the previous system. We employed the menu

selection method because it is easily handled. In order to handle the menu selection two types described below were considered.

i) **Sequential selection system**: In this system contents of the menu appear sequentially. Preparing the default value in case that users do not select particular values, it is easy to make the menu selection table without knowledge of the whole system flow. However modifying the table is not easy, because it is difficult to know the selection restart point. The "HELP" function helps partly this problem.

ii) **Random selection system**: The menu selection table is displayed directly on the CRT screen. It is easy to look out over the system. Thus modification is easy. However, it is necessary to set the whole table. This is quite annoying. Therefore, we have made the system so that the default values resulting necessarily from the change of other values in the table are always set properly. Since the modification function is important, we have employed this system.

The "PAGE" utility is useful for the random selection system. The "PAGE" was developed by Chiba and Hayano in the KEK as a utility of the KEK-X system[HA80,HA82]. The "PAGE" displays the menu table on the PDP-11 memory and modifies it according to the display text file. Since the "PAGE" cannot handle directly the previous EDT (menu table), the new EDT was defined. The new EDT is divided into two parts. i) On-line EDT is optimized for the on-line data processing. ii) Off-line EDT is optimized for the "PAGE". This means optimization for users. Using the task "CON", these two tables are connected. The sequential default is processed by the task "ETS" (Event Descriptor Table Support). Since the ETS and CON are spawned by the PAGE, users are not required to be familiar with these tasks. The off-line table is stored on the magnetic disk by the ETS.

We have successfully developed the new data taking system. With the help of the screen editing, the EDT can be easily modified so that even beginners can use the system with no difficulty. Data taking by means of the CAMAC is very powerful for multi-parameter measurements. The CAMAC can handle fast signals directly. The new data taking system can be used extensively for multi-parameter and correlation measurements.

3.1 Introduction

Lower energy γ-rays (≦ 30 MeV) have been studied mainly to investigate giant multipole resonances. The study of giant resonances demands a good γ detector for γ-rays in a 10-30 Mev region. Several large NaI spectrometers have been developed previously(SU68,DI70,KE70,DA71,HA74). Characteristics for some of them are listed in Ref. HA74. Most of them use a large volume NaI(Tl) crystal of typically 25 cm $\phi \times 25$ cm.

Energetic γ-rays entering the NaI crystal are mainly converted to e^+-e^- pairs. These e^+ and e^- cause a bremsstrahlung photons, and e^+ annihilates finally with e^- by emitting two 511 keV γ-rays. Some γ-rays are those by Compton scattering. The full energy of the γ-ray is deposited in the detector provided that all of these photons and electrons are absorbed in the detector. However, the full energy cannot be deposited if some photons escape from the detector. Those escaping photons are detected by plastic scintillators surrounding the NaI crystal. Thus the full energy loss event can be selected by requiring anti-coincidence with the signal from the plastic scintillators.

In order to get more sharp spectrum, following correction (see Fig. 3.1) had been carried out for the γ-ray detectors, since the efficiency of the plastic scintillator shield is not 100 %.

$$A=F+(1-f)\times E. \tag{3.1a}$$

$$R=f\times E. \tag{3.1b}$$

Here, A is the accepted NaI spectrum, which is taken in anti-coincidence with signals from the plastic scintillators, R is the rejected NaI spectrum, which is taken in the coincidence with signals from the plastic scintillators, F is

the full energy loss NaI spectrum where the γ-ray energy is fully absorbed in the NaI, E is the NaI spectrum for events where some photons escape from NaI, and f is the detection efficiency of the plastic scintillators for escaping photons. Factor f is not a constant value but a function of the energy of the escaping photons. Then we get

$$F=A-\frac{1-f}{f}\times R \tag{3.2}$$

Assuming that f is a constant value which is independent to the γ-ray energies, the factor $(1-f)/f$ for the HERMES was obtained so that the γ-ray peak in the energy spectrum becomes of Gaussian shape. The $(1-f)/f=0.9$ is obtained for the low energy γ-ray measurements.

The present work deals with medium energy γ-rays with extended energy region of 30-70 MeV. Followings are important for measurements of the medium energy γ-rays.

i) **Good energy resolution**: Good energy resolution is necessary to separate individual γ-rays feeding the low-lying levels, since the energy resolution (ΔE) is taken worse with the increasing the γ-ray energy. It is practically given as

$$\Delta E=a\times E^{3/4}, \qquad \Delta E/E=a\times E^{-1/4}, \tag{3.3}$$

where "a" is a energy resolution for an 1 MeV γ-ray. A ΔE of a detector with a = 0.1 is 2.4 MeV for a 70 MeV γ-ray. Thus detectors with small "a" are required for the medium energy γ-ray detection. Good energy resolution also improves S/N ratio.

ii) **Neutron rejection**: In nuclear reactions induced by energetic protons, the probability of emitting medium energy γ-rays is several order of magnitude smaller than the nucleon emission probability. Radiative capture

total cross sections in the medium energy region (Ep = 40-65 MeV) are as small as ~500 nb. On the other hand, the cross sections of neutron emission are an order of a couple of hundreds mb. Furthermore, medium energy γ-rays have to be picked up among huge flux of neutrons.

iii) **Cosmic ray rejection**: Medium energy γ emission following radiative capture is indeed rare event. In case of a typical radiative capture process with say 100 nb/sr, 30 nA proton bombardment of a 3 milli-mol/cm^2 target yields 40 γ-ray events per second per steradian. A typical γ-ray detector efficiency with 10 msr get only 0.4 counts per second. On the other hand, cosmic ray flux is about $2.4\times10^{-2}cm^{-2}sec^{-1}$ on the horizontal plane. For the large volume NaI detector, typically 25 cm $\phi\times25$ cm, the counting rate of cosmic ray events amounts to 15 counts per sec. A minimum ionization in NaI is 4.84 MeV/cm, namely 60.5 MeV for a NaI crystal with typical thickness of 12.5 cm. It is just in an energy region of the medium energy γ-rays. Thus it is necessary to reject cosmic rays.

iv) **Good stability**: It takes a long term to get good data for rare events with adequate statistics. Thus stability of the detector gain for a long term is indispensable in order to get data with good resolution.

The energy resolution and S/N ratio of previous large single crystal NaI detectors, are not sufficient for medium energy γ-rays. We designed a new detector system HERMES for the detection of energetic γ-rays by taking into account the points mentioned above.

3.2 HERMES

HERMES (high energy gamma radiation measuring system) gave fairly clean spectra for the 20-35 MeV γ-rays. A sectional layout of the HERMES is shown in Fig. 3.2. The major part of the HERMES is an 27.9 cm φ×27.9 cm (11"φ×11") cylindrical NaI detector. This large NaI detector is composed of two parts. One is a central 15.2 cm φ×27.9 cm (6"φ×11") cylindrical crystal, the other is 27.9 cm φ×27.9 cm (11"φ×11") annular crystal surrounding the central one. The annular one is divided into four segments, each being a quarter cylinder. Each NaI crystal is optically isolated by magnesium oxide (MgO) powder. The whole NaI detector is packed in a 3 mm thick aluminum can. The NaI detector is surrounded by 10 cm thick annular plastic scintillators and a 7 cm thick front plastic scintillator. The annular plastic scintillator is covered with a 5 cm thick lead shield. A 10 cm thick lead shield is placed in front of the front plastic scintillator. All lead shields are covered by 0.5 mm thick cadmium sheets to absorb thermal neutrons.

3.2.1 Energy distribution in the annular crystals

Energetic γ-rays entering the central NaI deposit most of their energies on the central NaI. Some low energy photons escape partly from the central NaI and are likely absorbed by the annular NaI. Therefore, the energy deposited on the annular NaI is much smaller than that deposited on the central crystal. Fig. 3.3 shows a pulse height distribution of one of the annular crystal segments obtained for the $^{12}C(p,\gamma)^{13}N$ reaction at Ep=50 MeV. Here the spectrum has been gated by the large energy deposit ($\geqq$ 14.5 MeV)

on the central NaI crystal. A distinct peak coresponds to 511 keV e^+e^- annihilation γ-rays. The continuum spectrum is due to the Compton γ-rays and the bremsstrahlung photons. It decreases exponentially with the increasing energy deposit "Ea". The spectrum is fitted by the function $a\times e^{-\lambda Ea}$ with a decay constant of λ=0.94±0.12 MeV^{-1}, as shown by a solid line in the figure. Events with the energy deposit of less than 3 MeV on one of the annular NaI segments amounts to almost 98 % of the total events recorded in the spectrum. Since γ-rays escape statistically, the total energy deposit on the whole annular NaI crystal is evaluated as $a\times e^{-\lambda' Ea}$ with a decay constant of λ'=0.7 MeV^{-1}. It is still much smaller than the energy deposit on the central NaI crystal.

The γ-ray energy is deduced from summation of the energy deposit on the central NaI and that on the whole annular NaI. Therefore, the total resolution is described as follow.

$$R_{total}=\sqrt{(Ec/(Ec+Ea))^2Rc^2+(Ea/(Ec+Ea))^2Ra^2}, \qquad (3.4)$$

where Ec and Ea are the energy deposit on the central NaI and the whole annular NaI, respectively, and R_{total}, Rc and Ra are the resolution of the total system, the central NaI and the whole annular NaI, respectively. Since Ea/(Ec+Ea) is very small and Ec/(Ec+Ea) is nearly equal to 1, R_{total} is determined by Rc. The present central NaI has been so made as to give fairly good energy resolution compared to large NaI detectors developed previously in other laboratories. Consequently the energy resolution of the HERMES as a whole is as good as the small central NaI, and its peak efficiency is as large as previous large single crystal NaI detectors (see Fig. 3.4). Thus the improvement of energy resolution is successfully achieved.

3.2.2 Cosmic ray rejection

As mentioned in section 3.1, cosmic ray rejection is crucial for measurements of rare γ-rays. The plastic scintillators surrounding the large NaI crystal can reject almost all cosmic rays with efficiency $f' \sim 100$ %. However, estimation of the full energy loss spectrum from the "accepted" spectrum and the "rejected" spectrum is impossible because the cosmic ray spectrum is included only in the rejected spectrum. The eq. 3.1 is written for such rare γ-rays.

$$A = F + (1-f)\times E + (1-f')\times C \rightarrow F + (1-f)\times E \qquad (3.5a)$$

$$R = f\times E + f'\times C \rightarrow F\times E + C. \qquad (3.5b)$$

Here, C is the cosmic ray spectrum. It is impossible to derive the full energy loss spectra from the measured spectrum A and R without knowing either the spectrum C or the spectrum E. Therefore, we need the cosmic ray rejection without the plastic scintillator.

In order to reject cosmic rays without the plastic scintillator, two methods are possible. One is to use the TOF data. Since cosmic rays do not correlate in time with the naturally bunched beam pulse of the cyclotron, one can obtain the cosmic ray spectrum "C" using the TOF data. We employed another way. It is more simple and is possible only by the HERMES. Note that the cosmic rays cross not only the plastic scintillator but also the annular NaI crystals, and deposit the energy of about 30 MeV. On the other hand, medium energy γ-rays entering the central crystal deposit only small fraction of its energy on the annular NaI crystal. The energy deposit on one of the annular NaI segments do not exceed 8 MeV. Thus the cosmic rays with large energy deposit can be distinguished from the photons sneaking from the

central NaI.

3.2.3 Response and efficiency

Pair production cross section for medium energy γ-rays is very large. For example, the absorption length of 60 MeV photons in NaI is about 5 cm. Thus the probability that the γ-rays pass through the 28 cm long HERMES without any interaction is only 0.4 %. It means that the efficiency of the HERMES is almost equal to the geometrical solid angle. In order to know the peak efficiency, the response function of the HERMES for the mono energy γ-rays is necessary. The response function is not a Gaussian shape because some fraction of the γ-ray energy is carried away by low energy photons escaping from the NaI detector. Thus the response function of the NaI can be derived from the energy spectrum of this escaping photons. In fact, the escaping photons are considered to be mostly go away at the back-end of the NaI crystal, where neither annular NaI nor the plastic scintillators cover the central crystal. The spectrum may be simulated to one of the annular NaI. As mentioned above, this energy spectrum can be fitted with the $exp(-(0.94\pm0.12\ MeV^{-1})\times Ea)$. Thus a gaussian plus exponential tail is employed as a fitting function to derive the peak counts for low-lying levels. Details of the peak fitting program is given in section 3.5.

3.3 Electronics and on-line processing

In order to measure good γ-ray spectra in the medium energy region, the signal arising from the γ-rays must be selected from the high counting rate background signals. The followings are the present procedure of the electronics and the on-line data processing of the HERMES for the medium energy γ-ray measurements.

i) Counting rate for each crystal is high because of neutrons and low energy γ-rays. In order to prevent signals from piling up, a fast signal processing is necessary. The NIM fast signal is better than the slow signal in order to reduce the pile-up. The pulse width of the NIM slow signal is about 1∼3 μsec . On the other hand that of the NIM fast signal is about 1∼100 nsec. Therefore, the NIM fast signal endures high counting rate up to the limit of what the detector can accept.

ii) In order to get good energy resolution, the analog signal is obtained through the pulse shaping electronics (TFA : Timing filter amplifier) so that the pulse-height of the analog signal is proportional to the total charge output from the PMT (Photo multiplier tube) of the central NaI. The pulse width is about 500 nsec. Therefore, the pile-up rejection using the fast signal is required.

iii) Since the medium energy γ-rays have to be selected out from huge flux of neutrons, neutrons were eliminated by measuring the time of flight (TOF). The TOF data are recorded event by event using the data acquisition system, which are described in chapter II. The neutrons, taking longer flight time, may in principle be eliminated at off-line sorting of this TOF data. However, in case of our experiment (Ep=50MeV θ_{lab}=60°) γ-ray events were only about 5 % of total events which deposit more than 15 MeV on the central

NaI. Thus on-line neutron rejection is necessary in order to reduce the number of magnetic tapes.

3.3.1 Outline of the electronics

The NIM fast modules and the CAMAC system were used. Fig. 3.5 shows basic electronics for the HERMES. Event trigger signal is obtained from the central NaI. The discriminator level was set just below the 15.11 MeV $1^+, T=1 \rightarrow 0^+, T=0$ ^{12}C γ-ray peak. This peak was used as an energy reference. The medium energy γ-rays entering the central NaI deposits most of its energy on the central NaI. Thus setting the high discriminator level on the central NaI signals reduces much the event rate because the background signals are mostly below the discriminator level, but it reduces little the efficiency for the medium energy γ-rays far beyond 15 MeV. Since Q-value of the neutron capture reaction in NaI(Tl) is about 8 MeV, γ-rays following the slow neutron capture in the NaI crystal appear only below the discriminator level. Gamma rays following particle emission and γ-rays from radio-active isotopes produced in nuclear reactions have energies below the discriminator level. Consequently all these γ-rays can not produce event trigger signals.

The trigger signal opens the ADC gate and starts the TDC. Output signals from the fast amplifiers (TFA : Timing filter amplifier ORTEC 474) are directly used for input signals to the ADC. Their timing was shifted by a proper delay line so as to match with the timing of the gate signal. The ADC used is a peak sensitive type, where the peak voltage during the gate period of 500 nsec is converted to the digital data. Since the gate used in the ADC is the fast gate, it can stand well high counting rate. On the other hand the data processing following the event trigger takes a long time of about

100~200 μsec. Thus the event trigger for the data process must be selected so as to reduce the number of events as much as possible. The neutron events and the pile-up events are rejected by using a fast logic as follows.

3.3.2 Fast clear

The CAMAC ADC yields the LAM (Look at me) signal on the CAMAC Data way when conversion is completed. The LAM signal starts the data processing of the MBD-11. A fast clear signal cancels the conversion for both the ADC and the TDC, and prevents the LAM signal from arising. Using the fast clear, event selection after the event trigger becomes possible. Events were triggered firstly by rough selection and were cancelled by the fast clear signal after severe selection.

3.3.3 Pile-up rejection

The two successive events within 1 μsec were rejected. In order to judge whether the pile-up event or not, following processes must wait for this 1 μsec. The analog signals from the detectors must be stored elsewhere for this 1 μsec. Thus delay lines might be used for the storage. However, use of the 1 μsec delay line for signals from every NaI scintillators would be not practical because the length of delay line amounts to 200 m for each analog signal from the HERMES and the attenuation in the delay line would become appreciable. Therefore, by using the fast clear the analog signals could be stored in the ADC for this 1μsec duration.

The main components of the electronics used are shown in Fig. 3.6. The up-dating discriminator is used as a tag whether the signal comes from the

lower discriminator during the preceding 1 μsec. If there is no signal from the lower discriminator during the preceding 1 μsec, then the signal from the higher discriminator triggers the CAMAC system, so that analog signals are fed into the ADC and the conversion starts. The output of the up-dating discriminator is checked 1 μsec later again. If there are signals from the lower discriminator during the preceding 1 μsec, the fast clear signal is generated to cancel the conversion for the all modules and to prevent the data from processing.

3.3.4 Neutron rejection

Because the neutron event rate is very high in spite of the high discriminator level, one needs to reject most of neutrons by using a electronic circuit in order to save the amounts of magnetic tapes. The TAC (Time to analog converter) was used to derive the TOF data. The single channel output of TAC, which corresponds to the neutron events, gave the fast clear signal, which was used for the on-line neutron rejection.

The electronics actually used in the measurement are shown in Fig. 3.7.

3.4 Data reduction

Since the HERMES is a kind of multi-parameter detector, some data reductions are necessary in order to deduce the γ-ray energy. Some parameters are used for selecting true γ-ray events. Followings are realized by the data reduction program.

i) Derivation of the γ-ray energy: Sum of energy deposits in all the NaI scintillators used for the HERMES gives the γ-ray energy. In practice amplifier gains for these NaI scintillators are not the same. Therefore, the gains were properly adjusted when the pulse heights of these scintillators were summed up.

ii) Neutron rejection: The γ window in the TOF spectrum selects the γ events. After severe event selection, background events were negligibly small. The neutron contamination is less than 7 % in the γ-ray spectrum above 14.5 MeV at θ_{lab}=40° for the 50 Mev proton bombardment, that was negligibly small in the 40-70 MeV region, which is corresponding to the medium energy radiative capture γ-rays.

iii) Cosmic ray rejection: Cosmic ray events were rejected by throwing away events with the large energy deposit beyond 8 MeV on any segment of the annular NaI crystal. The rejection efficiency was almost 100 % and the energy spectrum was free from the cosmic ray background without using the plastic scintillator as a cosmic ray shield. Cosmic rays coming horizontal may enter directly the central NaI without passing through the annular NaI crystal. The event rate of such horizontal cosmic rays is indeed negligibly small, and the energy deposit of such cosmic rays is about 135 MeV. This energy is beyond the medium energy γ-ray region.

iv) Router using signals from the plastic scintillator: In order to

estimate the full energy loss spectrum, two histograms were necessary. One is a raw spectrum independent of signals from the plastic scintillators. The other is a spectrum obtained with the anticoincidence of the signals from the plastic scintillators. Using the notation of eq. 3.1, the former is the A+R (accepted spectrum + rejected spectrum), and the latter is the A (accepted spectrum). About 85 % events for the $^{11}B(p,\gamma)^{12}C$ reaction at Ep = 50 MeV were accepted. The efficiency f of the plastic scintillator for the escaping photons in the medium energy γ-ray measurements had not been investigated yet. Therefore, only the accepted spectra "A" were used in the following analysis.

The FORTRAN program used for the data reduction is shown in Fig. 3.8. It took 25 minutes to perform some reduction procedure of a magnetic tape by means of PDP-11/44 and the TU-10 magnetic tape handler. Since the RSX-11M is multi task operating system, same two tasks can perform the reduction of two magnetic tapes at the same time. The speed was limited by the magnetic tape handler (45 inches/sec 800 bpi).

The γ-ray window in the TOF spectrum and the gain factors were read in from the parameter file, which was used later as documents of the data reduction parameters.

Histograms were generated for every data taking run, one run data corresponding to about one magnetic tape. In order to get the γ-ray spectrum at each detection angle, the histograms were summed up with proper gain adjustment for relevant data taking run. The gain adjustment was within about 1 %. Therefore, the spectrum was subject to almost 1 % gain shift. This is appreciable in the present measurement, since the total energy resolution was about 3.5 %. Some improvements of the gain stabilizer are necessary for practical use in the 50-100 MeV γ-ray energy region.

3.5 Peak fitting

A proper response function for medium energy γ-rays is necessary to derive the differential cross section from the spectrum. As mentioned in section 3.2, a Gaussian plus exponential tail is employed as a fitting function. The fitting function itself is same as that used at BNL(C082), but the definition of the parameters used are different from those of the BNL one. As a function of channel number x, the fitting function of a γ-ray peak with energy E is parameterized as the sum of two components, the Gaussian $P(x)$ and the Tail $T(x)$. They are defined as

$$P(x) = I \times exp(-(Y(x)-E_\gamma/2\sigma)^2)$$

$$T(x) = \begin{cases} I \times P_3 \times (P_5 \times (Y(x)-E)) \times (1-\exp(-((Y(x)-E_\gamma)/2P_4P_6)^2) & Y(x)<E \\ 0 & Y(x)\geqq E \end{cases} \quad (3.6)$$

The parameters and variables used in eq. 3.6 are defined as follows.

E_γ	the γ-ray energy.
$Y(x)$	the energy corresponding to the channel number x.
I	peak intensity parameter.
σ	the peak width (MeV) of the Gaussian.

These are rewritten in terms of the free parameters P_i used for actual peak fitting program.

$$Y(x)=E_{\gamma_0}+\frac{x-P_1}{P_2},$$

$$\sigma=P_4 \times (E_\gamma/E_{\gamma_0})^{3/4}. \quad (3.7)$$

Here σ/E has the energy dependence of $E_\gamma^{-1/4}$. The fitting parameters are described as follows.

P_1 the channel number of the γ_0 peak.

P_2 the gain factor (channel / MeV).

P_3 the tail / peak ratio parameter (arbitrary unit).

P_4 the peak width of the Gaussian for γ_0 (MeV).

P_5 the exponential decay parameter of the tail (MeV^{-1}).

P_6 This defines how the tail smoothly merges with the Gaussian.

The parameter P_1 to P_4 and "I" were treated as free parameters in the peak fitting program. It was difficult to derive the parameters P_5 and P_6 from the χ^2 of the fitting. So the parameters P_5 and P_6 were treated as fixed parameters in the fitting program. However, the estimation of the parameter P_5 is possible by using the energy spectrum of the annular NaI. The energy spectrum of the whole annular NaI is evaluated as the function of the $a \times \exp(-\lambda' E_a)$, where λ' is the decay constant of 0.7 MeV^{-1}. Thus the P_5 must be close to the decay constant $\lambda' \sim 0.7$ MeV^{-1}. The values for the parameter P_5 are in a range of $0.5 \sim 1.0 MeV^{-1}$. The parameter P_6 is defined so that the fitting function becomes finally a smooth function. The peak area was obtained for several sets of the P_5 and P_6. The ambiguity of the peak area due to the choice of the parameter set are included in the error. The peak fit results and parameters used are shown in Fig. 3.9.

4.1 Introduction

Recently radiative capture reactions of medium energy protons have been studied on light nuclei by Kovash et al.(KO79). They demonstrated isolated γ-rays following radiative capture reactions at Ep=40-80 MeV. In the $^{11}B(p,\gamma)^{12}C$ reaction they found a strong γ transition to the 19.2±0.6 MeV state. Arnold(AR79) discussed the microscopic structure of the initial and final states of this reaction.

A direct capture reaction simply populates final states with configurations of 1-particle plus the target nucleus. In this process the incoming proton radiates directly γ-rays and drops into the appropriate particle orbit of the residual nucleus. The high-lying states with the $\{d_{5/2}(p_{3/2})^{-1}\}_{4^-}$ configuration in ^{12}C (AR79) are good candidates of the final states populated directly by the proton radiative capture on the ^{11}B with the $(p_{3/2})^{-1}$ configuration. These are known from other reaction studies (see Table 4.10). Since the radiative capture reaction populates a state of spin J in proportional to the statistical weight of 2J+1, the high-spin final state with the spin-stretched configuration of $J\sim j_p+j_h$ is strongly populated. Tsai and Londergan(TS79) calculated the $^{11}B(p,\gamma)^{12}C$ reaction leading to the spin-stretched high-lying states and the low-lying states in term of the direct capture model. They included in the calculation the contribution from the exchange current. The effect of the exchange current becomes important at the medium energy radiations as discussed in Refs. GA74, HE76 and GA78. Tsai and Londergan showed that the direct capture model calculation reproduces well the observed γ-ray spectra. The 19 MeV excited region in ^{12}C is far beyond the threshold energy of particle emission. Therefore, continuum wave functions have to be used for the final states in this excitation region.

Halderson and Philipott(HA81) studied the bremsstrahlung strength emitted by incident protons interacting with the target nucleus. Calculated there were γ radiations from the initial continuum state to the final continuum state. They also reproduced the observed spectra of γ-rays feeding continuum states above the proton threshold in term of the simple direct process without contributions of the exchange current and the semidirect process. Blatt et al.(BL79) measured the excitation function of the radiative capture on ^{11}B into the high-lying states in ^{12}C. Londergan and Ludeking(LO82) calculated the $^{11}B(p,\gamma)^{12}C$ reaction feeding high-lying states by using unbound final state wave functions. They showed the semidirect contribution is appreciable at $E\gamma \sim E_{GDR}$. Weller et al.(WE82) also calculated the $^{11}B(p,\gamma)^{12}C$ reaction to high-lying states by using both bound and unbound wave functions. The simple direct capture model, without the contribution of the exchange current and the semidirect mechanism, was used in their calculation. The calculated excitation functions agree with the observed ones.

It seems as mentioned above that there are several ways of theoretical calculations. Further experimental studies are important to check these.

Angular dependences of differential cross sections and those of analyzing powers have not been measured so far in these medium energy (Ep=40~80 MeV) radiative capture reactions. High resolution precise studies of medium energy γ-rays are indispensable to derive the information about the microscopic configuration of the nucleus.

The purpose of the present experiment is to investigate microscopic features of the medium energy radiative capture reaction. The HERMES, as described in section 3.2, gave fairly clean spectra for medium energy γ-rays following 40-65 MeV proton radiative capture on ^{11}B and ^{12}C. The spectra were much improved in both the energy resolution and the separation from

background. Several γ-rays were well observed. The angular dependences of the differential cross sections and those of the analyzing powers were measured for the first time. The analyzing powers of radiative capture γ-rays to low-lying states are found to relate to the microscopic configurations of the final states. The analyzing powers of the γ-rays to highly excited regions are compared with those of the low-lying states, and the same relation is found in the microscopic configurations of the highly excited regions, which have been obtained from other reactions and RPA calculations.

4.2 Experimental procedures

The medium energy γ-rays from the $(\vec{p},\gamma)$ reactions on ^{11}B and ^{12}C were measured by using 40-65 MeV polarized protons provided from the Osaka Univ. RCNP cyclotron. The beam intensity was around 5~30 nA. Table 4.1 lists targets, beam energies and beam intensities used for the experiment. The targets used were ^{11}B and ^{12}C. The ^{11}B target was a self-supporting ^{11}B sheet with 31 mg/cm^2 and 98.6 % isotopic enrichment. This target was prepared by Sugai at INS using a hot-press method. The ^{12}C target was a 29.3 mg/cm^2 self-supporting foil. This target was prepared by a commercial natural carbon foil. Natural abundance of ^{12}C is 98.9 %. The energy loss of the incident proton in the target was about 400~450 keV as tabulated in Table 4.2. The γ-rays were observed at θ_{lab}=40° ,60° ,80° ,110° and 135° by the HERMES.

The beam polarization was monitored downstream the target. The asymmetry of the elastic scattering from the carbon target made of a polyethylen film was measured by using two NaI scintillator detectors. Table 4.3 shows the ^{12}C analyzing powers as a function of the proton energy and the proton detection angles(KA80s). The beam polarization was around 80~83 % for 40 and 65 MeV protons and 70~75 % for 50 MeV protons.

The electronics circuits used were as described in section 3.3. The trigger signals were generated for the event signal with large energy deposit (≧14.5 MeV) on the central NaI. The lower discrimination level for the central NaI, output of which was used for the pile-up rejection as described in section 3.3, was set at about 800 keV for the 50 (40° ,60° ,80° ,110°) and 65 MeV proton bombardments and at about 2 MeV for the 40 and 50 (60° ,135°) MeV proton bombardments. The threshold level of the annular NaI was set at about 300 keV. The counting rate of signals beyond the lower discriminator

for the central NaI was around 30-60 kc/sec. That of one segment of the annular NaI was about the same as that of the central NaI. Dead time was corrected for by counting the number of the output signals from the central NaI and the number of events rejected. The dead time is mainly due to the event rate of high discriminator. It was typically 5 % at Ep = 40 MeV and about 25 % at Ep = 50 and 65 MeV.

Background neutrons were rejected by a time of flight technique. The flight path L_{TOF} from the target to the detector face was 75 cm at Ep = 40 MeV and 90 cm at Ep = 50 and 65 MeV as tabulated in Table 4.1. The time of flight (TOF) spectra for L_{TOF} = 75 cm at Ep = 40 MeV are shown in Fig. 4.1. They were measured at 60° to the beam axis. The time resolution for the γ-ray peak is 3.0 - 3.5 nsec including about 2.6 - 3.0 nsec beam width. The spectrum after the on-line neutron rejection by using the fast clear as described in section 3.3 is shown in the figure. The neutron events rejected by the on-line TOF measurement were about 90-95 % of the total triggered events.

Cosmic ray backgrounds were rejected with almost 100 % efficiency by using the annular NaI signals as described in section 3.2.2.

The over-all resolution for the 60 MeV γ-rays was about $\Delta E/E \sim$ 3.8 % including 0.9 % due to the target thickness and about 1 % due to the gain shift.

The solid angle of the HERMES set at 90 cm from the target is 10.4 msr and it is 15.7 msr at 75 cm from the target. Absorption rate of 29 % for the γ-ray in the 40-60 MeV region by the material between the target and the central NaI crystal was corrected for. About 18 % beam loss between the target and the Faraday cup was also corrected for. The ambiguity in evaluating the γ peak area by using various peak fitting functions was

included in the error of the data. The systematic error for the absolute cross section due to the error of the target thickness and that of the various corrections amounts to about 20~30 %. The data for the 40 MeV proton bombardment at all detection angles and those for the 50 MeV proton bombardment at θ_{lab}=135° were taken separately from other data at Ep = 50 MeV and 65 MeV. Thus the absolute cross sections for the 40 MeV proton bombardments and for the 50 MeV proton bombardments at θ_{lab}=135° were normalized to the that for the 50 MeV proton bombardments at θ_{lab}=60° . The normalization factor was the 0.706.

4.3 Results and discussion

An observed spectrum of the $^{11}B(p,\gamma)$ reaction at Ep = 50 MeV and θ_{lab}=40° to the beam is shown in Fig. 4.2. Several discrete γ-ray peaks from the $^{11}B(\vec{p},\gamma)$ reaction are evidently seen in the 40-65 MeV γ-ray energy region. They correspond to γ transitions to the ground 0^+, 4.44 MeV 2^+, and 9.64 MeV 3^- states, and those to the 18.8 MeV and 22.3 MeV excitation regions in ^{12}C. The angular dependences of the cross sections and the analyzing powers for these γ-rays are shown in Figs. 4.3-4.8 and Tables 4.4-4.9. Here, the γ-ray yields for the low-lying levels have been obtained by using the peak-fitting program. For the high-lying levels beyond the 10 MeV excitation energy, the peak-fitting is difficult, because the level density is too high to distinguish each levels. Therefore, the differential cross section per 1 MeV excitation energy window has been obtained by integrating the spectrum over the specified energy window. The γ-ray yields for two regions of the distinct peaks (18.8 MeV and 22.3 MeV) and for the neighboring excitation energy regions have been obtained.

An observed spectrum of the $^{12}C(p,\gamma)$ reaction at Ep = 40 MeV and θ_{lab}=60° to the beam is shown in Fig. 4.9. Two discrete γ-ray peaks from the $^{12}C(\vec{p},\gamma)$ reaction are evidently seen in the 30-40 MeV γ-ray energy region. They correspond to γ transitions to the ground $1/2^-$ and the unresolved second excited 3.51 MeV $3/2^-$ and third excited 3.55 MeV $5/2^+$ states in ^{12}C. The angular dependences of the cross sections and the analyzing powers for these γ-rays are shown in Figs. 4.6 and 4.7 and Tables 4.4 and 4.7.

General trends of the angular dependences of the differential cross sections and those of the analyzing powers are discussed in the following subsections in terms of a simple direct capture model. We give a brief

description of the formalism in Appendix 1. In this model, the incoming proton interacting with the target nucleus is considered to simply radiate the γ-ray and to drop into the appropriate particle orbit. Essentially this is a single particle transition. The target nucleus is treated as a spectator and this process does not depend on the direction of the target spin.

4.3.1 Differential cross section

The γ-ray angular distributions can be expanded in terms of the Legendre polynomials as

$$\frac{d\sigma}{d\Omega}(\theta)=\frac{\sigma_{total}}{4\pi}\{1+\sum_{k=1}a_kP_k(\cos\theta)\}\ . \qquad (4.1)$$

The coefficients a_k in the expansion depend on the γ-ray multipolarities as well as the spins of the initial and final states. The odd terms $a_kP_k(\cos\theta)$ with k = odd arise from the interference of the even parity γ radiation with the odd parity one.

The coefficients a_k obtained by fitting the angular distributions of the medium energy γ-rays following radiative capture reactions are tabulated in Table 4.11. The angular distributions show uniformly a similar pattern. There is a bump at the forward detection angle of around 40° ~60° . This forward peaking pattern is due to a positive a_1 coefficient and a small a_2 coefficient. A single particle transition at the present energy region is mainly of an E1 transition, and the main term of which has no spin component (σ). Therefore stretched E1 transitions with $j_i \rightarrow j_f \pm 1$ are dominant. The pure stretched E1 transitions give a negative a_2 coefficient. The stretched E2 transitions with $j_i \rightarrow j_f \pm 2$ give a positive a_2 coefficient. A finite value of the coefficient a_1 is considered to be due to an appreciable E2 admixture

into the E1 radiation. The interference of the stretched E2 with the stretched E1 gives a positive a_1 coefficient. We compute the a_1 and a_2 coefficients for the $p_{1/2}$ single particle final state. The harmonic oscillator wave functions are used as initial and final states for simplicity. The initial state wave functions are multiplied by a factor $\sqrt{2l+1}$ corresponding to the l-wave amplitude of the projectile. The ratio of the reduced matrix elements is $<1d_{3/2}\|E1\|1p_{1/2}> / <2s_{1/2}\|E1\|1p_{1/2}>=-5$. Using the tables in Ref. CA71, a_2 = -0.294 is obtained. The interference of the stretched E2 with these E1 transitions gives $a_1 \sim 2.7\times\sqrt{E2/E1}$. Ten percent admixture of the stretched E2 transition strength gives a_1=0.85 and a_2

The coefficients for the $p_{3/2}$ single particle final state are also calculated. E1 transitions give a_2 = -0.327. The interference of the stretched E2 with the E1 transitions gives $a_1 \sim 2.5\times\sqrt{E2/E1}$. Ten percent admixture of the stretched E2 transition strength gives a_1=0.79 and a_2

This rough calculation gives similar a_1, a_2 coefficients for the $p_{3/2}$ and $p_{1/2}$. Thus the similar pattern of the angular distribution is obtained (see Fig. 4.10). The observed angular distributions are rather close to the calculated one with the 10 % admixture than those of the pure E1 radiation. This fact may indicate admixture of an order of the 10 % E2 component into the E1 ones.

4.3.2 Analyzing power

The angular dependence of the γ-rays following radiative capture of polarized protons can be expressed in terms of the Legendre polynomials as follows:

$$\frac{d\sigma}{d\Omega}(0)=\frac{\sigma_{total}}{4\pi}\{1+\sum_{k=1}a_kP_k(\cos\theta)+\vec{p}\cdot\vec{n}\sum_{k=1}b_kP_k^1(\cos\theta)\}\quad , \tag{4.2}$$

where $\vec{n}$ is the unit vector $(\vec{k}_p\times\vec{k}_\gamma)/\mid\vec{k}_p\times\vec{k}_\gamma\mid$ normal to the reaction plane, and $\vec{p}$ is the polarization of the incident proton. The coefficients b_k are related to the interferences between different quantum amplitudes in the radiative process. The interference between radiations with the same parity leads to the even terms $b_kP_k^1(\cos\theta)$ with k = even, while that of opposite parity radiations to the odd terms with k = odd.

The measured angular dependences of the analyzing powers show two different patterns. One increases with the increasing detection angle θ_γ, and the other decreases with the increasing θ_γ. The difference of the angular dependences reflects the difference of the b_2 coefficients. The b_2 coefficient arises from the interferences between different kinds of E1 radiation amplitudes. For the present radiative capture process, an important process is the interference between two stretched E1 transitions of $j+1\rightarrow j$ and $j-1\rightarrow j$ types. This interference gives finite b_2 coefficients

$$b_2(lj)=c(lj)Im(\langle lj\|M_1^{(E)}\|l+1,j+1\rangle^*\langle lj\|M_1^{(E)}\|l-1,j-1\rangle)$$

$$for\ j>1/2, \tag{4.3a}$$

$$b_2(p_{1/2})=c(p_{1/2})Im(\langle p_{1/2}\|M_1^{(E)}\|d_{3/2}\rangle^*\langle p_{1/2}\|M_1^{(E)}\|s_{1/2}\rangle)$$

$$for\ j=1/2,\ l=1. \tag{4.3b}$$

Here, $c(lj)$ is determined by the 3-j coefficients etc. as shown by eq. A.24 in Appendix 1. Using the tables in Ref. La77 and Mo79, one gets for $j > 1/2$ $c(lj_>) > 0$ and $c(lj_<) < 0$, and for $j = 1/2$, l=1 one gets $c(p_{1/2}) > 0$. The $\langle lj\|M_1^{(E)}\|l'j'\rangle$ is a reduced matrix element for E1 transition from the $\mid l'j'\rangle$ state to the $\mid lj\rangle$ state. It is defined by eq. A.27 in Appendix 1. In

order to estimate the phase of the reduced matrix element, the eq. A.27 is rewritten as

$$<lj \| M^{(E)} \| l'j'>$$

$$= (-)^{j-1/2} i^{l'-l} Z(ljl'j';1/2\ 1) e^{i(\delta_{l'}-\delta_l)} I(ljl'j'). \qquad (4.4)$$

Here, $\delta_{l'}$ is the phase shift of the incoming partial wave with an orbital angular momentum l, and δ_l is the phase of the final state $|l'j'>$. The radial integral $I(ljl'j')$ is positive. The eqs. 4.3a and 4.3b are rewritten as

$$b_2(lj) = -c(lj)Z(l\ j\ l-1\ j-1\ ;\ 1/2\ 1)Z(l\ j\ l+1\ j+1\ ;\ 1/2\ 1)$$

$$\times Im\{e^{i(\delta_{l-1}-\delta_{l+1})}\} I(l\ j\ l-1\ j-1) I(l\ j\ l+1\ j+1)$$

$$for\ j>1/2 \qquad (4.5a)$$

$$b_2(p_{1/2}) = -c(p_{1/2})Z(1\ 1/2\ 0\ 1/2\ ;\ 1/2\ 1)Z(1\ 1/2\ 2\ 3/2\ ;\ 1/2\ 1)$$

$$\times Im\{e^{i(\delta_s-\delta_d)}\} I(1\ 1/2\ 0\ 1/2) I(1\ 1/2\ 2\ 3/2)$$

$$for\ j=1/2,\ l=1. \qquad (4.5b)$$

Let's introduce for simplicity the following quantities,

$$\alpha(lj) \equiv c(lj)Z(l\ j\ l-1\ j-1\ ;\ 1/2\ 1)Z(l\ j\ l+1\ j+1\ ;\ 1/2\ 1)$$

$$for\ j>1/2, \qquad (4.6a)$$

$$\alpha(p_{1/2}) \equiv c(p_{1/2})Z(1\ 1/2\ 0\ 1/2\ ;\ 1/2\ 1)Z(1\ 1/2\ 2\ 3/2\ ;\ 1/2\ 1)$$

$$for\ j=1/2,\ l=1. \qquad (4.6b)$$

Then the eqs. 4.5a and 4.5b are reduced as

$$b_2(lj) = -\alpha(lj) I \cdot I' \sin(\delta_{l-1}-\delta_{l+1}) \qquad for\ l \geqq 1. \qquad (4.7)$$

Here, I and I' are radial integrals, which are positive. The phase shift δ_l

is decomposed into the phase shift due to the central potential and that due to spin-orbit potential.

$$\delta_l=\delta^{V}_{l}+\delta^{s}_{l} \qquad for\ j_> \ (j=l+1/2), \tag{4.8a}$$

$$\delta_l=\delta^{V}_{l}-\delta^{s}_{l} \qquad for\ j_< \ (j=l-1/2). \tag{4.8b}$$

Using eqs. 4.8a and 4.8b, eq. 4.7 is rewritten as

$$b_2(lj_>) = -\alpha(lj_>)I\cdot I'\sin\{(\delta^{V}_{l-1}-\delta^{V}_{l+1})-(\delta^{s}_{+1}-\delta^{s}_{-1})\} \tag{4.9a}$$

$$b_2(lj_<) = -\alpha(lj_<)I\cdot I'\sin\{(\delta^{V}_{l-1}-\delta^{V}_{l+1})+(\delta^{s}_{+1}-\delta^{s}_{-1})\} \tag{4.9b}$$

We note that

$$Z(l\ j\ l-1\ j-1\ ;\ 1/2\ 1)Z(l\ j\ l+1\ j+1\ ;\ 1/2\ 1)I\cdot I' > 0$$
$$for\ j>1/2, \tag{4.10a}$$

$$Z(1\ 1/2\ 0\ 1/2\ ;\ 1/2\ 1)Z(1\ 1/2\ 2\ 3/2\ ;\ 1/2\ 1)I\cdot I' < 0$$
$$for\ j=1/2,\ l=1. \tag{4.10b}$$

Therefore,

$$\alpha(lj_>)>0, \qquad \alpha(lj_<)<0 \tag{4.11}$$

are obtained for $l\geqq 1$. The $\delta^{V}_{l-1}-\delta^{V}_{l+1}$ changes the value of the b_2 coefficient to the opposite direction for the $j_>$ and $j_<$ final states, and the $\delta^{s}_{-1}-\delta^{s}_{+1}$ changes the value of the b_2 coefficient to the same direction. Since the spin-orbit potential is much smaller than the central one, one may get very different values of the b_2 coefficients for the $j_>$ and $j_<$ final states.

Therefore study of the angular dependence of the analyzing power by using polarized protons is crucial for investigating the spin direction of

the nucleon associated with the radiation.

4.3.3 $^{11}B(\vec{p},\gamma)^{12}C$ (γ_a; the ground 0^+ state, and γ_b; the 4.44 MeV 2^+ state)

The observed differential cross sections at θ_{lab}=60° for the γ_a and γ_b are compared with the direct capture model calculation in Fig. 4.11. General trends of the energy dependence are in accord with the calculated values, although the observed value for γ_b at Ep = 65 MeV is somewhat smaller than the calculation. Calculation based on the direct capture model (TS79, GA78) for the γ_a reproduces the observed angular dependence of differential cross section (see Fig.4.4).

Using a pure j-j coupling shell model, the configuration of the ^{12}C ground state (0^+) is the $(p_{3/2})^4$. Actually the wave function contains some of the $(p_{3/2})^2(p_{1/2})^2$ configurations, too, where two particles in the same j orbit are coupled to 0^+. The possible configurations for the ^{11}B ground state with J^π=3/2$^-$ are $\{(p_{3/2})^3\}_{3/2}$ and $\{p_{3/2}(p_{1/2})^2\}_{3/2}$. Therefore, only the $p_{3/2}$ particle (proton) leads to the ^{12}C ground state by coupling with the ^{11}B ground state. According to the pure j-j coupling model, the configuration of the ^{12}C first excited state with J^π=2^+ is mainly the $(p_{3/2})^3p_{1/2}$. Actually the wave function contains some of the component $(p_{3/2})^2(p_{1/2})^2$, where two $p_{3/2}$ particles are coupled to 2^+. Therefore the configuration of the particle (proton), which leads to the ^{12}C first excited state by coupling with the ^{11}B ground state, is mainly $p_{1/2}$ and to some extent $p_{3/2}$. The contributions of the other particle-hole configuration are small (GI64). Thus the ground state (0^+) has the $p_{3/2}$ configuration coupled to the ^{11}B ground state, while the first excited (2^+) state has a large fraction of the $p_{1/2}$ component coupled to the

^{11}B ground state. At lower proton energies (BR72, WE82) the transitions to the ground and first excited states are mainly the $d_{5/2}\rightarrow p_{3/2}$ and $d_{3/2}\rightarrow p_{1/2}$ E1 transitions, respectively. The a_1,a_2 coefficients of the angular distributions are close to pure E1 values which are computed in subsection 4.3.1. Increasing the incident proton energy, the E2 transitions of $f_{7/2}\rightarrow p_{3/2}$ and $d_{5/2}\rightarrow p_{1/2}$ are admixed into the E1 transitions of $d_{5/2}\rightarrow p_{3/2}$ and $d_{3/2}\rightarrow p_{1/2}$, respectively. These admixtures give the similar angular dependence of the differential cross section for both transitions to the ground state and the first excited state, namely the broad peak at forward detection angles. At the medium energy region, the deviation of the a_1 and a_2 coefficients from the E1 value becomes larger because of the larger E2 admixture as increasing the incident proton energy (see Fig. 4.12).

Analyzing powers of the ^{11}B$(\vec{p},\gamma)^{12}$C reaction have been also measured at lower proton energies (GL72). The sign of measured coefficient b_2 for the γ-rays to the ground 0^+ state is just opposite to that for the γ-rays to the 2^+ state. The analyzing power of the transition to the 0^+ (i.e. $p_{3/2}$) increases with the increasing detection angle θ_γ, and that of the transition to the 2^+ (i.e. $p_{1/2}$) decreases with the increasing θ_γ. This feature seems to be preserved even at the present medium energy region of 40-50 MeV, but not at Ep=65 MeV. The measured coefficient (See Fig. 4.13) b_2 for the γ-rays to the ground 0^+ state is nearly equal to zero. On the other hand, the γ-rays to the 2^+ state has a finite b_2 value with positive sign. The E2 admixture into the E1 transitions gives the finite b_1 coefficient.

4.3.4 ^{12}C$(\vec{p},\gamma)^{13}$N (γ_f; the ground $1/2^-$ state, and γ_g; the 3.51 MeV $3/2^-$ and 3.55 MeV $5/2^+$ doublet states)

Within a framework of the p-shell, the configuration of the ^{13}N ground state with $J^{\pi}=1/2^-$ is the $(p_{3/2})^4 p_{1/2}$. Thus it is composed of the $p_{1/2}$ proton configuration coupled to the main configuration $(p_{3/2})^4$ of the ^{12}C ground state. The configuration of the second excited state (3.51 MeV $3/2^-$) of ^{13}N is the $(p_{3/2})^3 (p_{1/2})^2$. It is composed of the $p_{3/2}$ proton configuration coupled to the another configuration $(p_{3/2})^2 (p_{1/2})^2$ of the ^{12}C ground state. The configuration of the third excited state (3.55 MeV $5/2^+$) is the $d_{5/2}$ proton configuration coupled to the ^{12}C ground state. The energy difference between the second and third excited states is too small to be resolved in the present medium energy γ-ray spectrum. Actually one strong peak corresponding to the second $3/2^-$ and third $5/2^+$ excited states was observed. The yield of this strong peak is one order of magnitude larger than the γ-ray yield to the ground state with $1/2^-$. The strength of the γ radiation to the $3/2^-$ second excited state is evaluated to be about the same order as that to the $1/2^-$ ground state. Therefore the strong peak is considered to be predominantly due to the γ-radiation to the $5/2^+$ third excited state. The configurations for both the $3/2^-$ second excited state and the $5/2^+$ third excited state are the j-upper (j=l+1/2) one.

The angular dependences of the analyzing powers for the γ radiations to the $1/2^-$ and the $5/2^+$ are quite different from each other. The analyzing power of the γ-radiation to the $1/2^-$ (i.e. $p_{1/2}$) ground state decreases as the detection angle increases, and that to the $5/2^+$ (i.e. $d_{5/2}$) state increases. Both the ^{13}N ground state with $1/2^-$ and the ^{12}C first excited state with 2^+ are composed of the $p_{1/2}$ particle (proton) configuration coupled with the target nucleus of ^{12}C and ^{11}B, respectively. The b_2 coefficient of γ radiation to the ^{13}N $1/2^-$ state is larger than that to the ^{12}C 2^+ state, probably because the ^{13}N $1/2^-$ ground state is a pure $p_{1/2}$

particle state while the ^{12}C 2^+ state may be rather of mixed configurations. Comparing the $^{11}B(\vec{p},\gamma)^{12}C$ at Ep = 40 MeV with the $^{12}C(\vec{p},\gamma)^{13}N$ at the same energy, the analyzing power of the transition to the j-upper state increases as the detection angle increases, and that to the j-lower state decreases. This feature corresponds to a positive large b_2 coefficient for the transitions to the j-upper states and to a positive small or negative b_2 coefficient for the j-lower states (see Fig. 4.13). As mentioned in sub-section 4.3.2, a central potential may arise the b_2 coefficient from the difference of the phase shift for the $j+1$ wave and the $j-1$ wave.

4.3.5 $^{11}B(\vec{p},\gamma)^{12}C$ (γ_c; the 9.64 MeV 3^- state)

As for the γ_c, the 3^- state is not simply of a 1p-1h configuration, but rather of complicated configurations. At lower E_p (BR72), it has an appreciable admixture of the $d_{5/2} \rightarrow d_{3/2}$ M1 component into the $f_{7/2} \rightarrow d_{5/2}$ E1 component. Thus interpretation of the γ_c data is not simple.

4.3.6 $^{11}B(\vec{p},\gamma)^{12}C$ (γ_d; the 18.8 MeV region, γ_e; the 22.3 MeV region γ_h; the 10-18 MeV region and γ_i; the 25-35 MeV region)

The strong peak γ_d feeding the 18.8± 0.5 MeV region may correspond to the prominent γ peak feeding the 19.2± 0.6 MeV state observed in Ref K079. The broad peak γ_e feeding the 22.3± 1.0 MeV state shows up for the first time in the present spectrum. Let's consider microscopic configurations of the excitation energy region of γ_d and γ_e. Assuming a simple direct radiative proton capture process on the ^{11}B with the $(p_{3/2})^{-1}$ configuration, the final states are mainly of 1-particle 1-hole($p_{3/2}$) states. The particle-hole

configurations in the 18–23 MeV region have been studied by (e,e')(YA70,DO70b), (p,p')(BU77), (α,α')(BU77) and $(^3He,d)$(RE71) reactions and the RPA calculations(GI64, DO70a, RO70). As shown in Table 4.10 the $(J^\pi T)$= (2^-1), (3^-1), (4^-1), and (4^-0) states with mainly the $(d_{5/2})(p_{3/2})^{-1}$ configuration are located in the 18.3–19.8 MeV excitation region of γ_d. Therefore this peak is considered to be the γ-rays feeding these states. The $[(d_{5/2})(p_{3/2})^{-1}]_{4^-}$ configuration has been assigned to the 19.2± 0.6 MeV(KO79) state. Arnold(AR79) has assigned the $[(d_{5/2})(p_{3/2})^{-1}]_{4^-3^-2^-}$ configurations to this peak. On the other hand the 20.6–22.5 MeV excitation region of γ_e includes the (3^-0), (3^-1), (2^-0), and (2^-1) states with mainly the $(d_{3/2})(p_{3/2})^{-1}$ configuration as well as the (1^-1) state with the $(d_{5/2})(p_{3/2})^{-1}$ configuration (see in Table 4.10). The angular dependences of the differential cross section for the γ_d and γ_e are similar, suggesting similar E1 radiations with the E2 admixture as those for the low-lying peaks. Of great interest is the sharp contrast between the observed analyzing power for the γ_d and that for the γ_e (Figs. 4.6, 4.7). The b_2 coefficient of the γ_d is small and sign is positive or negative, while that of the γ_e is large and sign is positive. As mentioned above, the γ_d is the γ-ray feeding the excitaion region where the main configuration is $d_{5/2}(p_{3/2})^{-1}$, and the γ_e is the γ-ray feeding the excitaion region where the main configuration is $d_{3/2}(p_{3/2})^{-1}$. As we have pointed out in the previous sections, the analyzing powers for the $j_>(p_{3/2};\gamma_a,\gamma_g)$ orbits increase as a function of the detection angle, while those for the $j_<(p_{5/2};\gamma_b,\gamma_f)$ orbits decrease. Interesting is to note that those for the $d_{5/2}$ orbits $(j_>)$ increase as a function of the detection angle, and those for the $d_{3/2}$ orbits $(j_<)$ decrease (see Fig. 4.6, 4.7). On the other hand the observation that angular dependences of the cross-sections are very similar with each other may be interpreted by the

predominance of the E1 stretched transitions and admixture of the E2 transitions for both $j=l+1/2$ and $j=l-1/2$ final states.

4.3.7 The analyzing powers at Ep = 65 MeV

The angular dependences of the analyzing powers at Ep = 65 MeV show somewhat different pattern from those observed at lower proton energies. The calculation of the analyzing power including the contribution of the exchange current may be necessary to discuss whether this difference arises from its contribution or not.

4.4 Conclusion

The present work reports for the first time angular distributions and analyzing powers for medium energy γ-rays following interaction of medium energy (40-65 MeV) polarized protons. The newly developed HERMES with good energy resolution and good S/N ratio made it possible in practice to observe isolated γ-rays associated with radiative capture into shell model orbits with mainly the $p_{1/2}$, $p_{3/2}$, $d_{3/2}$ and $d_{5/2}$ configurations. The angular distributions of these γ-rays show similar forward peaking patterns with significant E1-E2 multipole mixing, while the analyzing powers depend on the final orbit of j-upper ($j_>=l+1/2$) or j-lower ($j_<=l-1/2$). This feature may be explained by the difference of the phase shift for the j+1 and j-1 initial waves. Analyzing power of the medium energy γ-rays associated with interaction of polarized protons is indeed a good probe to study the microscopic nucleon configuration. The medium energy γ-radiation far beyond the GDR is considered to be mainly due to the direct process (TS79, GA78, AR79) with appreciable contribution of the exchange current (GA78, HE76, GA74). Extensive studies of such energetic γ-rays are interesting to clarify the relevant radiation mechanism as well as the nuclear structure.

5.1 Summary

The new data acquisition system was successfully developed in this work. The unique points of this system are as follows. i) This system can handle up to 63 parameters and 2^{15} combinations of the events. ii) This system can handle the CAMAC system. Therefore the fast signal processing becomes possible. iii) It is easy to use this system for beginners by the event descriptor table handling system.

In order to measure the medium energy γ-rays using the HERMES, the improvements of electronics and the development of the data reduction algorithm were successfully completed in this work. By using the CAMAC and new data acquisition system, pile-up rejection and neutron rejection became possible. They were indispensable for measurements of the medium energy γ-rays. A new way of rejecting cosmic rays was developed. We found that the cosmic rays can be rejected almost 100 % by rejecting the events with large energy deposit ($E_a \geqq 8$ MeV) in any one segment of the annular NaI segments. A peak fit program and other utility programs were developed.

In order to measure the analyzing power, a beam polarimeter was set up at the F beam line in RCNP.

The angular dependences of both the differential cross section and the analyzing power for the radiative capture of polarized protons were successfully measured for the first time by means of the HERMES in the medium energy region (E_γ=40~80 MeV). Several discrete γ-ray peaks from the $^{11}B(\vec{p},\gamma)$ reaction and the $^{12}C(\vec{p},\gamma)$ reaction are evidently seen. The 22.3± 1.0 MeV peak in ^{12}C was observed for the first time in this work.

The angular distributions of these γ-rays show a similar pattern with a broad bump at forward detection angles. This pattern may arise from admixture

of the stretched E2 ($j+2\rightarrow j$) radiation into the stretched E1 ($j+1\rightarrow j$) radiation.

Angular dependences of the analyzing powers for these γ-rays show very different patterns from each other. Some increase with the increasing detection angle, and the others decrease. The analyzing powers of the γ-rays to low-lying states, configuration of which are well known, may be classified into two groups, one pattern for the γ radiation feeding the j-upper ($j=l+1/2$) particle states and another one for the γ radiation feeding the j-lower ($j=l-1/2$) particle states. In addition to this, the analyzing powers of the γ-rays to high-lying states, configurations of which are known from other reaction studies, may also be classified into the two groups.

The present work demonstrated importance of the measurements of the analyzing power in the medium energy region in order to study the microscopic nucleon configurations.

5.2 Remarks

The new data acquisition system developed in this work is very flexible for the on-line data processing, and its functions will be sufficient to most of nuclear physics experiments for several years. However, some day, they will become insufficient for future sophisticated experiments. At that time one will, in principle, be able to reform the system. The reformation, however, is not quite convenient because our system is almost of a maximum size which can use the menu selection method. Therefore some computer language will become necessary to describe the on-line data processing.

In this work, the new method of the cosmic ray rejection without plastic shields was developed. The division of the NaI crystal make it possible, as described in section 3.2. The peak efficiency of the HERMES without the Compton suppression is not as good as that of previous large volume NaI crystals, and the energy resolution is better than those. One can use this NaI ensemble without the plastic scintillator shield for low energy γ-ray measurements. In this case one can use small outer lead shields, reducing the total weight of the γ-ray detector and increasing the target accessibility.

We show the advantage of a multi-parameter (multi-segments) detector in this work. Redundancy of a multi-parameter detector is very useful for the severe event selection. This philosophy can be applied for other detectors.

The gain shift of the HERMES is not negligible. Thus some improvement of the gain stabilizer is necessary. There are two references to monitor the PMT gain. i) Photo pulser : Light from an LED is used as a reference. In order to use the LED, some modification of the assemble of the NaI ensemble will be necessary. ii) Low energy γ-rays : We used the 4.4 MeV γ-rays as a reference for the low energy γ-ray measurements. The hard-ware gain stabilizer did not

work well because of the unstable beam current and the large background. Therefore one needs so intelligent gain stabilizer as to adjust the time interval of correction of the gain according to the beam intensity and to determine the amounts of the gain correction by the peak fitting. Such intelligent stabilizer can endure the large background.

The observed γ-ray yields increase with the increasing the excitation energy of the final states beyond the proton threshold energy. This feature does not depend much on the target nuclear species and the incident proton energy. The (p,γp') reaction channel opens above the proton threshold. This reaction may increase the γ-ray yields beyond the proton threshold energy. As shown in this work, measurements of the analyzing power may be also a good tool to study this mechanism by comparing the measured data with direct process calculations using continuum final state wave functions.

A scattering process of the incident proton is strong, because it is due to a strong interaction. The scattering process may occur either before or after the γ radiation. Such two-step processes may be appreciable. As mentioned in Chapter I, the simple direct capture (one-body radiation) probability decreases with the increasing energy of the incident proton, because of the momentum mismatching between the incident nucleon and the out-going γ-ray. On the other hand, the two step processes are favorable in view of the momentum matching. In the simple direct capture process, single particle (hole) states dominate the final states. Two-step processes, however, are likely to feed collective states. Thus the coupling of the angular momenta for these processes may be quite different from each other. Since the measurement of the analyzing power is sensitive to the coupling of the angular momenta, it is a powerful method for study of this mechanism.

As mentioned in section 4.3.7, the angular dependence of the analyzing

powers at Ep = 65 MeV shows somewhat different pattern from those observed at lower proton energies. This may be due to the effect of the exchange current. The exchange current effect is essentially two-body process. It changes the quantum state of the target as well. Thus the angular dependence of the analyzing powers may be different from the simple direct one-body process where the target nucleus remains unchanged as a spectator. The calculation of the analyzing power including the contribution of the exchange current is necessary.

AR79 L.G. Arnold, Phys. Rev. Lett. 42, 1253 (1979).

BL79 S.L. Blatt, M.A. Kovash, R.N. Boyd, T.R. Donoghue, H.J. Hausman, A.D. Bacher and C.C. Foster, IUCF annual report 1979.

BR64 G.E. Brown, Nucl. Phys. 57, 339 (1964).

BR72 C. Brassard, H.D. Shay, J.P. Coffin, W. Scholz, and D.A. Bromley, Phys. Rev. C6, 53 (1972).

BU77 M. Buenerd, P. Martin, P. de Saintignon, and J.M. Loiseaux, Nucl. Phys. A286, 377 (1977).

CA71 R.W. Carr and J.E.E. Banglin, Nuclear Data Table 10, 143 (1971).

CO82 M.T. Collins, S. Manglos, N.R. Roberson, A.M. Sandrifi and H.R. Weller, Phys. Rev. C26, 332 (1982).

DA71 W.F. Davidson, J.L. Black and M.R. Najam, Nucl. Phys. A168, 339 (1971).

DI70 E.M. Diener, J.F. Amann, S.L. Blatt and P. Paul, Nucl. Instr. and Meth. 83, 115 (1970).

DO68 T.W. Donnelly, Phys. Rev. Lett. 21, 1196 (1968).

DO70a T.W. Donnelly, Phys. Rev. C1, 833 (1970).

DO70b T.W. Donnelly, Ann. Phys. (N.Y.), 60, 209 (1970).

GA74 M. Gari and H. Hebach, Phys. Lett. 49B, 29 (1974).

GA78 M. Gari and H. Hebach, Phys. Rev. C18, 1071 (1978).

GI64 V. Gillet and N. Vinh Mau, Nucl. Phys. 54, 321 (1964).

GL72 H.F. Glavish, S.S. Hanna, R. Avida, R.N. Boyd, C.C. Chang, and D. Diner, Phys. Rev. Lett. 28, 766 (1972).

HA74 M. Hashinoff, S.T. Lim, D.E. Meusday and T.L. Mulligan, Nucl. Instr. and Meth. 117, 375 (1974).

HA80 R. Hayano and J. Chiba, (private communication 1980)

HA81 D. Halderson and R.J. Philpott, Phys. Rev. Lett. 46, 100(1981).

HA82 R. Hayano and J. Chiba, *Butsuri* 37, 936 (1980).

HE76 H. Hebach, A. Wortberg, and M. Gari, Nucl. Phys. A267, 425 (1976).

KA80i I.Katayama and H. Ogata, Nucl. Instr. and Meth. 174, 295 (1980).

KA80s S. Kato, K.Okada, M. Kondo, A. Shimizu, K. Hosono, T. Saito, N. Matsuoka, S. Nagamachi, K. Nishimura, N. Tamura, K. Imai, K. Egawa, M. Nakamura, T. Noro, H. Shimizu, K. Ogino and K. Kadota, Nucl. Instr. and Meth. 169, 589 (1980).

KE70 G. Kernel, W.W. Mason and N.W. Tanner, Nucl. Instr. and Meth. 89, 1 (1970).

KI80 T. Kishimoto Ph.D. thesis Osaka Univ., (1980).

KI82 T. Kishimoto, T. Shibata, M. Sasao, M. Noumachi, and H. Ejiri, Nucl. Instr. and Meth. 198, 269 (1982).

KO79 M.A. Kovash, S.L. Blatt, R.N. Boyd, T.R. Donoghue and H.J. Hausman, Phys. Rev. Lett. 42, 700 (1979).

LA77 R.M. Laszewski and R.J. Hot, Atomic Data and Nuclear Data Table 19, 305 (1977).

LO82 J.T. Londergan and L.D. Ludeking, Phys. Rev. C25, 1722 (1982).

MA81 S. Manglos, N.R. Roberson and H.R. Weller, Phys. Rev. C24, 2378 (1981).

MO79 J.E. Monahan, R.J. Hot and R.M. Laszewski, Atomic Data and Nuclear Data Table 23, 97 (1979).

OG80 H. Ogata and I. Katayama, *Genshikaku Kenkyu* 25, 2 (1980).

OH82 H. Ohsumi (Private communication 1982)

RE71 G.M. Reynolds, D.E. Rundquist, and R.M. Poichar, Phys. Rev. C3, 442 (1971).

RO70 D.J. Rowe and S.S.M. Wong, Nucl. Phys. A153, 561 (1970).

SA79 F. Saporetti and R. Guidotti, Nucl. Phys. A330, 53 (1979).

SH74 A. de Shalt and H. Feshbach, *Theorelical Nuclear Physics* Vol. 1, John Wiley & Sons Inc., New York, 1974.

SN77 K.A. Snover, P. Paul, H.M. Kuan, Nucl. Phys. A285, 189 (1977).

SU68 M. Suffert, W. Feldman, T. Makieux and S.S. Hanna, Nucl. Instr. and Meth. 63, 1 (1968).

TS79 S.F. Tsai and J.T. Londergan, Phys. Rev. Lett. 43, 576 (1979).

WE82 H.R. Weller, H. Hasan, S. Manglos, G.Mitev, N.R. Roberson, S.L. Blatt, H.J. Hausman, R.G. Seyler, R.N.Boyd, T.R. Donoghue, M.A. Kovash, A.D. Bacher and C.C. Foster, Phys. Rev. C25, 2921 (1982).

YA70 A. Yamaguchi, T. Terasawa, K.Nakahara, and Y. Torizuka, Phys. Rev. C3, 1750 (1970).

YA76 T. Yamazaki, I. Katayama and H. Ogata, RCNP annual report 1976, p. 159.

A.1 Angular distribution of γ-rays from the polarized proton radiative capture reaction

A.1.1 Target spin 0 We use a simple direct capture model, where a target nucleus is a spectator, and the quantum state of the target nucleus does not change through the radiation. We proceed the calculation according to Ref. SH74 for a spin zero target nucleus from an equation,

$$M_{fi}(\vec{k}\sigma) = -\frac{1}{16\pi^2}\sqrt{\hbar/\omega_k}\sum_{\lambda\mu\sigma'}\hat{\lambda}\,[D^{\lambda *}_{\mu 1}(\vec{k})+(-)^{\sigma+\sigma'}D^{\lambda *}_{\mu,-1}(\vec{k})]\,\langle f\,|\,M^{(\sigma')}_{\lambda\mu}\,|\,i\rangle. \qquad (A.1)$$

Here $M_{fi}(\vec{k}\sigma)$ is a transition matrix element for radiation. Momentum of photon is $\vec{k}$ and helicity is σ. $M^{\sigma'}_{\lambda\mu}$ is a operator corresponding to the radiation of the photon of which angular momentum is $|\lambda\mu\rangle$ and parity is $(-)^{\lambda+\sigma'}$. $\hat{\lambda}$ is defined as:

$$\hat{\lambda} = \sqrt{2\lambda+1} \qquad (A.2)$$

D is the D-function. An initial state φ_i is described as:

$$\varphi_i=\sum_{lj}\hat{l}\hat{j}\,(-)^{l-1}\begin{bmatrix} l & 1/2 & j \\ 0 & 1/2 & -1/2\end{bmatrix}\{P_+\,|\,j\,l\,1/2\rangle+(-)^{l+j-1/2}P_-\,|\,j\,l-1/2\rangle\} \qquad (A.3)$$

Beam direction is chosen as Z-axis. $\vec{P}$ is the beam polarization. P_+ and P_- are its projections to the spherical tensor. Detecting the γ-ray at an angle (θ,φ),

$$\vec{P}\,\vec{n} = \frac{1}{2}\,(\sigma_x sin\varphi - \sigma_y cos\varphi)$$

$$= \frac{i}{4}\,(\sigma_+ e^{-i\varphi}-\sigma_- e^{i\varphi}). \qquad (A.4)$$

Here, $\vec{n}$ is the unit vector, which is normal to the reaction plane, and defined as:

$$\vec{n} = \frac{\vec{k}_p \times \vec{k}_\gamma}{|\vec{k}_p \times \vec{k}_\gamma|}. \tag{A.5}$$

The expectation value of $\vec{p} \cdot \vec{n}$ for the initial state is

$$\langle \vec{p} \cdot \vec{n} \rangle = \frac{i}{2} \left(e^{-i\varphi} P_+^\dagger P_- - e^{i\varphi} P_-^\dagger P_+ \right). \tag{A.6}$$

For the normalization

$$P_+^\dagger P_+ + P_-^\dagger P_- = 1. \tag{A.7}$$

A single particle final state φ_f is defined as :

$$\varphi_f = | j_f l_f m_f \rangle. \tag{A.8}$$

Inserting eq. (A.8) and eq. (A.3), and using the Wigner-Eckart theorem eq. (A.1) yields

$$M_{fi} = -\frac{1}{16\pi^2}\sqrt{\hbar/\omega_k} \sum_{\substack{\lambda\mu\alpha' \\ lj}} \hat{\lambda}\hat{l}\hat{j}\,(-)^l \begin{bmatrix} l & 1/2 & j \\ 0 & 1/2 & -1/2 \end{bmatrix} \left[D^{\lambda *}_{\mu 1} + (-)^{\alpha+\alpha'} D^{\lambda *}_{\mu,-1} \right]$$

$$\cdot (-)^{j_f - m_f} \left\{ \begin{bmatrix} j_f & \lambda & j \\ -m_f & \mu & 1/2 \end{bmatrix} P_+ + (-)^{l+j+1/2} \begin{bmatrix} j_f & \lambda & j \\ -m_f & \mu & -1/2 \end{bmatrix} P_- \right\}$$

$$\cdot \langle f \| M^{(\alpha')}_{\lambda\mu} \| i \rangle. \tag{A.9}$$

The differential cross section of the radiative capture reaction is

$$\frac{d\sigma}{d\Omega} = \frac{2\pi}{\hbar}\frac{k_\gamma^2}{\hbar c}\frac{m_p}{k_p\hbar}|M_{fi}|^2 \qquad (A.10)$$

where $\hbar k_\gamma$ and $\hbar k_p$ are linear momenta of the photon and the proton, respectively. The m_p is the reduced proton mass. Inserting eq. (A.9) into eq. (A.10) and summing up over the helicity σ and the final state magnetic substate m_f, because neither σ nor m_f are observed, one gets

$$\sum_{\substack{\lambda_1\sigma'_1\lambda_2\sigma'_2\\ l_1 j_1 l_2 j_2}} \hat{\lambda_1}\hat{\lambda_2}\hat{j_1}\hat{j_2}\hat{l_1}\hat{l_2}(-)^{l_1+l_2}\begin{bmatrix} l_1 & 1/2 & j_1 \\ 0 & 1/2 & -1/2 \end{bmatrix}\begin{bmatrix} l_2 & 1/2 & j_2 \\ 0 & 1/2 & -1/2 \end{bmatrix}$$

$$\langle f\|M^{(\sigma'_1)}_{\lambda_1\mu}\|j_1 l_1\rangle\langle f\|M^{(\sigma'_2)}_{\lambda_2\mu}\|j_2 l_2\rangle \sum_{\mu_1\mu_2 m_f}(D^{\lambda_1}_{\mu_1 1}D^{\lambda_2}_{\mu_2 1}+(-)^{\sigma'_1+\sigma'_2}D^{\lambda_1}_{\mu_1 -1}D^{\lambda_2 *}_{\mu_2 -1})$$

$$\times\{\begin{bmatrix} j_f & \lambda_1 & j_1 \\ -m_f & \mu_1 & 1/2 \end{bmatrix}P^*_+ + (-1)^{l_1+j_1-1/2}\begin{bmatrix} j_f & \lambda_1 & j_1 \\ -m_f & \mu_1 & -1/2 \end{bmatrix}P^*_-\}$$

$$\times\{\begin{bmatrix} j_f & \lambda_2 & j_2 \\ -m_f & \mu_2 & 1/2 \end{bmatrix}P_+ + (-1)^{l_2+j_2-1/2}\begin{bmatrix} j_f & \lambda_2 & j_2 \\ -m_f & \mu_2 & -1/2 \end{bmatrix}P_-\}. \qquad (A.11)$$

where factor

$$\frac{2\pi}{\hbar}\frac{k_\gamma^2}{\hbar c}\frac{m_p}{k_p\hbar}\left(\frac{1}{16\pi^2}\right)^2\frac{\hbar}{\omega_k} \qquad (A.12)$$

is omitted. The product of D-function is reduced to an expansion of single D-functions.

$$D^{\lambda_1}_{\mu_1 1}D^{\lambda_2 *}_{\mu_2 1}+(-)^{\sigma'_1+\sigma'_2}D^{\lambda_1}_{\mu_1 -1}D^{\lambda_2 *}_{\mu_2 -1}$$

$$= \begin{cases} 2\cdot(-)^{\mu_2-1}\sum_k \hat{k}^2 \begin{bmatrix} \lambda_1 & \lambda_2 & k \\ 1 & -1 & 0 \end{bmatrix} \begin{bmatrix} \lambda_1 & \lambda_2 & k \\ \mu_1 & -\mu_2 & m_k \end{bmatrix} d^k_{m_k 0} \\ \qquad\qquad for \quad \sigma'_1+\sigma'_2+\lambda_1+\lambda_2+k = even \\ 0 \qquad\qquad for \quad \sigma'_1+\sigma'_2+\lambda_1+\lambda_2+k = odd \end{cases} \tag{A.13}$$

Rewriting the eq. (2.93) of ref. SH74 p929, one gets

$$\sum_{m_f\mu_1\mu_2} (-)^{\mu_2-1} \begin{bmatrix} j_f & \lambda_1 & j_1 \\ -m_f & \mu_1 & s_1 \end{bmatrix} \begin{bmatrix} j_f & \lambda_2 & j_2 \\ -m_f & \mu_2 & -s_2 \end{bmatrix} \begin{bmatrix} \lambda_1 & \lambda_2 & k \\ \mu_1 & -\mu_2 & m_k \end{bmatrix}$$

$$= (-)^{j_1+j_2-j_f-s_2-m_k-1} \begin{Bmatrix} j_1 & j_2 & k \\ \lambda_2 & \lambda_1 & j_f \end{Bmatrix} \begin{bmatrix} j_1 & j_2 & k \\ s_1 & s_2 & -m_k \end{bmatrix}. \tag{A.14}$$

Inserting eq. (A.13) and eq. (A.14) into eq. (A.11), one gets

$$2\cdot\sum \hat{\lambda}_1\hat{\lambda}_2\hat{j}_1\hat{j}_2\hat{l}_1\hat{l}_2\hat{k}^2 (-)^{l_1+l_2+j_1+j_2} \langle 1\rangle^* \langle 2\rangle$$

$$\cdot \begin{bmatrix} l_1 & 1/2 & j_1 \\ 0 & 1/2 & -1/2 \end{bmatrix} \begin{bmatrix} l_2 & 1/2 & j_2 \\ 0 & 1/2 & -1/2 \end{bmatrix} \begin{bmatrix} \lambda_1 & \lambda_2 & k \\ -1 & 1 & 0 \end{bmatrix} \begin{Bmatrix} j_1 & j_2 & k \\ \lambda_2 & \lambda_1 & j_f \end{Bmatrix}$$

$$\times \{ \begin{bmatrix} j_1 & j_2 & k \\ 1/2 & -1/2 & 0 \end{bmatrix} (-)^{j_f+1/2} P^+_+ P_+ D^k_{0\,0}$$

$$+ (-)^{l_1+l_2+j_1+j_2-1} \begin{bmatrix} j_1 & j_2 & k \\ -1/2 & 1/2 & 0 \end{bmatrix} (-)^{j_f-1/2} P^+_- P_- D^k_{0\,0}$$

$$+(-)^{l_1+j_1-1/2}\begin{bmatrix} j_1 & j_2 & k \\ -1/2 & -1/2 & 1 \end{bmatrix}(-)^{j_f-1/2}P_-^{\dagger}P_+D_{-1\ 0}^{k}$$

$$+(-)^{l_2+j_2-1/2}\begin{bmatrix} j_1 & j_2 & k \\ 1/2 & 1/2 & -1 \end{bmatrix}(-)^{j_f+1/2}P_+^{\dagger}P_-D_{1\ 0}^{k}\}. \qquad (A.15)$$

where $< m >$ is $<j_f l_f \| M_m^{\lambda\sigma'} \| j_i l_i>$. First two terms in { } of eq. (A.15) become

$$(-)^{j_f+1/2}\begin{bmatrix} j_1 & j_2 & k \\ 1/2 & -1/2 & 0 \end{bmatrix}D_{00}^{k}(P_+^{\dagger}P_+ + (-)^{l_1+l_2+k}P_-^{\dagger}P_-). \qquad (A.16)$$

l_1+l_2+k must be even to make the parity (Π_f) of the residual nucleus definite, as follows.

$$\Pi_f(-)^{\lambda_1+\sigma'_1}=(-)^{l_1} \quad and \quad \Pi_f(-)^{\lambda_2+\sigma'_2}=(-)^{l_2}$$

Therefore $l_1+l_2-(\lambda_1+\sigma'_1+\lambda_2+\sigma'_2)$ is even. Using $\lambda_1+\lambda_2+\sigma'_1+\sigma'_2+k$ = even, the l_1+l_2+k is also even. Inserting this and eq. (A.7), (A.16) yields

$$(-)^{j_f+1/2}\begin{bmatrix} j_1 & j_2 & k \\ 1/2 & -1/2 & 0 \end{bmatrix}D_{00}^{k}. \qquad (A.17)$$

Last two terms in { } of eq. (A.15) become

$$(-)^{j_f+l_1+j_1+1}\begin{bmatrix} j_1 & j_2 & k \\ -1/2 & -1/2 & 1 \end{bmatrix}\{P_-^{\dagger}P_+D_{-1\ 0}^{k}+(-)^{l_1+l_2+k}P_+^{\dagger}P_-D_{1\ 0}^{k}\}. \qquad (A.18)$$

Using $D_{m0}^{k}=e^{-im\varphi}d_{m0}^{k}$ and the l_1+l_2+k=even, eq. (A.18) becomes

$$(-)^{j_f+l_1+j_1+1}\begin{bmatrix} j_1 & j_2 & k \\ -1/2 & -1/2 & 1 \end{bmatrix} d^k_{10}\,(e^{-i\varphi}P^+_+P^+_- - e^{i\varphi}P^+_-P^+_+). \tag{A.19}$$

Inserting eq. (A.6) into eq. (A.19) yields

$$2i\,(-)^{j_f+l_1+j_1+1}\begin{bmatrix} j_1 & j_2 & k \\ -1/2 & -1/2 & 1 \end{bmatrix} d^k_{10}\langle \vec{P}\cdot\vec{n}\rangle . \tag{A.20}$$

Using the recursion relation of 3-j

$$\begin{bmatrix} j_1 & j_2 & k \\ -1/2 & -1/2 & 1 \end{bmatrix} = -\begin{bmatrix} j_1 & j_2 & k \\ 1/2 & -1/2 & 0 \end{bmatrix}\frac{\{(j_1+1/2)+(-)^{j_1+j_2+j}(j_2+1/2)\}}{\hat{k}} \tag{A.21}$$

is derived. Then eq. (A.20) is rewritten as

$$2i\,(-)^{j_f+l_1+j_1}\begin{bmatrix} j_1 & j_2 & k \\ 1/2 & -1/2 & 0 \end{bmatrix} d^k_{10}\langle \vec{p}\cdot\vec{n}\rangle \frac{\{(j_1+1/2)+(-)^{j_1+j_2+j}\cdot(j_2+1/2)\}}{\hat{k}}$$

$$=2i\,(-)^{j_f+1/2}\begin{bmatrix} j_1 & j_2 & k \\ 1/2 & -1/2 & 0 \end{bmatrix} d^k_{10}\langle \vec{p}\cdot\vec{n}\rangle$$

$$\{-\frac{j_2(j_2+1)-l_2(l_2+1)-j_1(j_1+1)+l_1(l_1+1)}{\hat{k}}\} \tag{A.22}$$

Using the (2.93) of ref. SH74 p929,

$$\begin{Bmatrix} l_1 & l_2 & k \\ j_2 & j_1 & 1/2 \end{Bmatrix}\begin{bmatrix} l_1 & l_2 & k \\ 0 & 0 & 0 \end{bmatrix} = 2(-)^{j_1+j_2}$$

$$\times\begin{bmatrix} l_1 & 1/2 & j_1 \\ 0 & 1/2 & -1/2 \end{bmatrix}\begin{bmatrix} l_2 & 1/2 & j_2 \\ 0 & 1/2 & -1/2 \end{bmatrix}\begin{bmatrix} j_1 & j_2 & k \\ 1/2 & -1/2 & 0 \end{bmatrix} \tag{A.23}$$

Consequently, inserting eqs. (A.17,A.22 and A.23), eq. (A.15) yields

$$\sum \hat{\lambda}_1 \hat{\lambda}_2 \hat{j}_1 \hat{j}_2 \hat{l}_1 \hat{l}_2 \hat{k}^2 (-)^{l_1+l_2+j_1+j_2} \langle 1 \rangle^* \langle 2 \rangle$$

$$\cdot \begin{Bmatrix} l_1 & l_2 & k \\ j_2 & j_1 & 1/2 \end{Bmatrix} \begin{Bmatrix} \lambda_1 & \lambda_2 & k \\ -1 & 1 & 0 \end{Bmatrix} \begin{bmatrix} l_1 & l_2 & k \\ 0 & 0 & 0 \end{bmatrix} \begin{bmatrix} j_1 & j_2 & k \\ \lambda_2 & \lambda_1 & j_f \end{bmatrix}$$

$$\times \{ d^k_{0\,0} - \frac{j_2(j_2+1) - l_2(l_2+1) - j_1(j_1+1) + l_1(l_1+1)}{\hat{k}} 2i\ \vec{p} \cdot \vec{n}\ d^k_{1\,0} \} \qquad (A.24)$$

These values are tabulated in ref. CA71, LA77 and MO79. However definition of a phase of the reduced matrix element is different.

A.1.2 Reduced matrix elements

We evaluate the reduced matrix elements using the long wave length approximation. The operator $M^{(E)}_{\lambda\mu}$ becomes

$$M^{(E)}_{\lambda\mu} = 8\pi^{4}\frac{C}{\hat{\lambda}}\frac{k_{\gamma}^{\lambda}}{(2\lambda+1)!!}\sqrt{(\lambda+1)/\pi\lambda}\int(-ir)^{\lambda}Y^{*}_{\lambda\mu}\rho^{(E)}dr \qquad (A.25)$$

The (2.49) in ref. SH74 p923 is rewritten as

$$<1/2l_{f}j_{f}\|Y^{*}_{\lambda}\|1/2lj>=(-)^{j_{f}-1/2}i^{l_{f}-\lambda-l}\hat{\lambda}/\sqrt{4\pi}\ Z(l_{f}j_{f}lj;{}^{1}/_{2}\ \lambda). \qquad (A.26)$$

Z is the Z-coefficient (see eq. (7) of ref. CA71). Using eq. (A.25) and eq. (A.26), the reduced matrix element becomes

$$<\|M^{(E)}_{\lambda}\|> =$$

$$4\pi^{3}\frac{e\ c\ k_{\gamma}^{\lambda}}{(2\lambda+1)!!}\sqrt{(\lambda+1)/\lambda}\,(-)^{j_{f}-1/2}\ i^{l-l_{f}}Z(l_{f}j_{f}lj;{}^{1}/_{2}\ \lambda)\int\varphi^{*}_{f}r^{\lambda}\varphi_{i}dr. \qquad (A.27)$$

A.1.3 Target spin j_0

When the target has spin j_0, the cross section for the radiative capture into the final state J is derived as follows. Incident proton of total spin j radiates the γ-ray and drops into the j_1 orbit. The final state is written as

$$|J\ M\rangle=\sum_{m_0}\langle j_0\ m_0\ j_1\ M-m_0|J\ M\rangle|j_0\ m_0\rangle\cdot|j_1\ M-m_0\rangle \tag{A.28}$$

The transition probability becomes

$$\sum_{M}|\langle JM|T|jm\rangle\cdot|j_0m_0\rangle|^2$$

$$=\sum_{m_0\ m_0'}\langle j_0\ m_0\ j_1\ M-m_0|J\ M\rangle\langle j_0\ m_0'\ j_1\ M-m_0'|J\ M\rangle$$

$$\langle j_1\ M-m_0|T|j\ m\rangle^*\langle j_1\ M-m_0'|T|j\ m\rangle$$

$$=\frac{2J+1}{2J_1+1}\sum_{m_0}|\langle j_1\ M-m_0|T|j\ m\rangle|^2. \tag{A.29}$$

We may average eq. (A.29) over m_0 (initial state magnetic substate)

$$\frac{2J+1}{(2j_1+1)(2j_0+1)}\sum_{m_0}|\langle j_1\ M-m_0|T|j\ m\rangle|^2 \tag{A.30}$$

The summation in eq. (A.30) is just equal to the transition probability of the target spin 0.

$\sigma(Target\ spin\ j_0,\ Final\ spin\ J)$

$$=\frac{2J+1}{(2j_1+1)(2j_0+1)}\times\sigma(Target\ spin\ 0,\ Final\ spin\ j_1) \tag{A.31}$$

Figure captions

Fig. 1.1. Schematic diagram for radiative capture reaction. a). Simple direct process (one body process). b). Semi-direct process. c). Exchange current effect (two body process).

Fig. 1.2. Schematic diagram for comparison of medium energy radiative capture reaction to low energy radiative capture reaction.

Fig. 2.1. A block diagram of the new data acquisition system. It consists of three processors, which correspond to "task"s. The raw data are acquired by the data processor through the MBD-11 and CAMAC system, and they are stored in the raw data buffer. The data processor writes these data on a magnetic tape, and derives the histogram from the raw data according to the prescription of the EDT. The command processor displays this histogram on the graphic display. Commands from the key-board are interpreted by the command processor. According to this command, the command processor controls the data processor. The ETHS creates and modifies the EDT interactively.

Fig. 3.1. Schematic description of eq. 3.1. "F" is the full energy loss spectrum, where the γ-ray energy is fully absorbed in the NaI. "E" is the NaI spectrum where some photons escape from NaI. "A" is the accepted NaI spectrum, which is taken in anti-coincidence with signals from the plastic scintillators. "R" is the rejected NaI spectrum, which is taken in coincidence with signals from the plastic scintillators. Factor f is the detection efficiency of the plastic scintillators for escaping photons.

Fig. 3.2. Sectional layout of the HERMES. The 29.7 cm $\phi \times$ 29.7 cm (11"$\phi \times$11") NaI(Tl) crystal is divided into five segments. Each

part is optically isolated by 1.5 mm MgO layers. The whole NaI(Tl) assembly is packed in a 3 mm thick aluminum can.

Fig. 3.3. A spectrum of energy distributed on the annular 29.7 cm $\phi \times$ 29.7 cm (11"$\phi \times$11") crystal for the central NaI signals above 14.5 MeV in the $^{12}C(p,\gamma)^{13}N$ reaction at E_p=50 MeV.

Fig. 3.4. Schematic response functions for a small volume NaI, Previous single crystal NaI with large volume and the HERMES.

Fig. 3.5. Schematic diagram of the basic electronics used for the HERMES.

Fig. 3.6. Schematic diagram of the pile up rejection. Up-dating discriminator (EG&G T122/NL) is used as retriggerable astable flip-flop. Dual 4-fold majority logic units (LeCroy 365AL) with veto are used as logic elements in figure.

Fig. 3.7. Schematic diagram of the electronics used for the HERMES. This includes the pile-up rejection circuit and the on-line neutron rejection circuit. A 16 fold register (LeCroy 2341A) is described as "16 f." or "16 fold" in the figure. "QC" is a quad coincidence (LeCroy 622). "ML" is a dual 4-fold majority logic unit (LeCroy 365AL). "UD" is up-dating discriminator (EG&G T122/NL). "LiF" is linear fan-in / fan-out (LeCroy 428F). "LoF" is logical fan-in / fan-out (LeCroy 429F). Dual gate and delay generator (LeCroy 222) is described as "G.G." or "BUSY".

Fig. 3.8. A main routine of the off-line data reduction program. Raw data for each event is read from a magnetic tape on the common area /EVENT/ by the subroutine "EVREAD". The data reduction parameters such as the TOF γ window etc. are read from the file on the common area /PARAM/ by the subroutine "GETPRM". This is written in FORTRAN-77.

Fig. 3.9. Typical peak fitting result for the $^{11}B(p,\gamma)$ reaction. The $\gamma_a, \gamma_b, \gamma_c$ and the γ-ray feeding the second 0^+ are fitted at the same time. The fitted region is shown in Fig.. The parameters used are P_1= 448.6 channel, P_2= 6.905 channel/MeV, P_3= 5.683 MeV, P_4= 0.908, P_5= 0.77 MeV^{-1} and P_6= 2.1.

Fig. 4.1. (*a*), (*b*): A time of flight spectrum measured by the central NaI for the $^{11}B(p,\gamma)$ reaction at Ep = 40 MeV and θ_{lab}=60° . The central NaI signals above 14.5 MeV are selected. (*b*): Most neutron events with the flight time beyond the threshold T_n (see arrow in Fig.) were not recorded in the on-line data acquisition. The FWHM of 3.0 nsec includes the 2.6 nsec beam width.

Fig. 4.2. Gamma ray energy spectrum for the $^{11}B(p,\gamma)$ reaction at Ep = 50 MeV and θ_{lab}=40° .

Fig. 4.3. Differential cross sections for the radiative capture of the 40 MeV polarized protons on ^{11}B and ^{12}C. The solid lines show the Legendre fitting. Errors given are statistical ones. The systematic error for the absolute cross-sections due to the target thickness, the efficiency of the HERMES, and the beam current integration amounts to about 20-30 %.

Fig. 4.4. Differential cross-sections for the radiative capture of the 50 MeV polarized protons on ^{11}B. The solid lines show the Legendre fitting. The dashed line shows the calculated value, where the angular distributions in Ref. GA76 are normalized to the Ref. TS79. Errors given are statistical ones. The systematic error for the absolute cross-sections due to the target thickness, the efficiency of the HERMES, and the beam current integration amounts to about 20-30 %.

Fig. 4.5. Differential cross-sections for the radiative capture of the 65 MeV polarized protons on ^{11}B. The solid lines show the Legendre fitting. Errors given are statistical ones. The systematic error for the absolute cross-sections due to the target thickness, the efficiency of the HERMES, and the beam current integration amounts to about 20-30 %.

Fig. 4.6. Analyzing powers for the radiative capture of the 40 MeV polarized protons on ^{11}B and ^{12}C. Solid lines show the Legendre fitting. Statistical errors are shown.

Fig. 4.7. Analyzing powers for the radiative capture of the 50 MeV polarized protons on ^{11}B. Solid lines show the Legendre fitting. Statistical errors are shown.

Fig. 4.8. Analyzing powers for the radiative capture of the 65 MeV polarized protons on ^{11}B. Solid lines show the Legendre fitting. Statistical errors are shown.

Fig. 4.9. Gamma ray energy spectrum for the $^{12}C(p,\gamma)$ reaction at Ep = 40 MeV and $\theta_{lab}=60^{\circ}$.

Fig. 4.10. Angular distributions with the Legendre expansion and the measured differential cross sections. Angular distributions with coefficients of $a_1=0.0$, $a_2=-0.294$ and $a_1=0.85$, $a_2=-0.18$ are compared with observed angular distribution of the γ-rays following the $^{12}C(p,\gamma)^{13}N$ (ground state). Angular distributions with coefficients of $a_1=0.0$, $a_2=-0.327$ and $a_1=0.79$, $a_2=-0.22$ are compared with observed angular distribution of the γ-rays following the $^{11}B(p,\gamma)^{12}C$ (ground state).

Fig. 4.11. Differential cross section at $\theta_{lab}=60^{\circ}$ Open and closed circles are data for the γ-rays to the 0^+ and 2^+ states in ^{12}C,

respectively. The solid lines show the calculated value in Ref. TS79. The systematic error for the absolute cross-sections due to the target thickness, the efficiency of the HERMES, and the beam current integration are shown in the figure.

Fig. 4.12. The experimental a_k coefficients for the $^{11}B(p,\gamma)^{12}C$ reaction are shown. The observed differential cross sections are fitted with the function $a_0(1+a_1P_1+a_2P_2)$. TUNL, Ref. WE82.

Fig. 4.13. The experimental b_k coefficients for the $^{11}B(p,\gamma)^{12}C$ reaction are shown. The observed analyzing powers are fitted with the function $(b_1P_1^1+b_2P_2^1+b_3P_3^1)/(1+a_1P_1+a_2P_2)$. Here, a_1, a_2 are obtained from fitting the angular distribution of the γ-ray. Circle, present data for the $^{11}B(p,\gamma)^{12}C$; Triangle, present data for the $^{12}C(p,\gamma)^{13}N$; Rectangle, Ref. GL72.

Table 2.1 Performance of new data processor

Number of parameters	up to 63
Combination of events	up to 2^{15} a),b)
Gate function	Range (1-dimension) Range (2-dimension) Bit pattern matching
Preanalysis	Basic arithmetic Particle identification Multiplicity counting Function table looking
Histograming	1-dimensional histogram 2-dimensional histogram

a) The data structure table is used to define these events.
b) Rejection at MBD-11 is possible by checking the event ID word.

Table 4.1 Conditions of the measurements

E_p	Target	Beam current	Detector angle(degree)	L_{TOF}
40 MeV	^{12}C	5–10 nA	40 60 80 110 135	75 cm
40 MeV	^{11}B	5–10 nA	40 60 80 110 135	75 cm
50 MeV *	^{11}B	15–30 nA	60 135	75 cm
50 MeV	^{11}B	15–30 nA	40 60 80 110	90 cm
65 MeV	^{11}B	15–30 nA	40 60 80 110	90 cm

* This measurement was carried out at the same condition as Ep=40 MeV.

Table 4.2 Beam energy loss in the target

Target	Target angle	Thickness	E_p=40MeV	E_p=50MeV	E_p=65MeV
^{11}B	125 degree	54.1 mg/cm^2	—	564 keV	458 keV
^{11}B	120 degree	35.8 mg/cm^2	446 keV	—	—
^{12}C	120 degree	33.8 mg/cm^2	449 keV	—	—

Table 4.3 Polarization of p–^{12}C elastic scattering

E_p	Detection angle	Polarization
39.9 MeV	55 degree	0.801
49.7 MeV	50 degree	0.919
64.5 MeV	47.5 degree	0.975

Table 4.4a Differential cross section at E_p = 40 MeV

$d\sigma/d\Omega_{lab}$ nb/sr	θ_{lab}				
^{12}C state	40 degree	60 degree	80 degree	110 degree	135 degree
0^+	348.0	278.4	177.5	47.79	12.57
	16.6	15.8	7.7	2.64	1.11
2^+	450.0	373.8	291.1	133.2	73.00
	10.8	5.8	7.7	4.6	4.15
3^-	312.4	271.9	217.5	101.2	51.80
	12.9	8.7	7.5	4.6	2.64
10.0 MeV *	189.2	165.5	147.1	77.0	42.20
18.0 MeV	1.32	0.8	0.75	0.57	0.36
18.3 MeV *	430.3	380.6	343.2	185.9	105.6
19.8 MeV	4.61	2.9	2.7	2.0	1.3
20.5 MeV *	395.7	359.5	314.0	184.2	111.5
22.5 MeV	3.8	2.4	2.2	1.7	1.2
25.0 MeV *	388.3	339.7	320.4	213.2	147.0
35.0 MeV	1.7	1.06	1.0	0.8	0.6

Upper col. is the differential cross section (nb/sr).
Lower col. is its error (nb/sr).
* nb/sr per 1 MeV excitation energy region

Table 4.4b Differential cross section at E_p = 40 MeV

$d\sigma/d\Omega_{lab}$ nb/sr	θ_{lab}				
^{13}N state	40 degree	60 degree	80 degree	110 degree	135 degree
$1/2^-$	268.2	316.5	274.1	138.6	57.70
	12.7	15.6	12.2	7.3	4.14
$3/2^-$	1264.8	1403.5	1189.1	601.9	296.0
$5/2^+$	40.6	49.3	32.5	19.1	12.8

Upper col. is the differential cross section (nb/sr).
Lower col. is its error (nb/sr).

Table 4.5 Differential cross section at E_p = 50 MeV

$d\sigma/d\Omega_{lab}$ nb/sr	θ_{lab}				
^{12}C state	40 degree	60 degree	80 degree	110 degree	135 degree
0^+	185.6 17.5	167.6 14.4	95.5 8.43	21.85 2.29	4.623 0.306
2^+	218.0 6.7	221.7 7.3	154.7 7.26	69.2 5.76	32.62 1.58
3^-	184.0 11.77	178.7 11.7	137.4 7.7	67.39 6.69	26.97 1.08
10.0 MeV * 18.0 MeV	98.94 0.46	108.6 0.42	85.50 0.34	41.49 0.24	20.53 0.148
18.3 MeV * 19.8 MeV	208.3 1.55	229.1 1.39	183.27 1.133	94.138 0.822	49.215 0.530
20.5 MeV * 22.5 MeV	195.5 1.3	218.0 1.2	177.8 1.0	98.58 0.73	57.879 0.498
25.0 MeV * 35.0 MeV	217.8 0.6	250.9 0.6	222.4 0.5	146.14 0.40	98.98 0.29

Upper col. is the differential cross section (nb/sr).
Lower col. is its error (nb/sr).
* nb/sr per 1 MeV excitation energy region

Table 4.6 Differential cross section at E_p = 65 MeV

$d\sigma/d\Omega_{lab}$ nb/sr	θ_{lab}				
^{12}C state	40 degree	60 degree	80 degree	110 degree	135 degree
0^+	101.0	68.93	29.35	4.19	—
	14.7	8.6	4.60	0.83	—
2^+	116.0	100.8	58.89	22.89	—
	5.94	5.83	5.79	3.34	—
3^-	103.5	82.47	47.23	15.00	—
	13.25	7.99	7.91	2.57	—
10.0 MeV *	56.56	53.00	29.87	14.75	—
18.0 MeV	0.42	0.34	0.20	0.13	—
18.3 MeV *	108.56	107.74	60.76	31.52	—
19.8 MeV	1.34	1.13	0.66	0.43	—
20.5 MeV *	111.48	112.69	71.86	37.01	—
22.5 MeV	1.17	1.00	0.62	0.40	—
25.0 MeV *	127.26	134.37	94.06	62.17	—
35.0 MeV	0.56	0.49	0.32	0.23	—

Upper col. is the differential cross section (nb/sr).
Lower col. is its error (nb/sr).
* nb/sr per 1 MeV excitation energy region

Table 4.7a Analyzing power at E_p = 40 MeV

$A_y(\theta)$ (%)	θ_{lab}				
^{12}C state	40 degree	60 degree	80 degree	110 degree	135 degree
0^+	0.24 3.89	3.40 3.49	10.99 2.74	11.11 5.50	13.2 9.87
2^+	19.49 2.37	5.55 1.12	-4.43 2.39	-9.25 3.31	-4.43 4.26
3^-	5.69 5.33	12.21 4.15	2.15 4.39	-3.21 5.70	-14.00 6.48
10.0 MeV * 18.0 MeV	9.71 0.85	5.93 0.61	3.47 0.62	-0.47 0.88	-0.23 1.03
18.3 MeV * 19.8 MeV	1.73 1.31	2.44 0.93	5.77 0.93	8.07 1.31	11.66 1.49
20.5 MeV * 22.5 MeV	4.17 1.18	4.38 0.83	5.50 0.85	4.45 1.14	2.72 1.26
25.0 MeV * 35.0 MeV	4.03 0.53	3.96 0.38	2.63 0.38	0.94 0.47	1.51 0.49

Upper col. is the analyzing power (%).
Lower col. is its error (%).

Table 4.7b Analyzing power at E_p = 40 MeV

$A_y(\theta)$ (%)	θ_{lab}				
^{13}N state	40 degree	60 degree	80 degree	110 degree	135 degree
$1/2^-$	40.79 4.16	12.60 3.96	-4.13 3.31	-12.49 4.42	-19.62 8.20
$3/2^-$ $5/2^+$	0.39 2.95	4.30 2.06	8.63 2.14	13.59 3.01	8.19 5.14

Upper col. is the analyzing power (%).
Lower col. is its error (%).

Table 4.8 Analyzing power at E_p = 50 MeV

$A_y(0)$ (%)	θ_{lab}				
^{12}C state	40 degree	60 degree	80 degree	110 degree	135 degree
0^+	1.44 1.55	4.91 1.51	4.75 1.69	14.71 4.04	17.26 6.36
2^+	19.86 2.69	0.36 1.66	-3.81 1.70	-9.34 2.86	-8.40 2.87
3^-	11.27 3.21	4.37 2.71	-1.48 2.43	-1.01 3.61	-12.79 4.71
10.0 MeV * 18.0 MeV	11.06 0.62	5.87 0.51	1.87 0.53	-2.27 0.80	-2.92 0.89
18.3 MeV * 19.8 MeV	3.97 1.00	4.12 0.81	5.70 0.84	7.51 1.22	4.63 1.32
20.5 MeV * 22.5 MeV	7.04 0.89	6.48 0.72	4.21 0.74	3.24 1.03	3.32 1.06
25.0 MeV * 35.0 MeV	7.03 0.38	4.61 0.30	3.10 0.29	3.20 0.38	1.58 0.36

Upper col. is the analyzing power (%).
Lower col. is its error (%).

Table 4.9 Analyzing power at E_p = 65 MeV

$A_y(\theta)$ (%)	θ_{lab}				
^{12}C state	40 degree	60 degree	80 degree	110 degree	135 degree
0^+	7.30 2.66	4.44 2.65	-1.08 3.16	9.41 8.18	— —
2^+	9.60 4.47	1.65 3.05	-0.05 3.05	0.62 4.00	— —
3^-	1.33 9.36	-4.15 6.50	-3.45 8.05	-10.95 10.41	— —
10.0 MeV * 18.0 MeV	9.90 0.91	4.42 0.80	1.82 0.84	-3.78 1.09	— —
18.3 MeV * 19.8 MeV	6.99 1.52	7.30 1.30	2.20 1.37	1.71 1.73	— —
20.5 MeV * 22.5 MeV	7.18 1.30	4.90 1.10	4.76 1.09	1.00 1.38	— —
25.0 MeV * 35.0 MeV	8.95 0.54	5.84 0.45	3.27 0.43	1.54 0.48	— —

Upper col. is the analyzing power (%).
Lower col. is its error (%).

Table 4.10 ^{12}C 1p–1h excited states

J^p T	j_p	(e,e')[1]	(^{3}He,d)[2]	(p,p')[3]
1^- 1	$s_{1/2}$	18.1 MeV		
4^- 0	$d_{5/2}$		18.27 MeV	
3^- 1	$d_{5/2}$	18.6 MeV	18.36 MeV	
2^- 1	$d_{5/2}$	19.3 MeV	19.2 MeV	
4^- 1	$d_{5/2}$	19.6 MeV		
3^- 1	$d_{3/2}$			20.57 MeV
3^- 0	$d_{3/2}$		20.6 MeV	21.65 MeV
1^- 1	$d_{5/2}$	22.0 MeV		
1^- 1	$d_{5/2}$		22.4 MeV	
1^- 1	$d_{3/2}$	22.7 MeV		

1) Ref. YA71 A. Yamaguchi et al, Phys. Rev. C3, 1750 (1970).
2) Ref. RE71 G.M. Reynolds et al, Phys. Rev. C3, 442 (1970).
3) Ref. BU77 M. Buenerd et al, Nucl. Phys. A289, 377 (1977).

Table 4.11a Legendre expansion coefficients a_k

a_k		$E_{p\ lab}$		
^{12}C		40 MeV	50 MeV	65 MeV
0^+	a_1	1.39 + − 0.08	1.53 + − 0.12	1.61 + − 0.26
	a_2	0.30 + − 0.10	0.57 + − 0.08	1.00 + − 0.43
2^+	a_1	1.02 + − 0.02	0.98 + − 0.03	1.51 + − 0.18
	a_2	0.13 + − 0.04	−0.12 + − 0.06	0.03 + − 0.24
3^-	a_1	1.00 + − 0.04	0.97 + − 0.08	1.57 + − 0.27
	a_2	0.04 + − 0.05	−0.15 + − 0.08	0.27 + − 0.46
10 MeV : 18 MeV	a_1	0.84 + − 0.01	0.88 + − 0.00	1.16 + − 0.01
	a_2	−0.11 + − 0.01	−0.20 + − 0.01	0.23 + − 0.02
18.3 MeV : 19.8 MeV	a_1	0.79 + − 0.01	0.82 + − 0.01	1.13 + − 0.02
	a_2	−0.13 + − 0.01	−0.23 + − 0.01	0.15 + − 0.03
20.5 MeV : 22.5 MeV	a_1	0.73 + − 0.01	0.73 + − 0.01	1.15 + − 0.02
	a_2	−0.12 + − 0.01	−0.23 + − 0.01	−0.10 + − 0.03
25 MeV : 35 MeV	a_1	0.55 + − 0.00	0.49 + − 0.00	0.77 + − 0.01
	a_2	−0.13 + − 0.01	−0.31 + − 0.00	−0.12 + − 0.01

Table 4.11b Legendre expansion coefficients a_k

a_k		$E_{p\ lab}$		
^{13}N		40 MeV	50 MeV	65 MeV
$1/2^-$	a_1	0.87 + − 0.04	—	—
	a_2	−0.30 + − 0.06	—	—
$3/2^-$ and $5/2^+$	a_1	0.82 + − 0.03	—	—
	a_2	−0.27 + − 0.04	—	—

Table 4.12a Legendre expansion coefficients b_k

b_k (%) ^{12}C		$E_{p\ lab}$ 40 MeV	50 MeV	65 MeV
0^+	b_1	6.88 +- 1.91	5.14 +- 1.03	5.84 +- 2.01
	b_2	1.68 +- 1.58	1.33 +- 0.77	1.84 +- 1.29
2^+	b_1	1.03 +- 1.09	-0.33 +- 1.15	4.52 +- 2.54
	b_2	6.61 +- 0.77	5.70 +- 0.95	1.76 +- 1.82
3^-	b_1	4.93 +- 2.63	2.14 +- 1.65	-4.22 +- 5.35
	b_2	6.42 +- 1.99	4.85 +- 1.28	-0.36 +- 3.99
10 MeV : 18 MeV	b_1	4.71 +- 0.40	4.14 +- 0.35	4.53 +- 0.58
	b_2	4.15 +- 0.30	5.04 +- 0.24	4.28 +- 0.47
18.3 MeV : 19.8 MeV	b_1	5.92 +- 0.60	6.30 +- 0.55	6.00 +- 0.95
	b_2	-0.66 +- 0.45	1.22 +- 0.38	3.20 +- 0.79
20.5 MeV : 22.5 MeV	b_1	5.35 +- 0.53	5.95 +- 0.48	5.45 +- 0.82
	b_2	1.54 +- 0.40	2.86 +- 0.33	3.72 +- 0.69
25 MeV : 35 MeV	b_1	3.14 +- 0.23	4.57 +- 0.19	5.78 +- 0.32
	b_2	1.65 +- 0.17	2.12 +- 0.13	2.97 +- 0.28

Table 4.12b Legendre expansion coefficients b_k

b_k (%) ^{13}N		$E_{p\ lab}$ 40 MeV	50 MeV	65 MeV
$1/2^-$	b_1	6.61 +- 2.38	—	—
	b_2	16.27 +- 1.79	—	—
$3/2^-$ and $5/2^+$	b_1	8.87 +- 2.04	—	—
	b_2	-0.49 +- 1.43	—	—

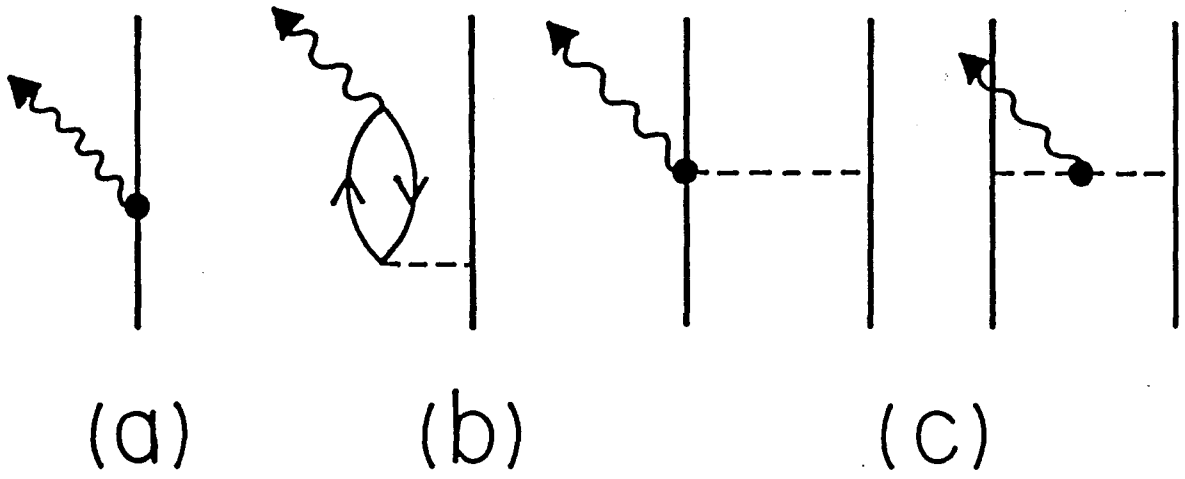
(a)
(b)
(c)

FIG. 1.1

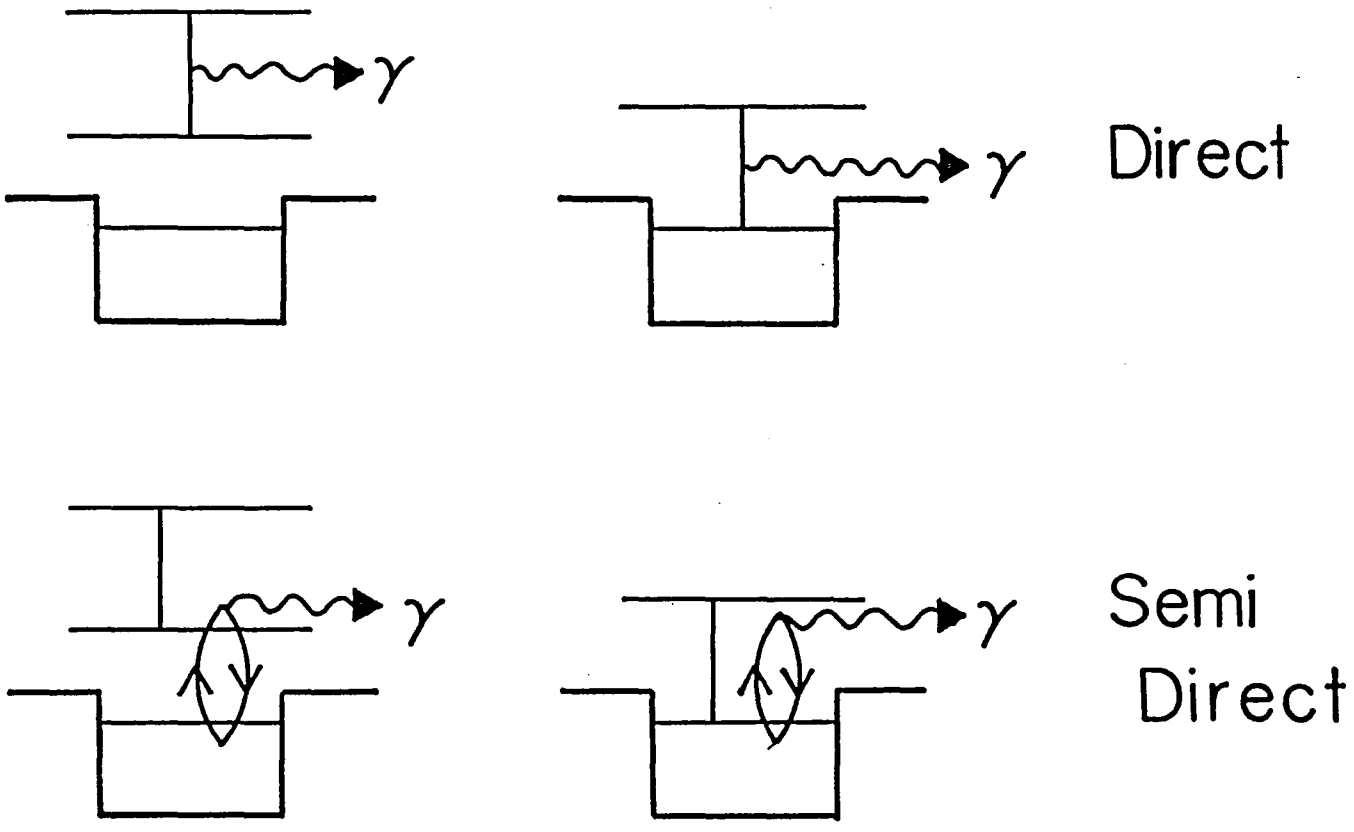
γ
γ
Direct
γ
γ
Semi
Direct
Medium Energy Proton
Radiative Capture
Low Energy Proton
Radiative Capture

FIG. 1.2

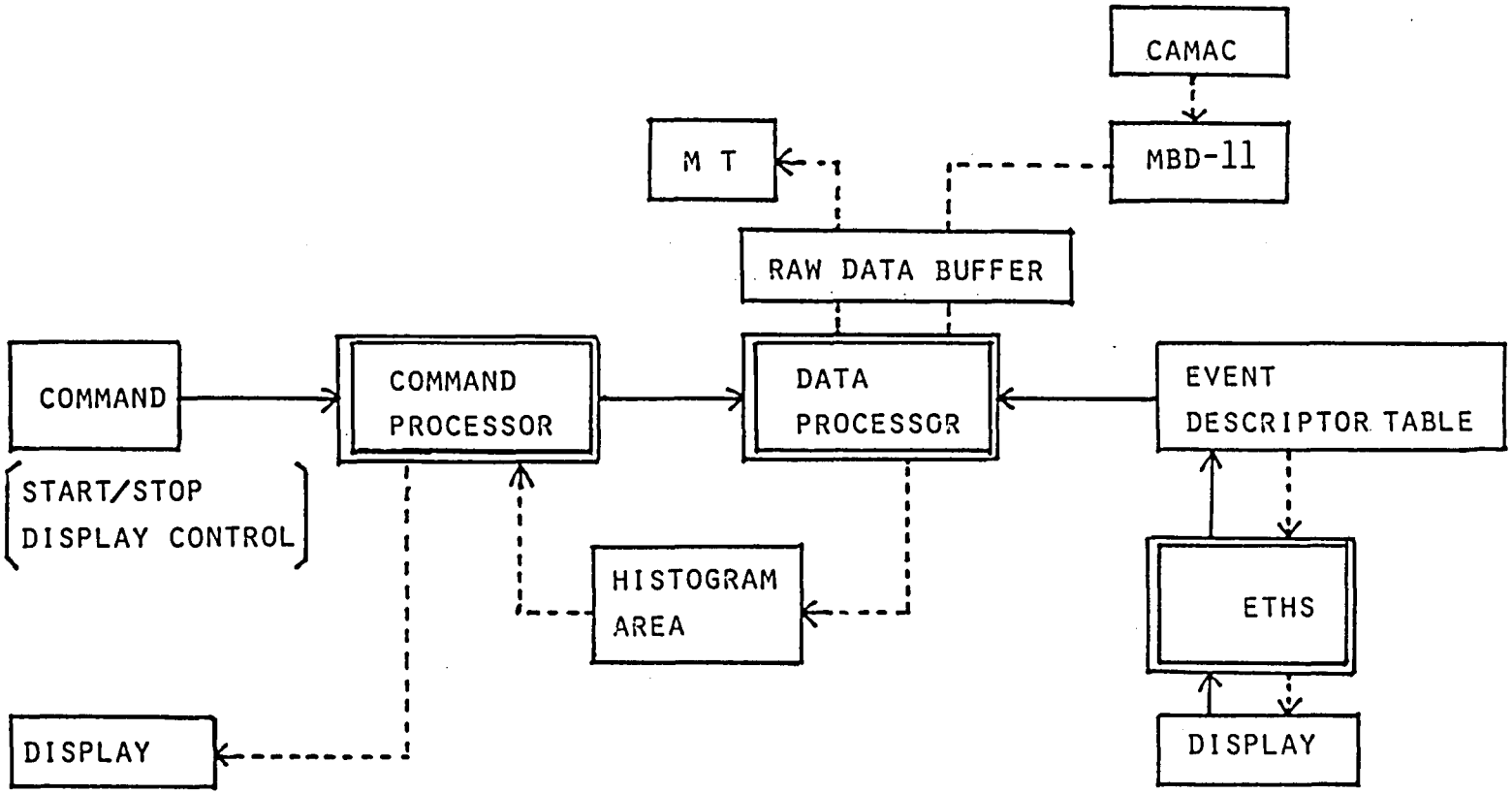

... PROCESSOR;TASKS FOR SPECIFIED FUNCTIONS.

... DATA STORAGE REGION OR PERIPHERAL DEVICES.

... RELATION OF CONTROLS.

... DATA FLOW.

Fig. 2.1

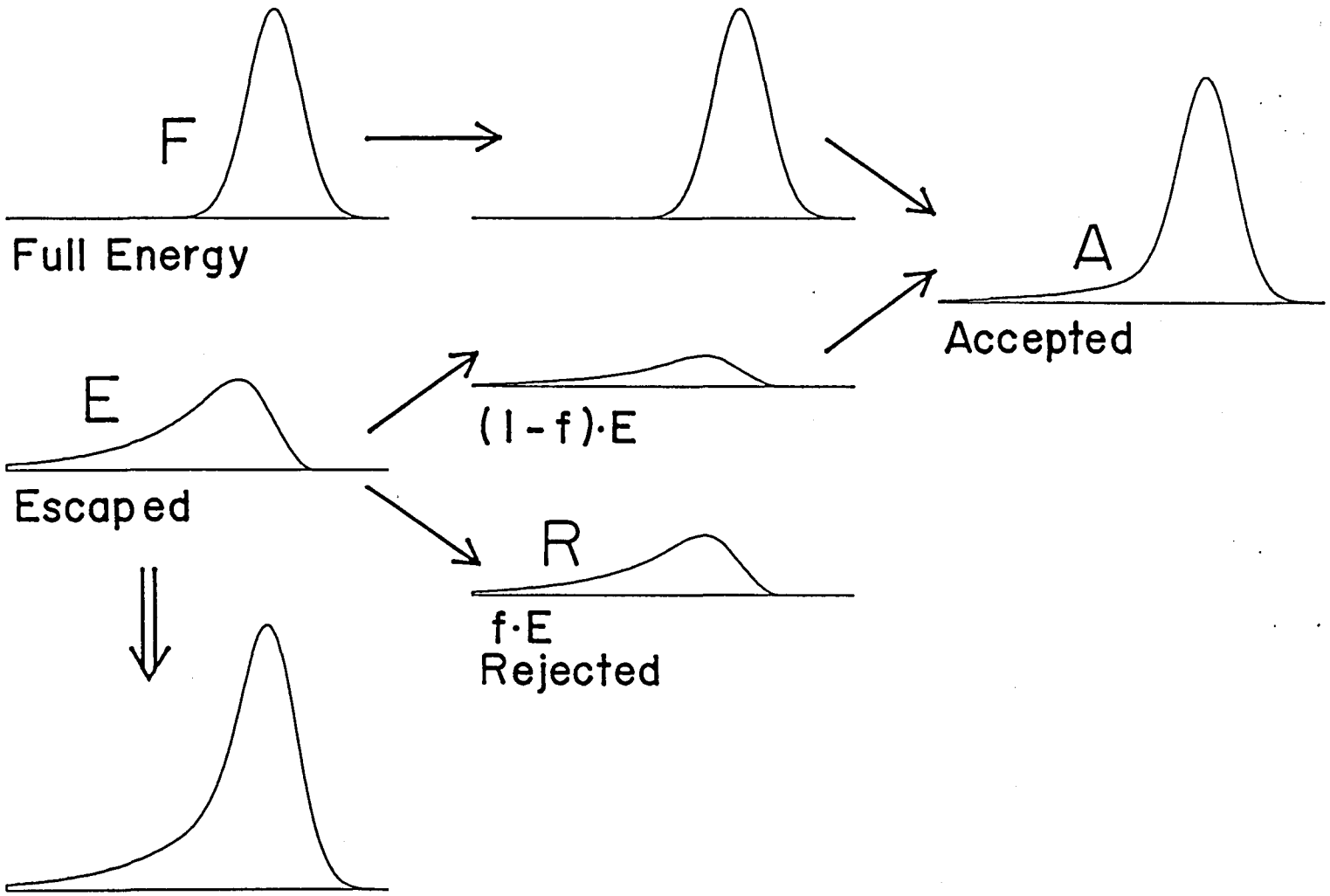
F
Full Energy
A
Accepted
E
Escaped
(1-f)·E
R
f·E
Rejected
Total (Spectrum Obtained From The NaI Signals)

Fig. 3.1

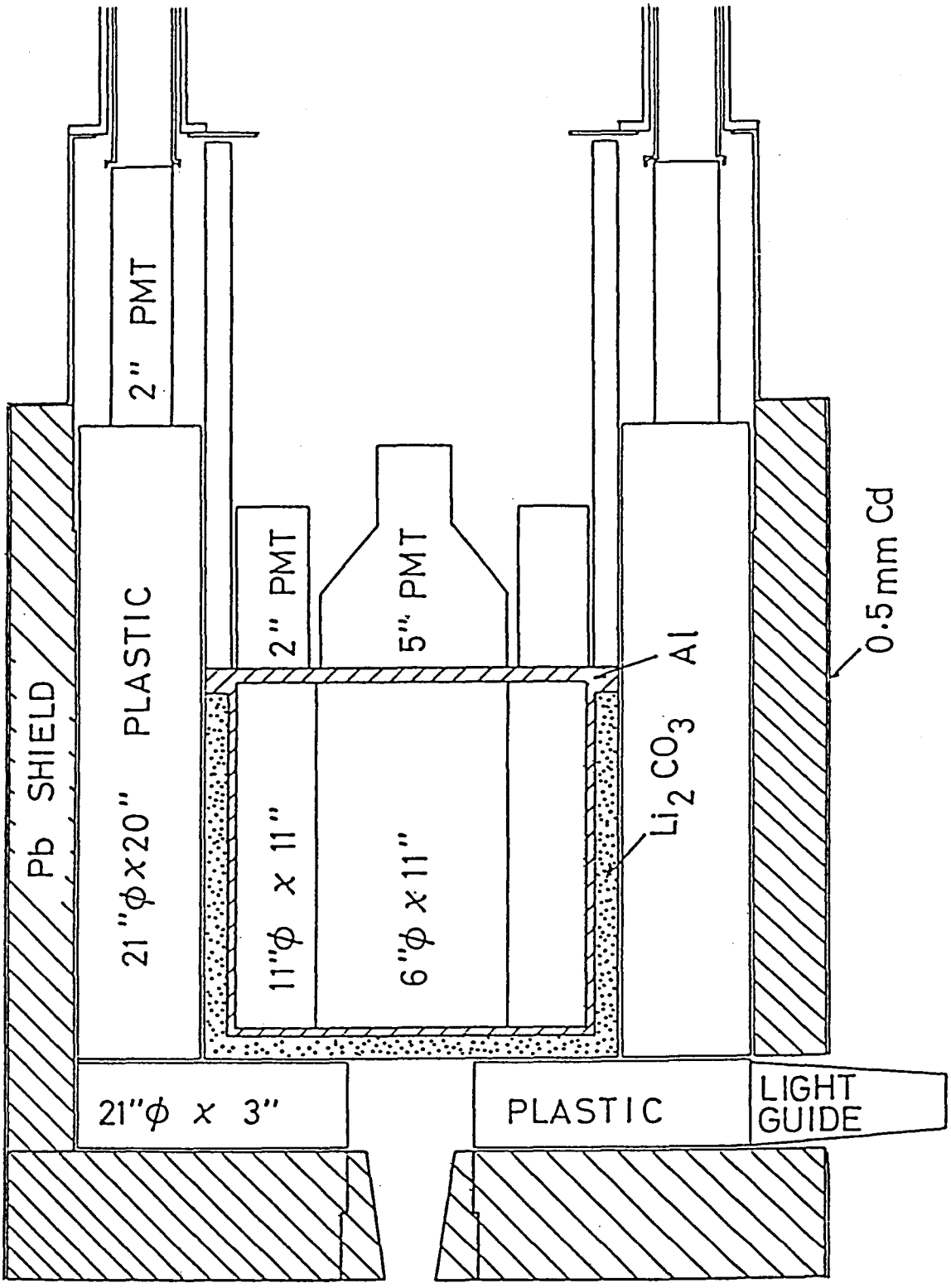
2" PMT
Pb SHIELD
21"φx20" PLASTIC
2" PMT
5" PMT
11"φ x 11"
6"φ x 11"
Al
Li_2CO_3
0.5mm Cd
21"φ x 3"
PLASTIC
LIGHT GUIDE

FIG. 3.2

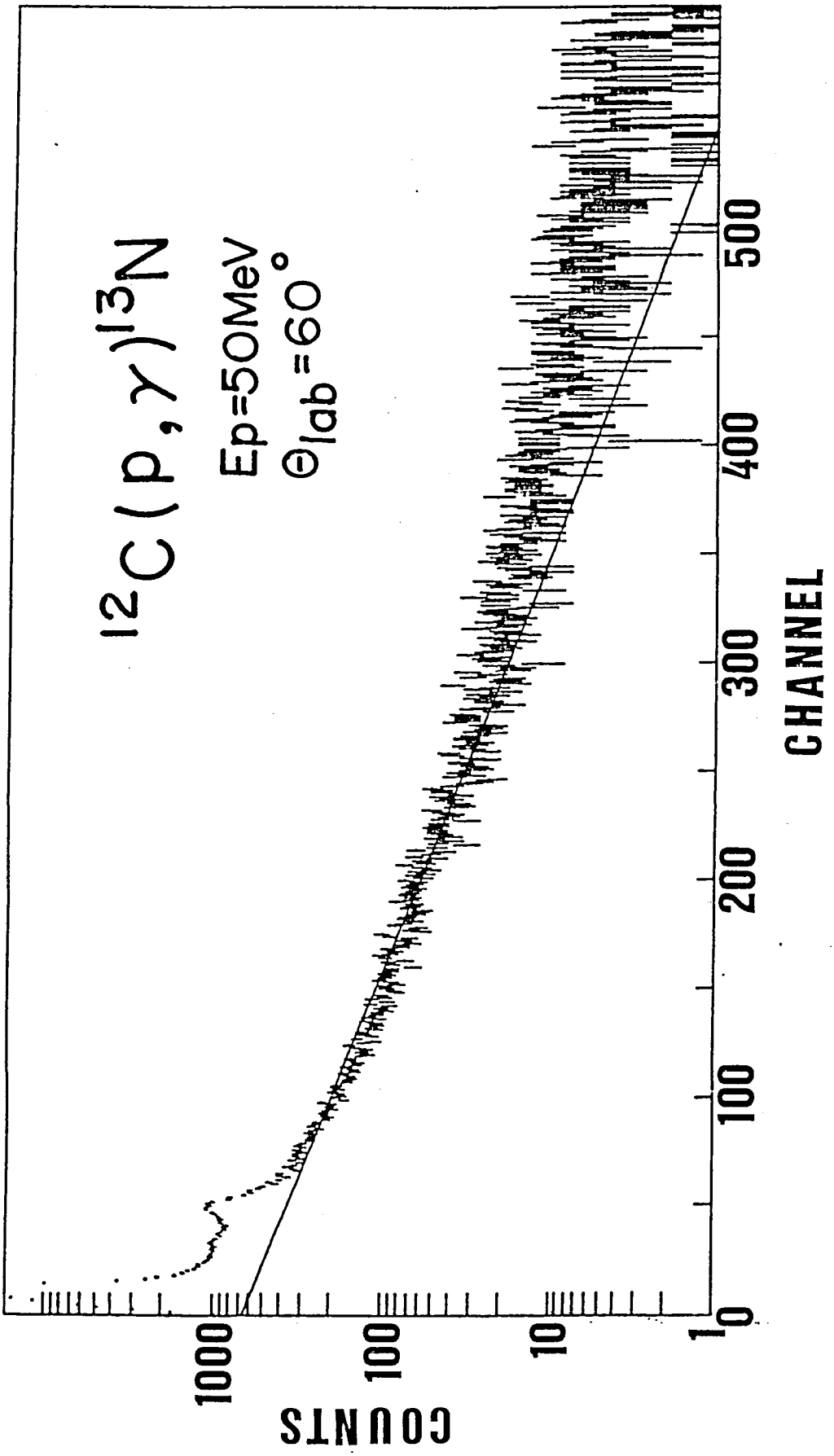
$^{12}C(p,\gamma)^{13}N$
Ep=50MeV
$\Theta_{lab}=60°$
COUNTS
1000
100
10
1
0
100
200
300
400
500
CHANNEL

FIG. 3.3

Small Volume NaI Crystal

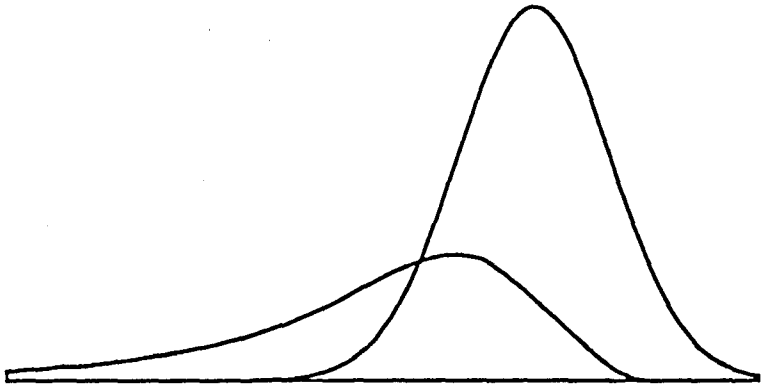

Previous Large Volume NaI Crystal

HERMES

Fig. 3.4

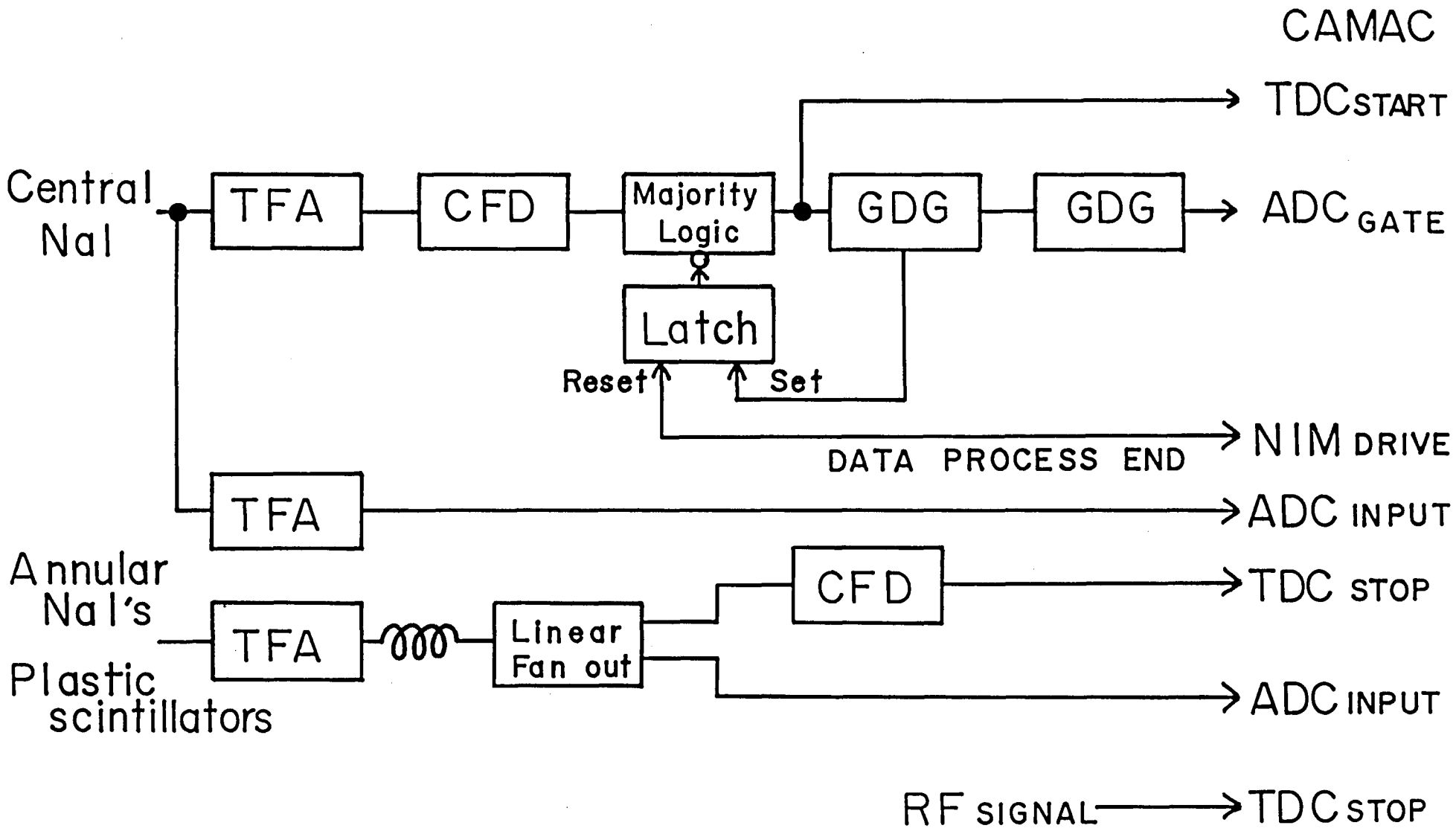
CAMAC
TDC START
Central
NaI
TFA
CFD
Majority
Logic
GDG
GDG
ADC GATE
Latch
Reset
Set
DATA PROCESS END
NIM DRIVE
TFA
ADC INPUT
Annular
NaI's
Plastic
scintillators
TFA
Linear
Fan out
CFD
TDC STOP
ADC INPUT
RF SIGNAL
TDC STOP

FIG. 3.5

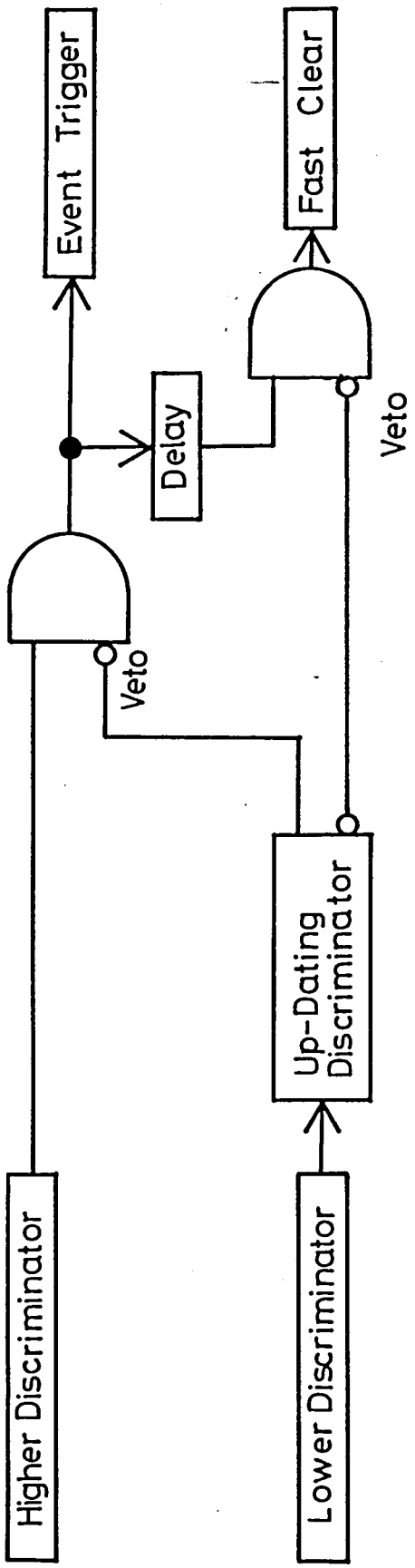
Event Trigger
Fast Clear
Delay
Veto
Veto
Up-Dating Discriminator
Higher Discriminator
Lower Discriminator

FIG. 3.6

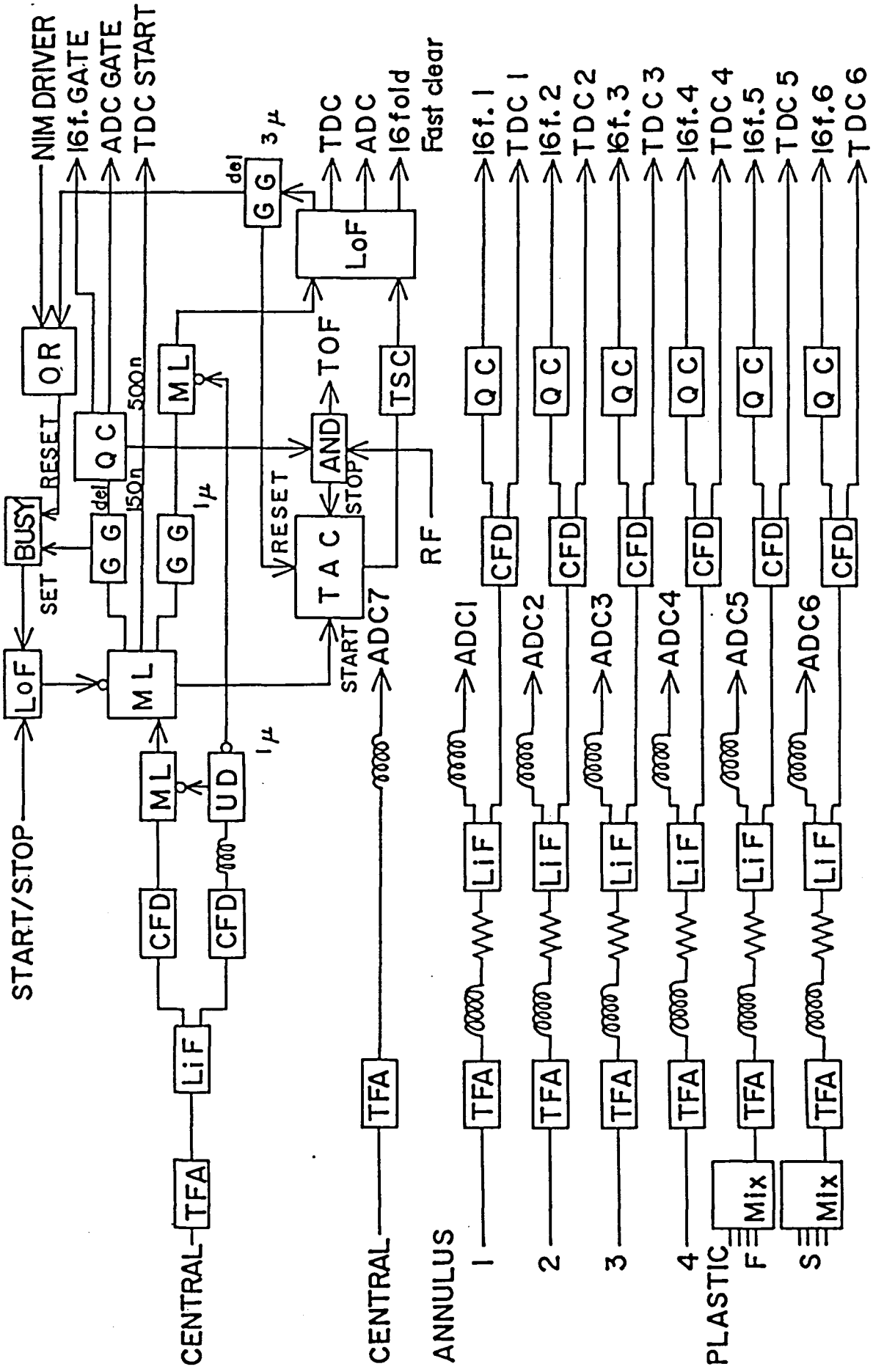
NIM DRIVER
16f. GATE
ADC GATE
TDC START
OR
BUSY
RESET
SET
Q C
500n
150n
del
G G
M L
1μ
3μ
LoF
TOF
AND
STOP
T A C
START
RESET
TSC
RF
TDC
ADC
16fold
Fast clear
START/STOP
CFD
LiF
TFA
UD
CENTRAL
ADC7
ADC1
ADC2
ADC3
ADC4
ADC5
ADC6
16f. 1
TDC 1
16f. 2
TDC2
16f. 3
TDC 3
16f. 4
TDC 4
16f. 5
TDC 5
16f. 6
TDC 6
ANNULUS
1
2
3
4
PLASTIC
F
S
Mix

FIG. 3.7

```
      PROGRAM HERANA
C
      CHARACTER COM*80,TAG*6,FNAME*9
      INTEGER*2 A1,A2,A3,A4,PF,PS,CENT,T1,T2,T3,T4,TPF,TPS,TOF
      INTEGER*2 T1S,T2S,T3S,T4S,TPFS,TPSS,A1MAX,A2MAX,A3MAX,A4MAX
      INTEGER*2 T1E,T2F,T3E,T4E,TPFE,TPSF,PFDIS,PSDIS,TOFS,TOFF
      INTEGER*2 IDX(16),TAGSIZ
      LOGICAL*1 UP,DOWN
      INTEGER*4 UPHST(0:1023),DNHST(0:1023),UPAHST(0:1023),DNAHST(0:1023)
      INTEGER*4 COUNT
C
      COMMON /COMENT/ COM
      COMMON /EVENT/ IBLOCK,ID,A1,A2,A3,A4,PF,PS,CENT,T1,T2,T3,T4,TPF,TPS,TOF
      COMMON /PARAM/ T1S,T1E,T2S,T2E,T3S,T3E,T4S,T4F,TPFS,TPFE,TPSS,TPSE,
     1               TOFS,TOFE,A1MAX,A2MAX,A3MAX,A4MAX,PFDIS,PSDIS,
     2               FA1,BA1,FA2,BA2,FA3,BA3,FA4,BA4
      COMMON /HISNAM/ TAG,TAGSIZ
C
      CALL MTRINI
      CALL GETID (IDX)
      IDPTR=1
      IF (IDX(IDPTR).EQ.0) STOP
2000  CALL GETPRM(IDX(IDPTR))
      IDPTR=IDPTR+1
      COUNT=0
      DO 200 I=0,1023
        UPHST(I)=0
        DNHST(I)=0
        UPAHST(I)=0
        DNAHST(I)=0
 200  CONTINUE
1000  CALL EVREAD(IFLAG)
      IF (IFLAG.LT.0) GOTO 500
      COUNT=COUNT+1
      IF (TOF.GT.TOFE .OR. TOF.LT.TOFS) GOTO 1000
      IF (A1.GT.A1MAX) GOTO 1000
      IF (A2.GT.A2MAX) GOTO 1000
      IF (A3.GT.A3MAX) GOTO 1000
      IF (A4.GT.A4MAX) GOTO 1000
      ANULUS=0.0
      IF (T1.GE.T1S .AND. T1.LE.T1E) ANULUS=ANULUS+FLOAT(A1)*FA1+BA1
      IF (T2.GE.T2S .AND. T2.LE.T2E) ANULUS=ANULUS+FLOAT(A2)*FA2+BA2
      IF (T3.GE.T3S .AND. T3.LE.T3E) ANULUS=ANULUS+FLOAT(A3)*FA3+BA3
      IF (T4.GE.T4S .AND. T4.LE.T4E) ANULUS=ANULUS+FLOAT(A4)*FA4+BA4
      II=CENT+ANULUS
      IF (II.GT.1023) GOTO 1000
      UP=ID.EQ.-16
      DOWN=ID.EQ.-15
      IF (UP)   UPHST(II)=UPHST(II)+1
      IF (DOWN) DNHST(II)=DNHST(II)+1
      IF ( TPS.GE.TPSS .AND. TPS.LT.TPSE .AND. PS.GE.PSDIS ) GOTO 1000
      IF ( TPF.GE.TPFS .AND. TPF.LT.TPFE .AND. PF.GE.PFDIS ) GOTO 1000
      IF (UP)   UPAHST(II)=UPAHST(II)+1
      IF (DOWN) DNAHST(II)=DNAHST(II)+1
      GOTO 1000
C
500   IF (IFLAG.EQ.-1) THEN
        WRITE (6,'('' MT READ ERROR AT BLOCK '',I5)') IBLOCK
        GOTO 1000
      END IF
      WRITE (6,'('' TOTAL COUNT ='',I9)') COUNT
      FNAME(1:TAGSIZ)=TAG



      FNAME(TAGSIZ+1:TAGSIZ+3)='UPA'
      CALL HISOUT (FNAME,TAGSIZ+2,UPHST,1024)
      CALL HISOUT (FNAME,TAGSIZ+3,UPAHST,1024)
      FNAME(TAGSIZ+1:TAGSIZ+3)='DNA'
      CALL HISOUT (FNAME,TAGSIZ+2,DNHST,1024)
      CALL HISOUT (FNAME,TAGSIZ+3,DNAHST,1024)
      IF (IFLAG.EQ.-4 .OR. IFLAG.EQ.-5) WRITE (6,'(1H ,A80)') COM
      IF (IFLAG.EQ.-2 .OR. IFLAG.EQ.-4) GOTO 2000
      STOP
      END
```

FIG. 3.8

```
xxxxx B50H40UPA xxxxx  Fitted from  375 ch to  465 ch  << HERFIT >>
     13  CHI=   99.47288
Ex   =     0.0000000        4.440000        7.650000        9.640000
Int  =     186.2785        266.3544        34.12064        215.5122
Error=     4.018353        5.642444        5.670315        5.755863
Sum  =     5129.534        7118.235        391.5172        5550.309
Prm  =     448.6142        6.904742        5.683361        0.9075806       0.7700000       2.100000
Error=     0.2789363       0.3362297E-01   0.2306865       0.2661803E-01
```

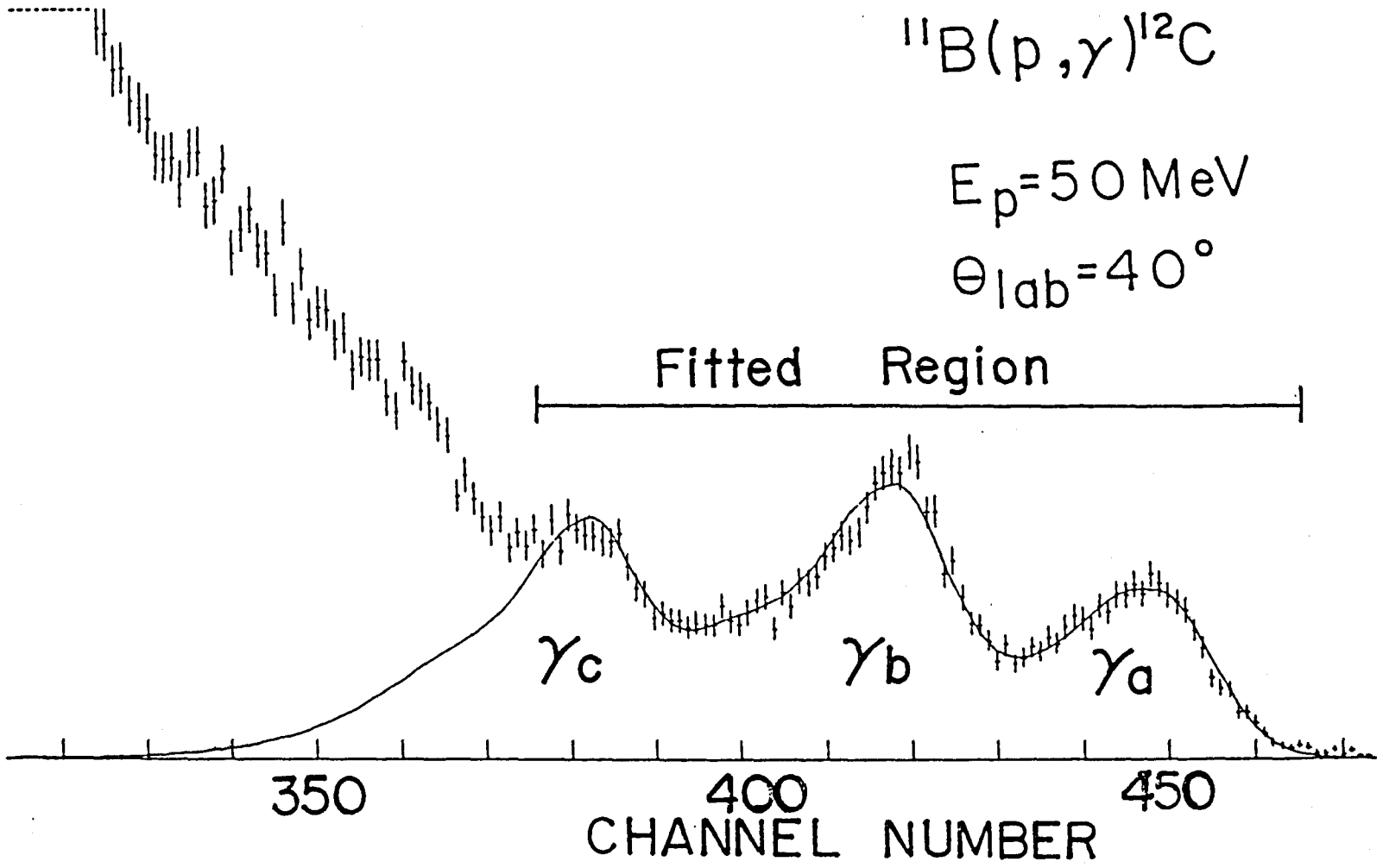

FIG. 3.9

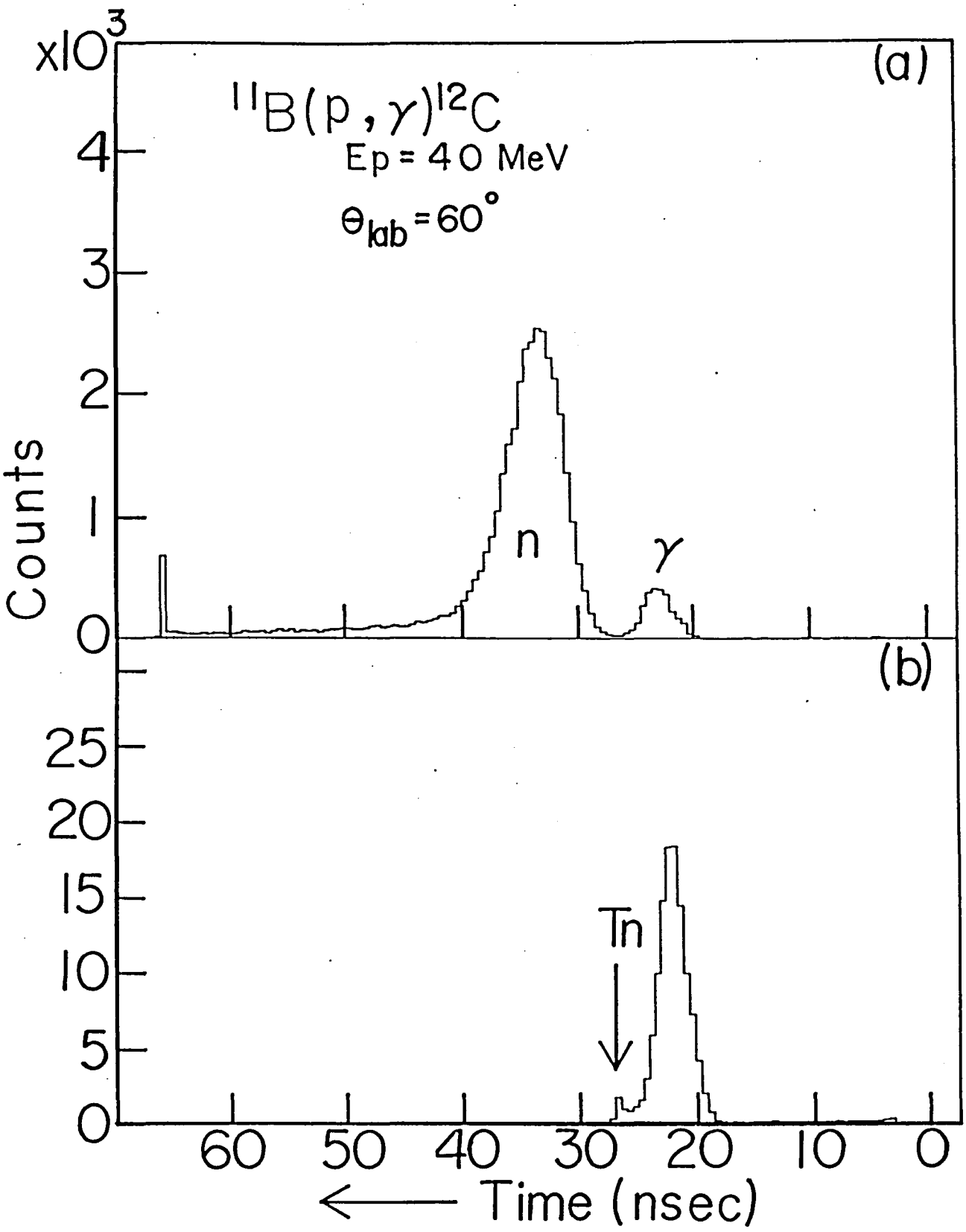
x10^3
(a)
11B(p,γ)12C
Ep = 40 MeV
θlab = 60°
4
3
2
1
0
Counts
n
γ
(b)
25
20
15
10
5
0
Tn
60
50
40
30
20
10
0
← Time (nsec)

FIG. 4.1

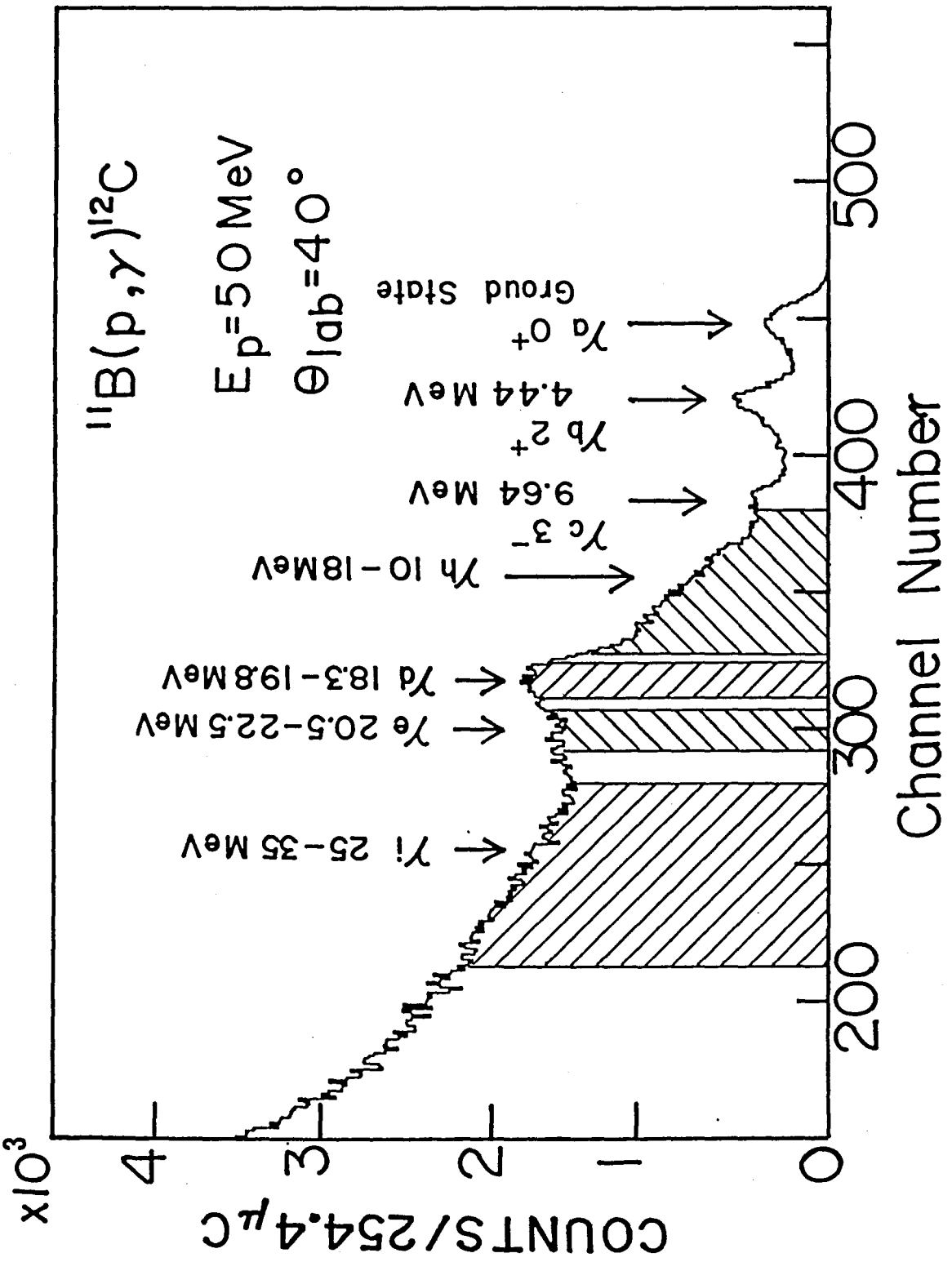
$^{11}B(p,\gamma)^{12}C$
E_p=50 MeV
Θ_{lab}=40°
Ground State
γ_a 0+
4.44 MeV
γ_b 2+
9.64 MeV
γ_c 3−
γ_h 10−18MeV
γ_d 18.3−19.8MeV
γ_e 20.5−22.5 MeV
γ_i 25−35 MeV
COUNTS/254.4 μC
x10³
0
1
2
3
4
200
300
400
500
Channel Number

FIG. 4.2

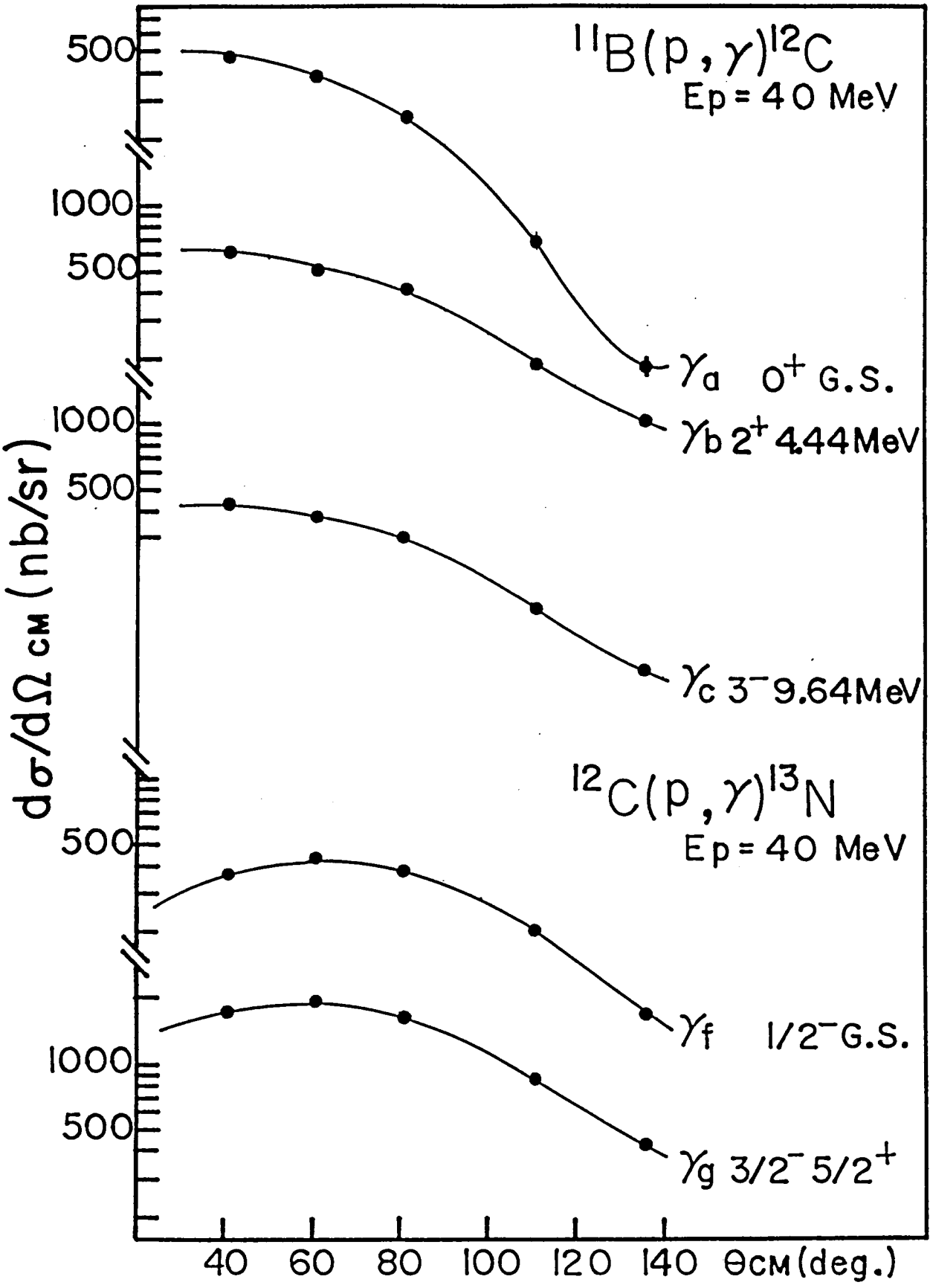
$^{11}B(p,\gamma)^{12}C$
Ep = 40 MeV
γ_a 0^+ G.S.
γ_b 2^+ 4.44MeV
γ_c 3^- 9.64MeV
$^{12}C(p,\gamma)^{13}N$
Ep = 40 MeV
γ_f $1/2^-$ G.S.
γ_g $3/2^-$ $5/2^+$
$d\sigma/d\Omega$ cm (nb/sr)
500
1000
500
1000
500
500
1000
500
40 60 80 100 120 140 θcm(deg.)

FIG 4.3A

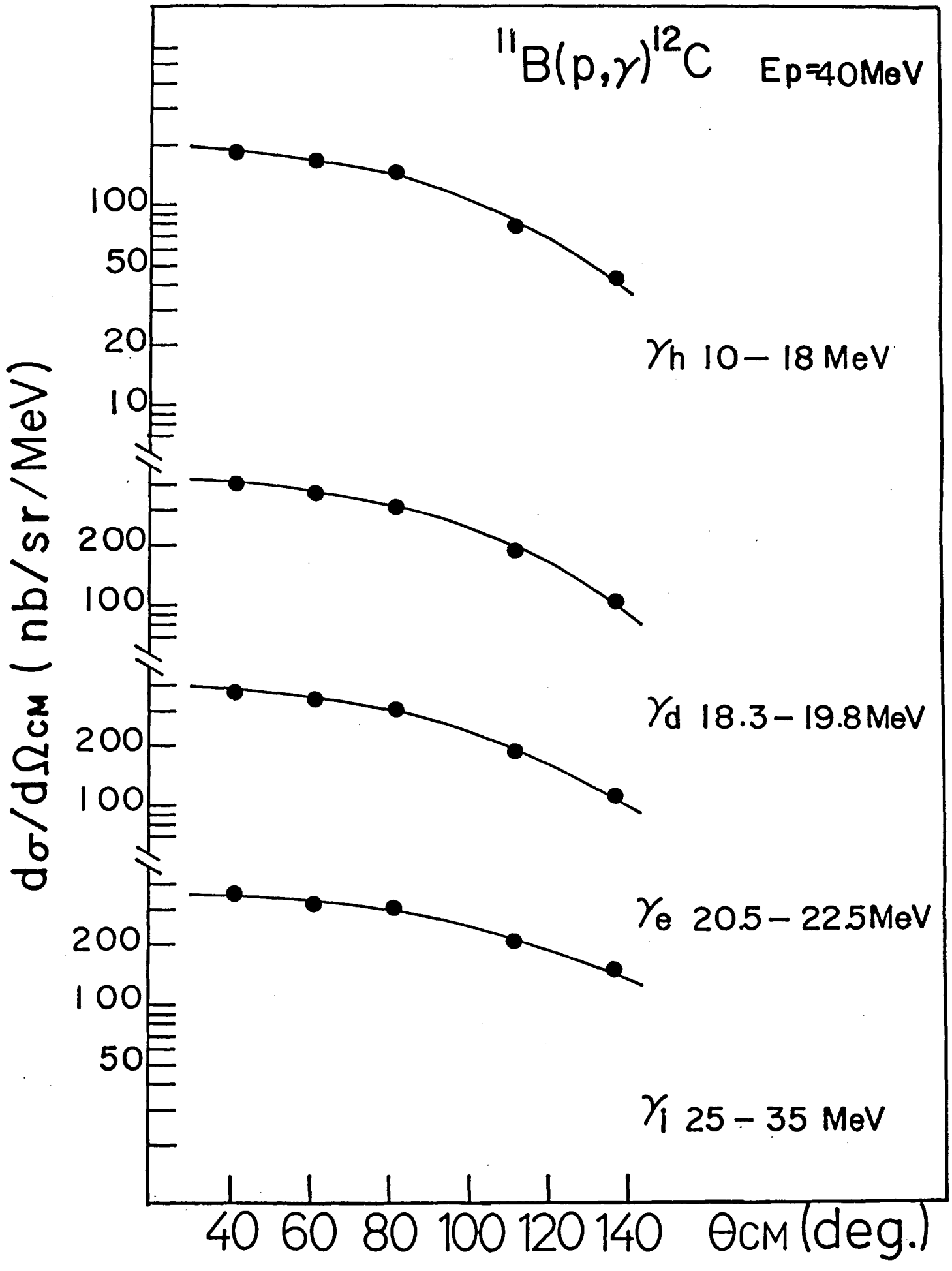
$^{11}B(p,\gamma)^{12}C$ Ep=40MeV
γ_h 10 – 18 MeV
γ_d 18.3 – 19.8MeV
γ_e 20.5 – 22.5MeV
γ_i 25 – 35 MeV
dσ/dΩcm (nb/sr/MeV)
100
50
20
10
200
100
200
100
200
100
50
40 60 80 100 120 140 θcm (deg.)

FIG. 4.3B

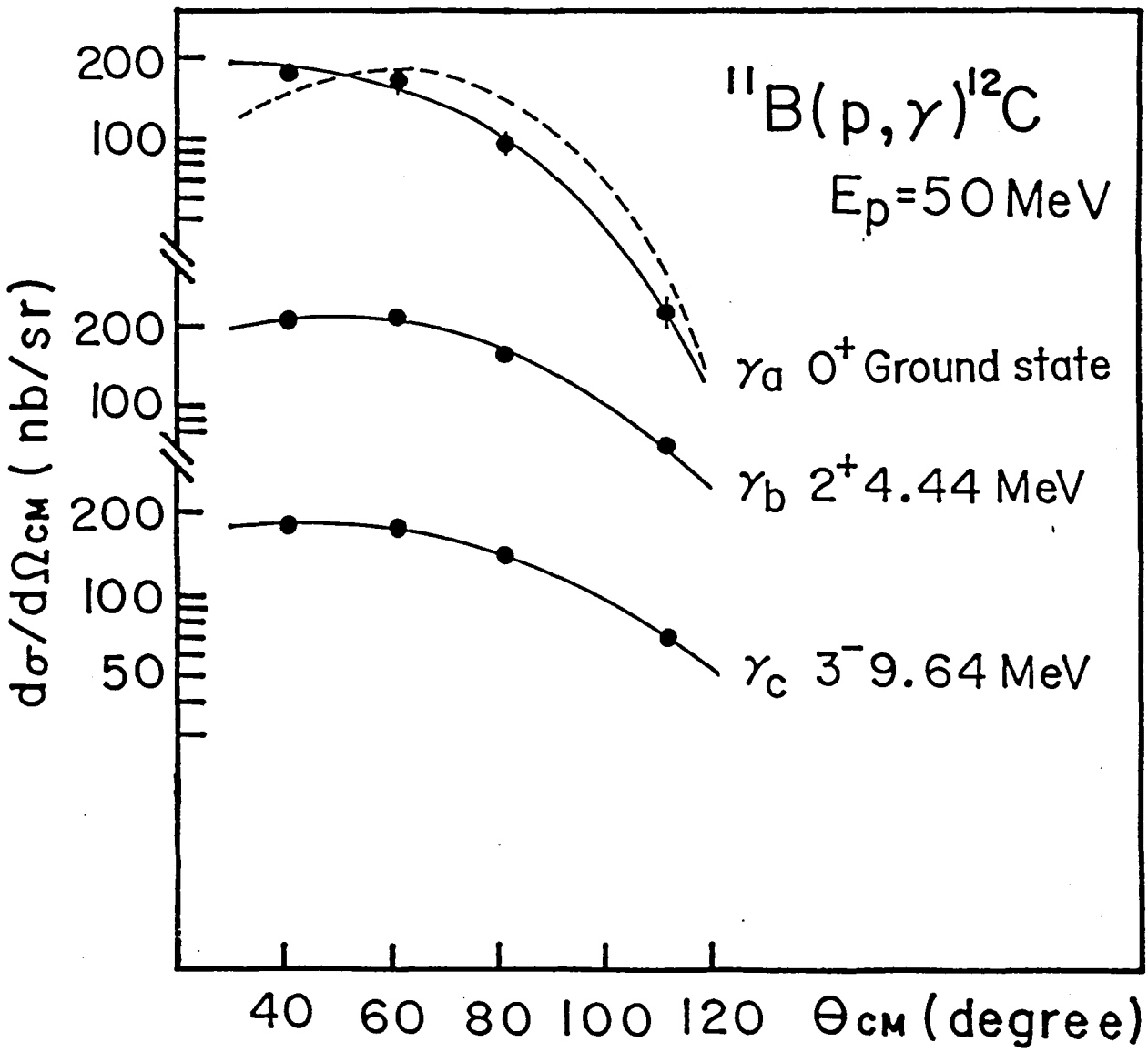
$^{11}B(p,\gamma)^{12}C$
E_p=50 MeV
γ_a 0^+ Ground state
γ_b 2^+ 4.44 MeV
γ_c 3^- 9.64 MeV
200
100
200
100
200
100
50
$d\sigma/d\Omega_{CM}$ (nb/sr)
40 60 80 100 120 Θ_{CM} (degree)

FIG. 4.4A

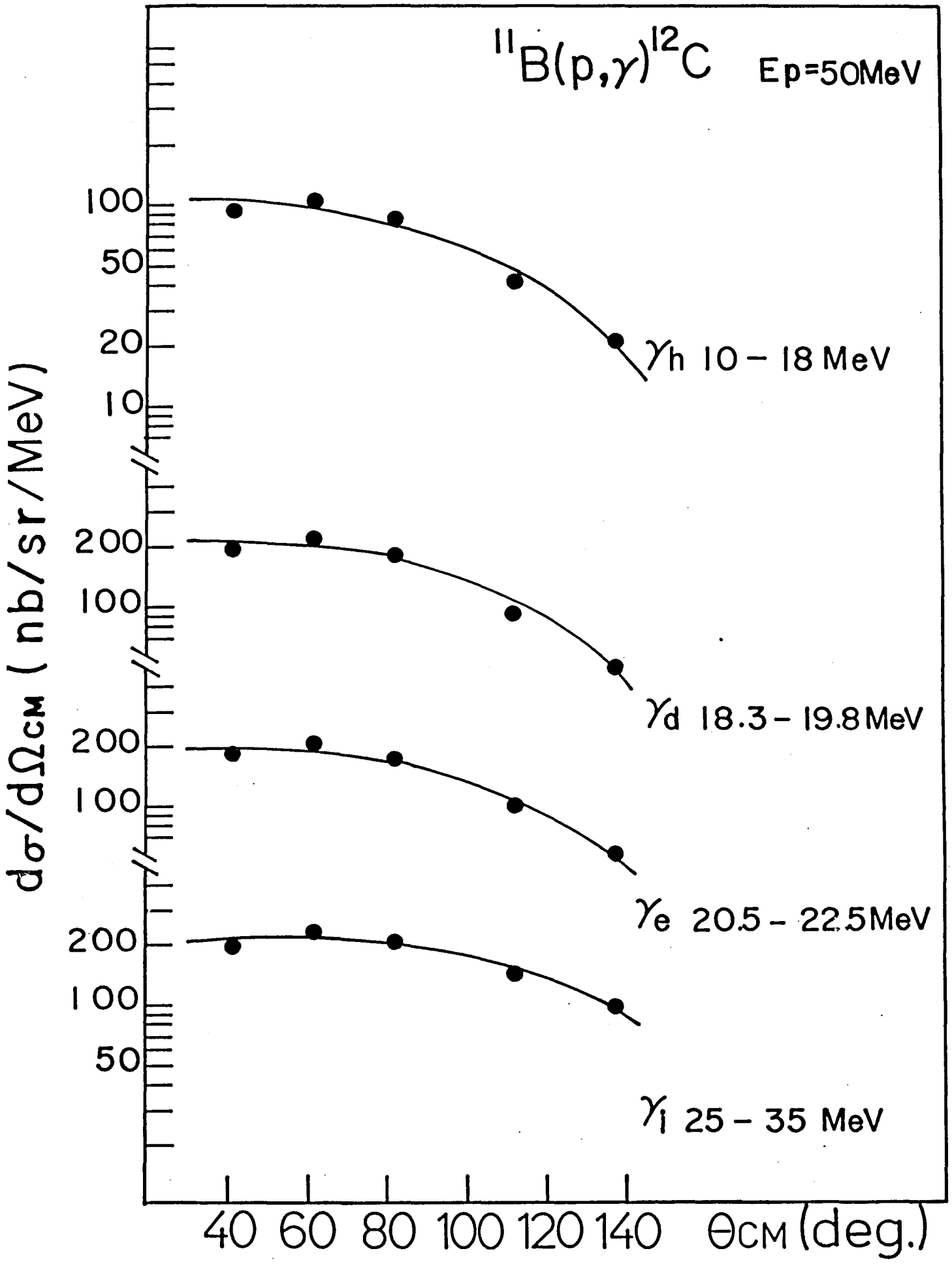
$^{11}B(p,\gamma)^{12}C$ Ep=50MeV
100
50
20
10
200
100
200
100
200
100
50
γ_h 10 – 18 MeV
γ_d 18.3 – 19.8MeV
γ_e 20.5 – 22.5MeV
γ_i 25 – 35 MeV
$d\sigma/d\Omega_{CM}$ (nb/sr/MeV)
40 60 80 100 120 140 θ_{CM} (deg.)

FIG. 4.4B

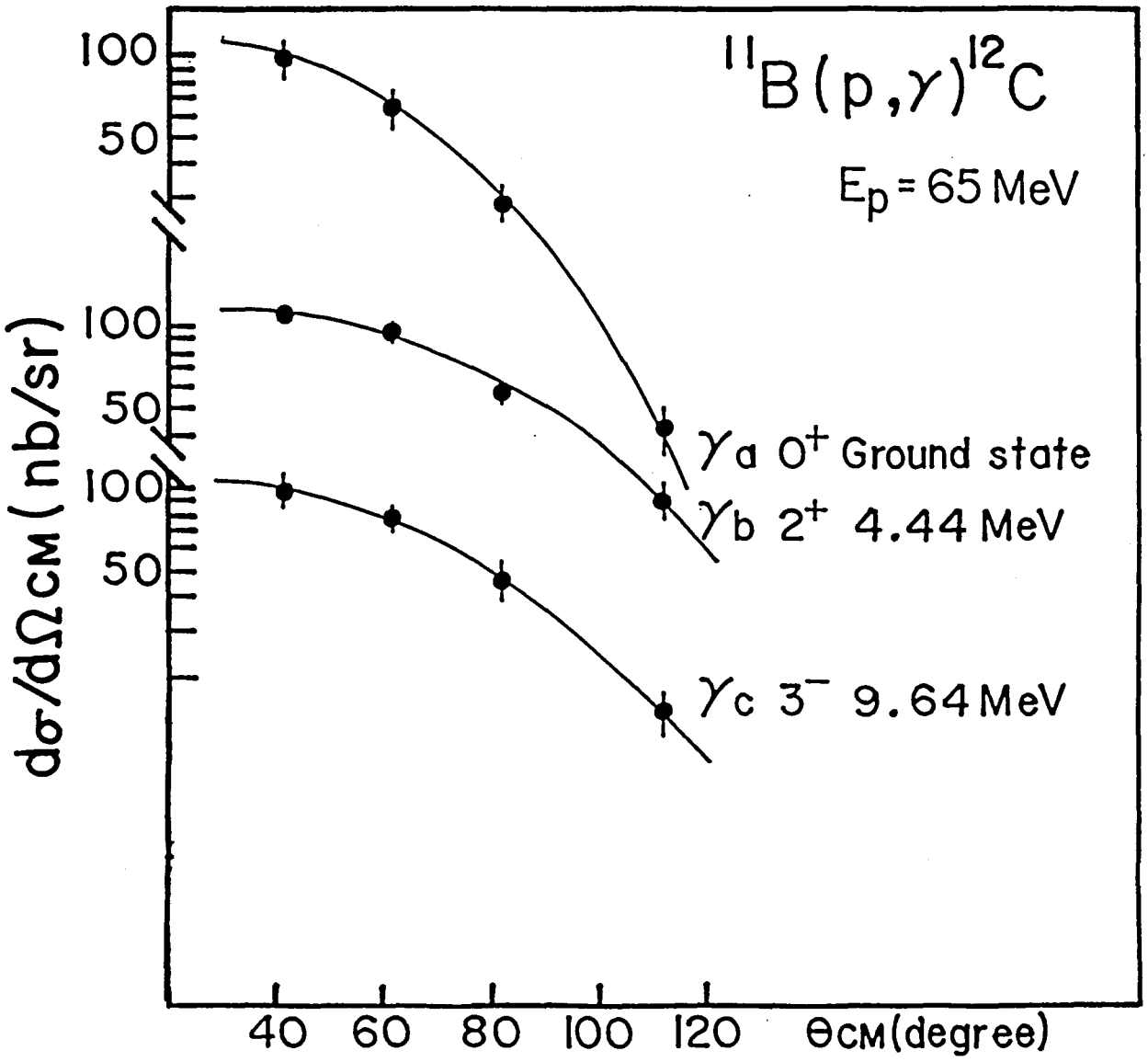
$^{11}B(p,\gamma)^{12}C$
$E_p = 65$ MeV
γ_a 0^+ Ground state
γ_b 2^+ 4.44 MeV
γ_c 3^- 9.64 MeV
$d\sigma/d\Omega_{CM}$ (nb/sr)
100
50
100
50
100
50
40
60
80
100
120
θ_{CM}(degree)

FIG. 4.5A

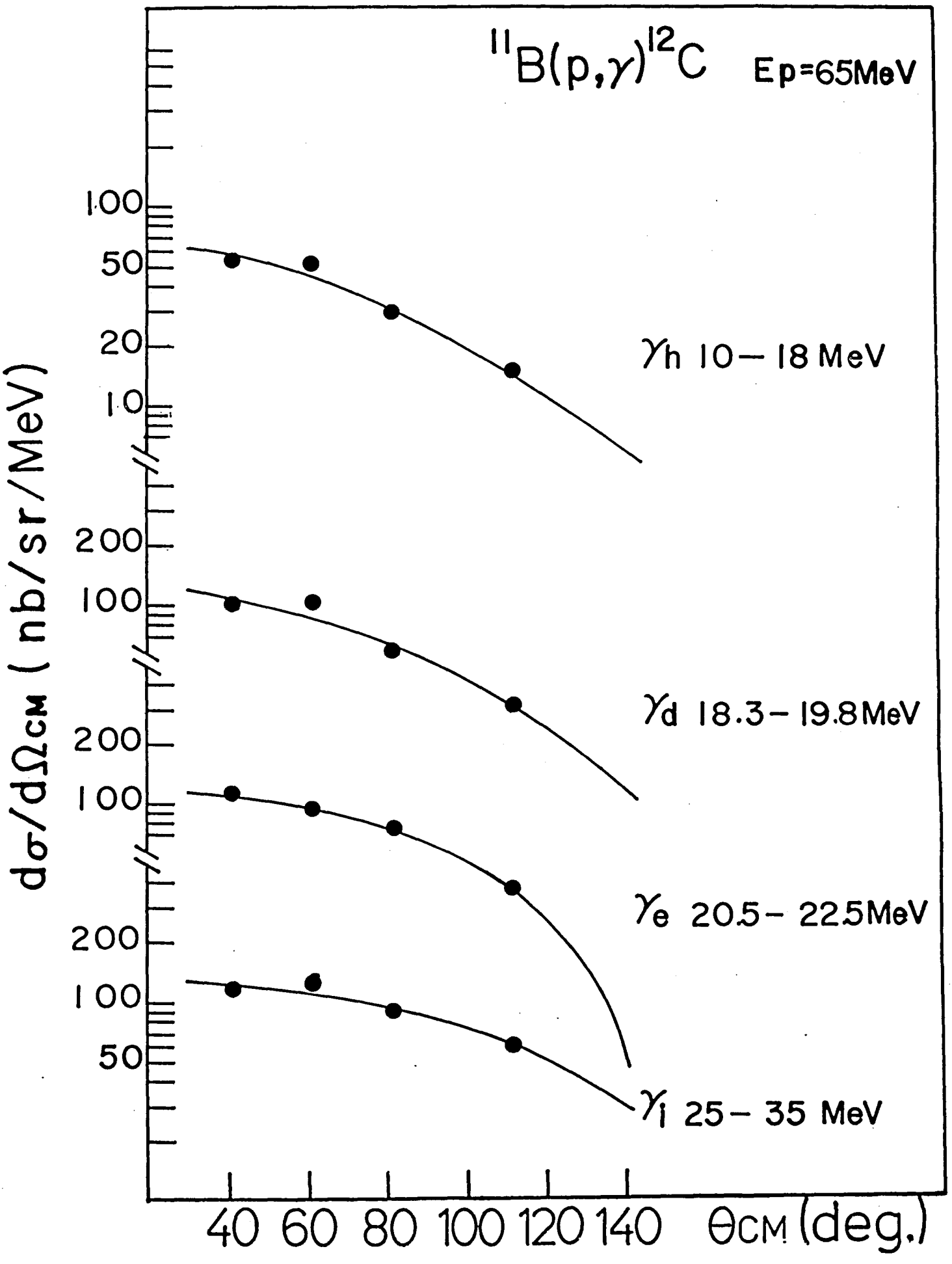
$^{11}B(p,\gamma)^{12}C$ Ep=65MeV
γ_h 10–18 MeV
γ_d 18.3–19.8MeV
γ_e 20.5–22.5MeV
γ_i 25–35 MeV
dσ/dΩcm (nb/sr/MeV)
100
50
20
10
200
100
200
100
200
100
50
40 60 80 100 120 140 θcm (deg.)

FIG. 4.5B

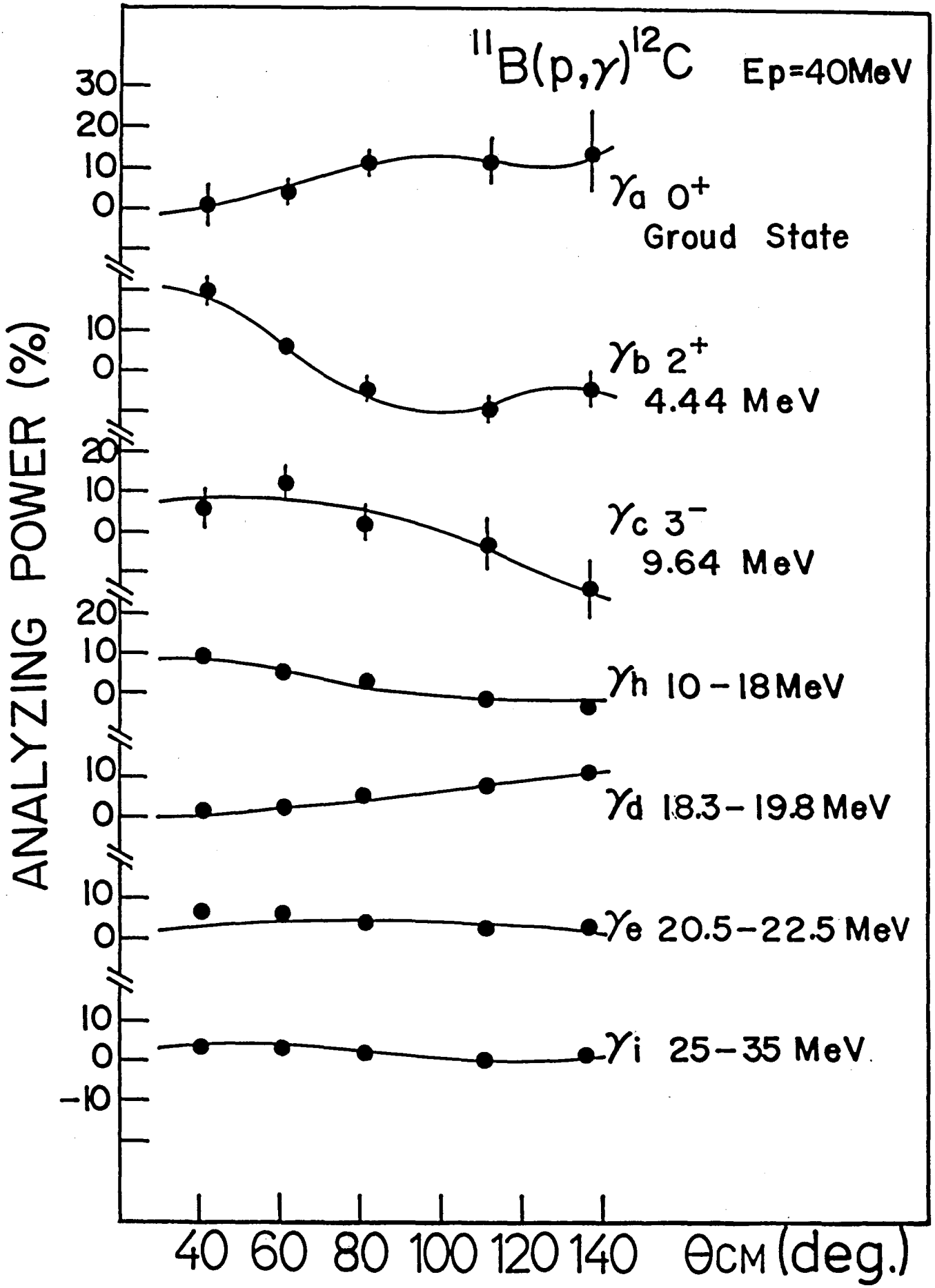
$^{11}B(p,\gamma)^{12}C$ Ep=40MeV
ANALYZING POWER (%)
30
20
10
0
10
0
20
10
0
20
10
0
10
0
10
0
10
0
-10
γ_a 0^+
Groud State
γ_b 2^+
4.44 MeV
γ_c 3^-
9.64 MeV
γ_h 10-18MeV
γ_d 18.3-19.8MeV
γ_e 20.5-22.5MeV
γ_i 25-35 MeV
40 60 80 100 120 140 θ_{CM} (deg.)

FIG. 4.6A

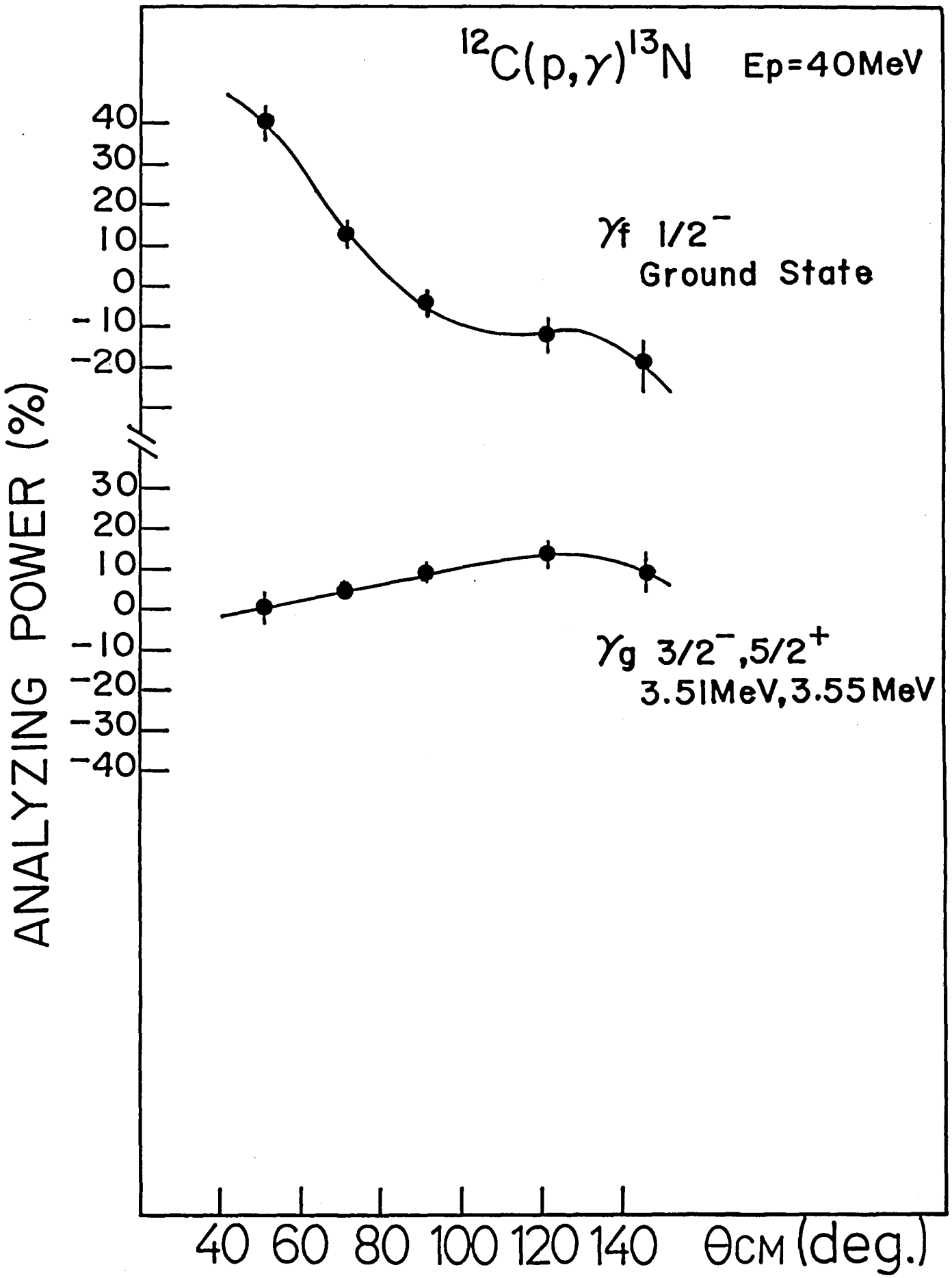
$^{12}C(p,\gamma)^{13}N$ Ep=40MeV
γ_f 1/2⁻
Ground State
γ_g 3/2⁻,5/2⁺
3.51MeV,3.55MeV
ANALYZING POWER (%)
40
30
20
10
0
-10
-20
30
20
10
0
-10
-20
-30
-40
40 60 80 100 120 140 θCM (deg.)

FIG. 4.6B

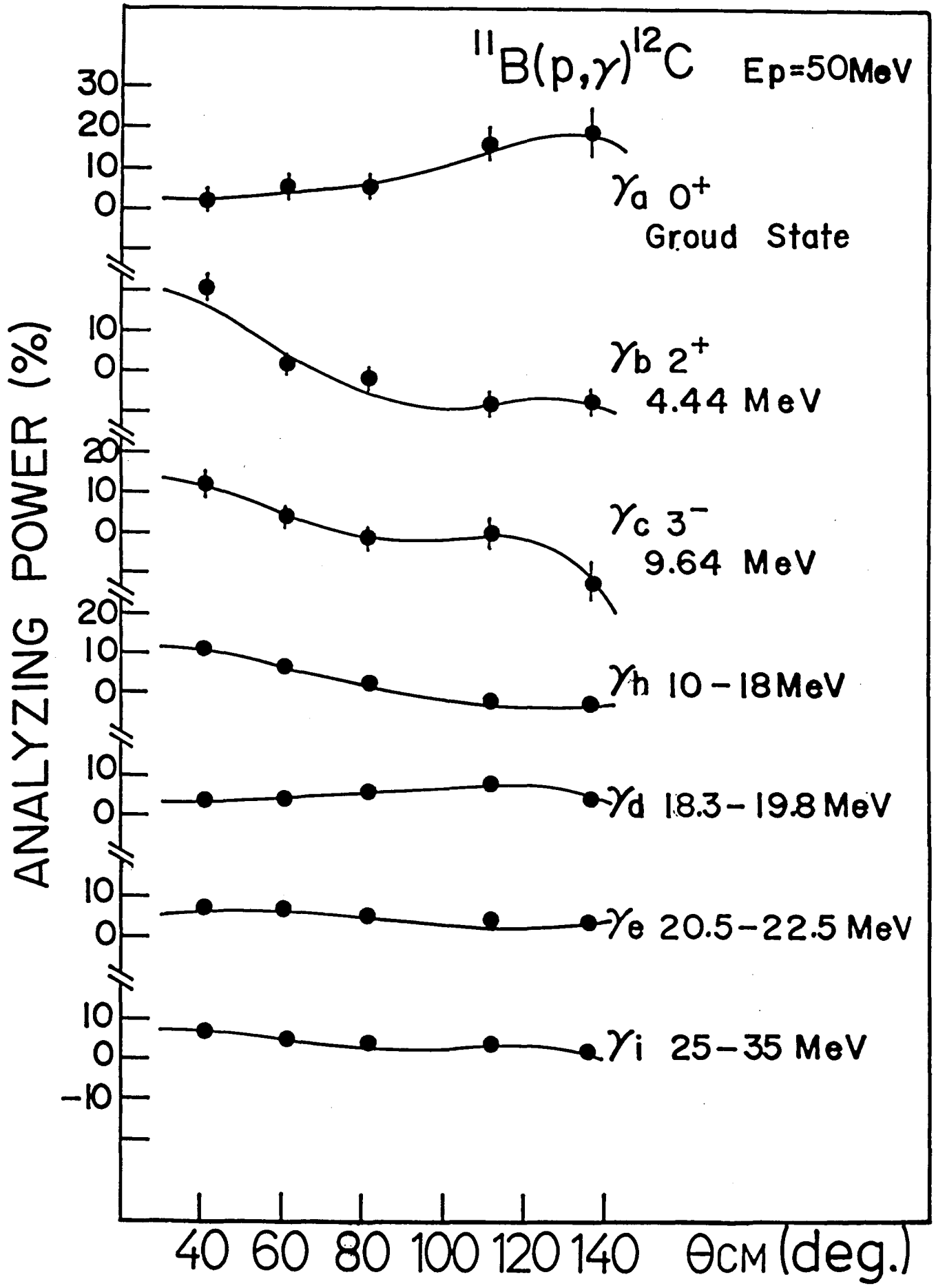
$^{11}B(p,\gamma)^{12}C$ Ep=50MeV
ANALYZING POWER (%)
30
20
10
0
10
0
20
10
0
20
10
0
10
0
10
0
10
0
-10
γ_a 0^+
Groud State
γ_b 2^+
4.44 MeV
γ_c 3^-
9.64 MeV
γ_h 10-18MeV
γ_d 18.3-19.8 MeV
γ_e 20.5-22.5 MeV
γ_i 25-35 MeV
40 60 80 100 120 140 θ_{CM} (deg.)

FIG. 4.7

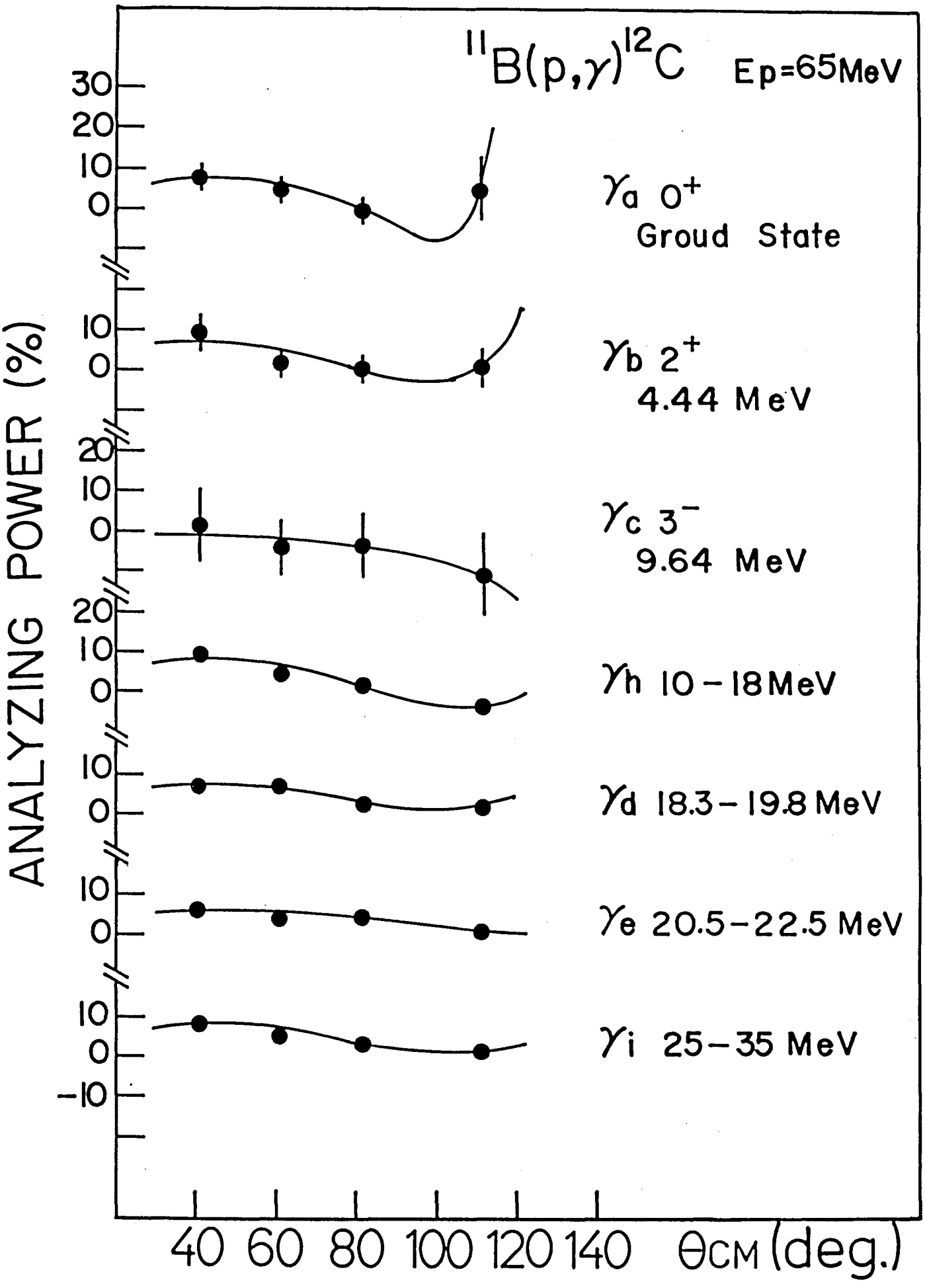
$^{11}B(p,\gamma)^{12}C$ Ep=65MeV
ANALYZING POWER (%)
30
20
10
0
10
0
20
10
0
20
10
0
10
0
10
0
10
0
-10
γ_a 0^+
Groud State
γ_b 2^+
4.44 MeV
γ_c 3^-
9.64 MeV
γ_h 10-18MeV
γ_d 18.3-19.8 MeV
γ_e 20.5-22.5 MeV
γ_i 25-35 MeV
40 60 80 100 120 140 θ_{CM} (deg.)

FIG. 4.8

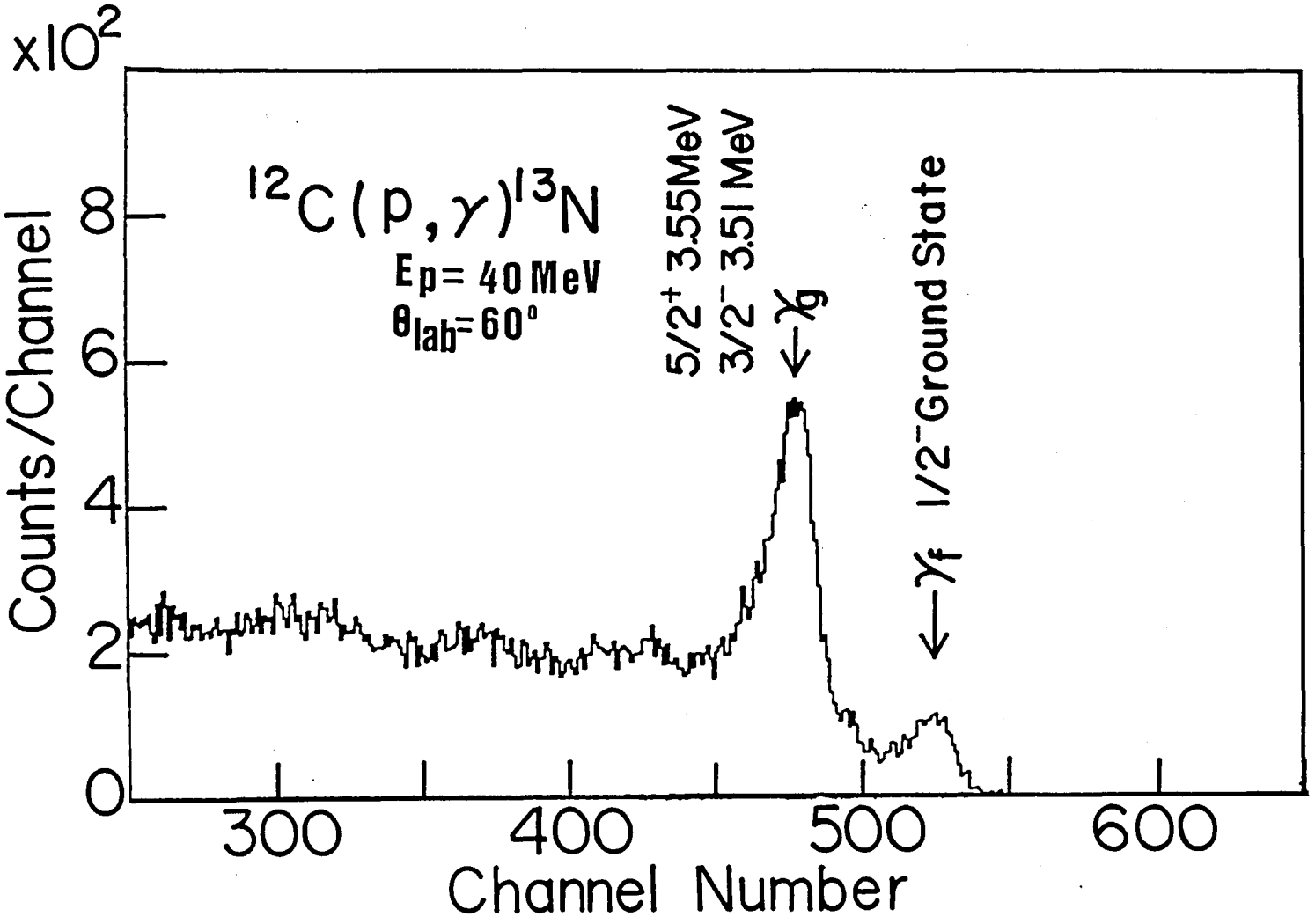
x10²
Counts/Channel
0
2
4
6
8
$^{12}C(p,\gamma)^{13}N$
Ep= 40 MeV
θ_{lab}= 60°
5/2⁺ 3.55MeV
3/2⁻ 3.51 MeV
← γ_g
← γ_f 1/2⁻Ground State
300
400
500
600
Channel Number

Fig. 4.9

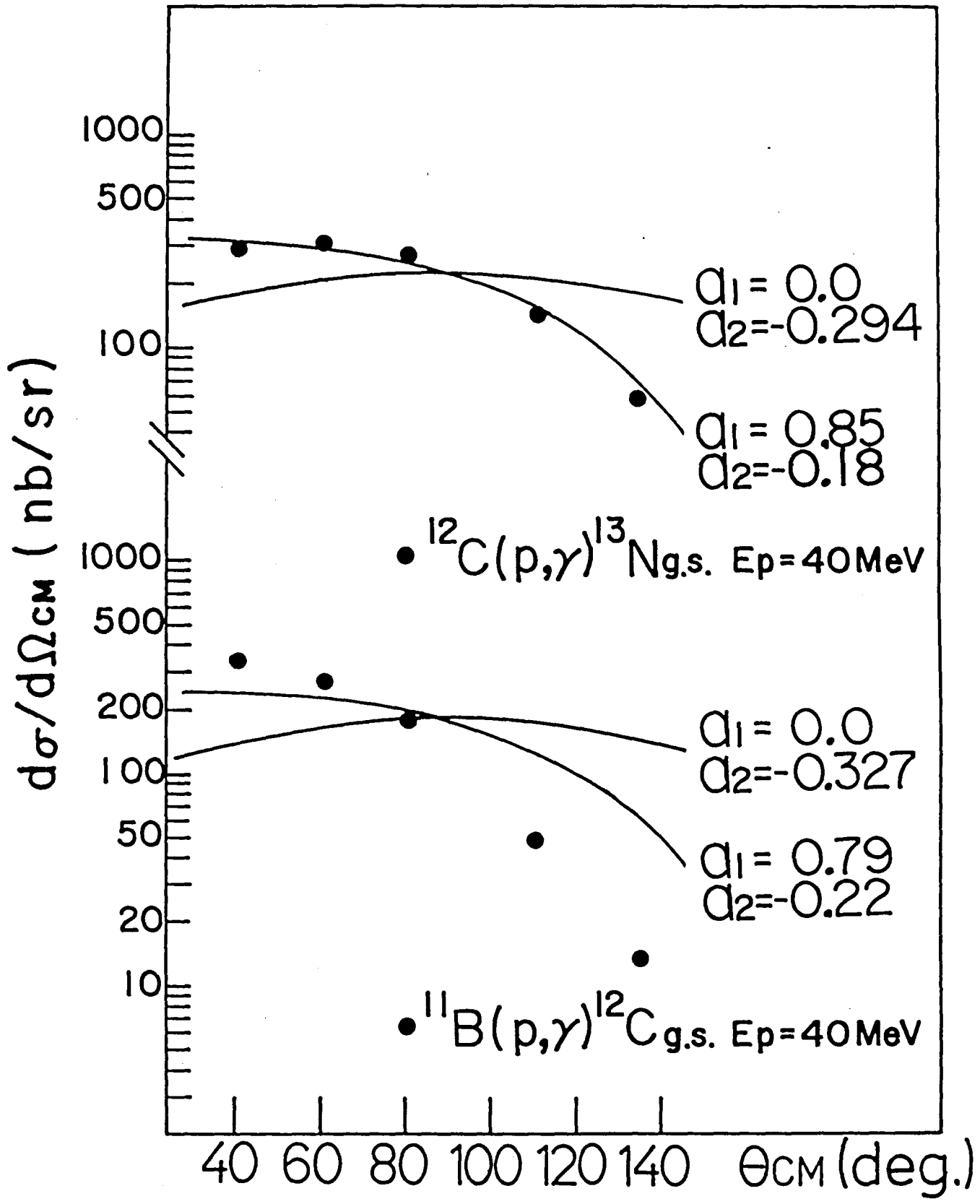
1000
500
100
1000
500
200
100
50
20
10
dσ/dΩcm (nb/sr)
a1 = 0.0
a2=-0.294
a1 = 0.85
a2=-0.18
12C(p,γ)13Ng.s. Ep=40MeV
a1 = 0.0
a2=-0.327
a1 = 0.79
a2=-0.22
11B(p,γ)12Cg.s. Ep=40MeV
40 60 80 100 120 140
θcm (deg.)

FIG. 4.10

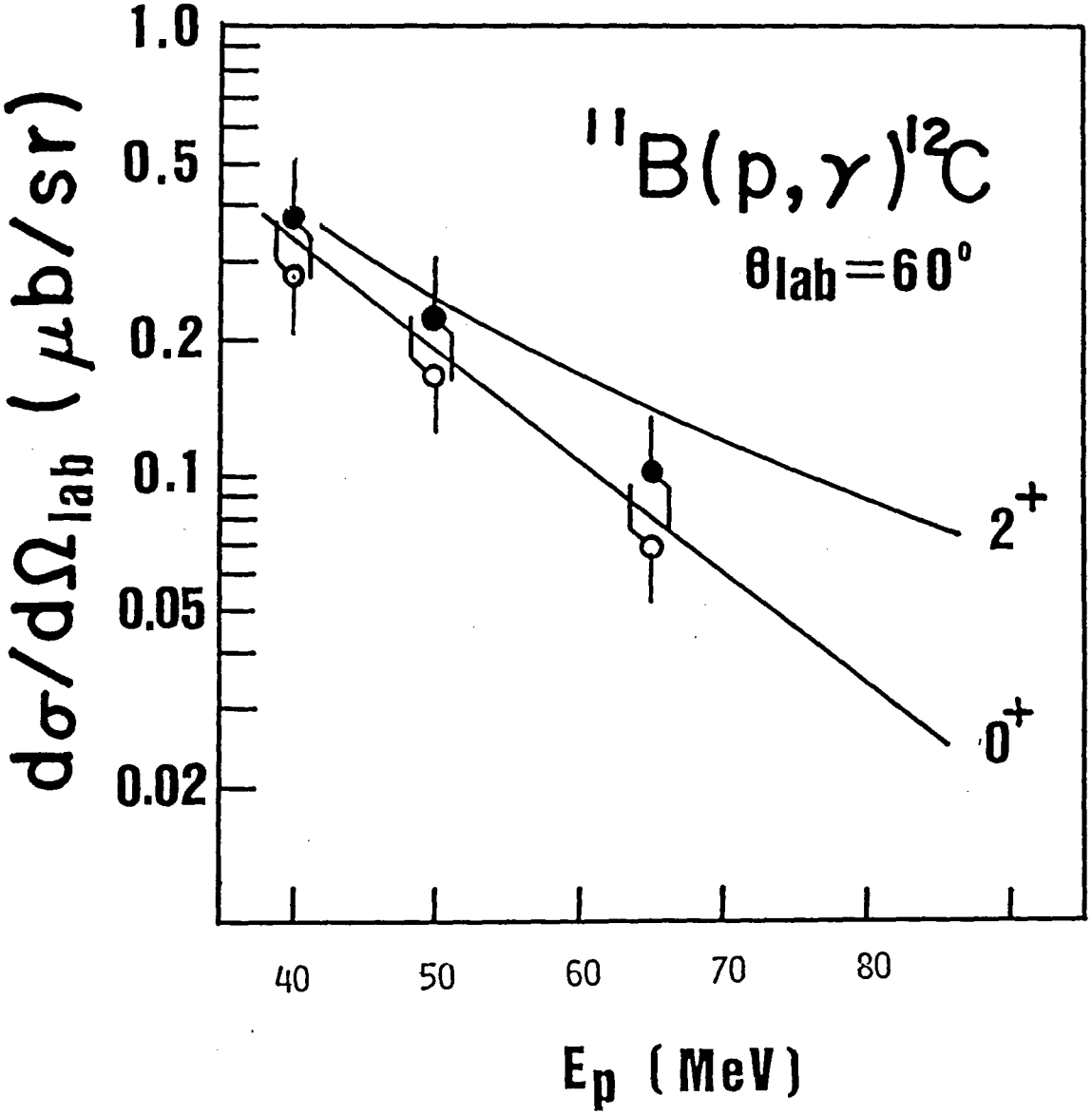
1.0
0.5
0.2
0.1
0.05
0.02
dσ/dΩlab (μb/sr)
11B(p,γ)12C
θlab=60°
2+
0+
40
50
60
70
80
Ep (MeV)

FIG. 4.11

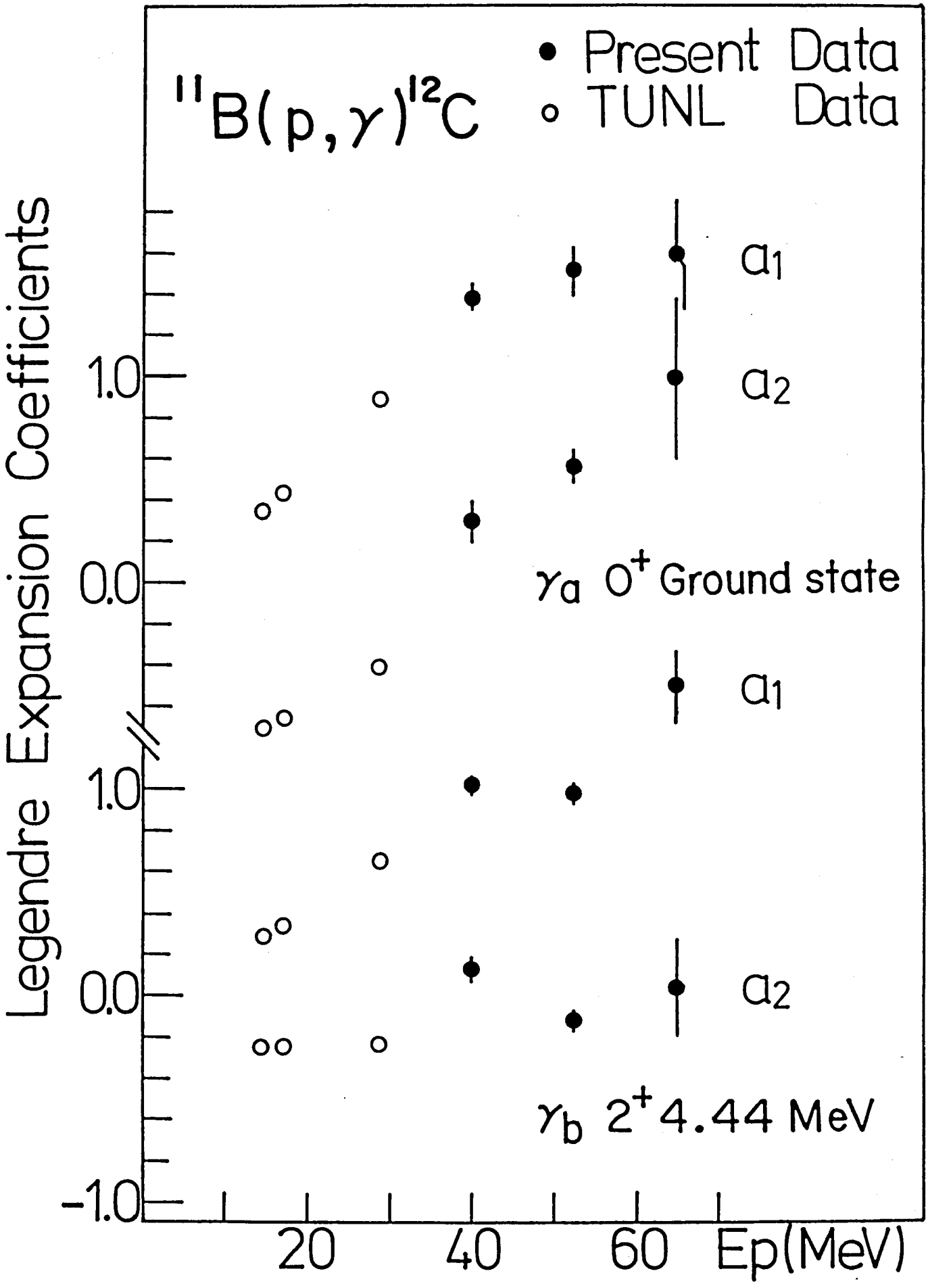
$^{11}B(p,\gamma)^{12}C$
Present Data
TUNL Data
Legendre Expansion Coefficients
1.0
0.0
1.0
0.0
-1.0
a_1
a_2
γ_a 0^+ Ground state
a_1
a_2
γ_b 2^+ 4.44 MeV
20
40
60
Ep(MeV)

FIG. 4.12

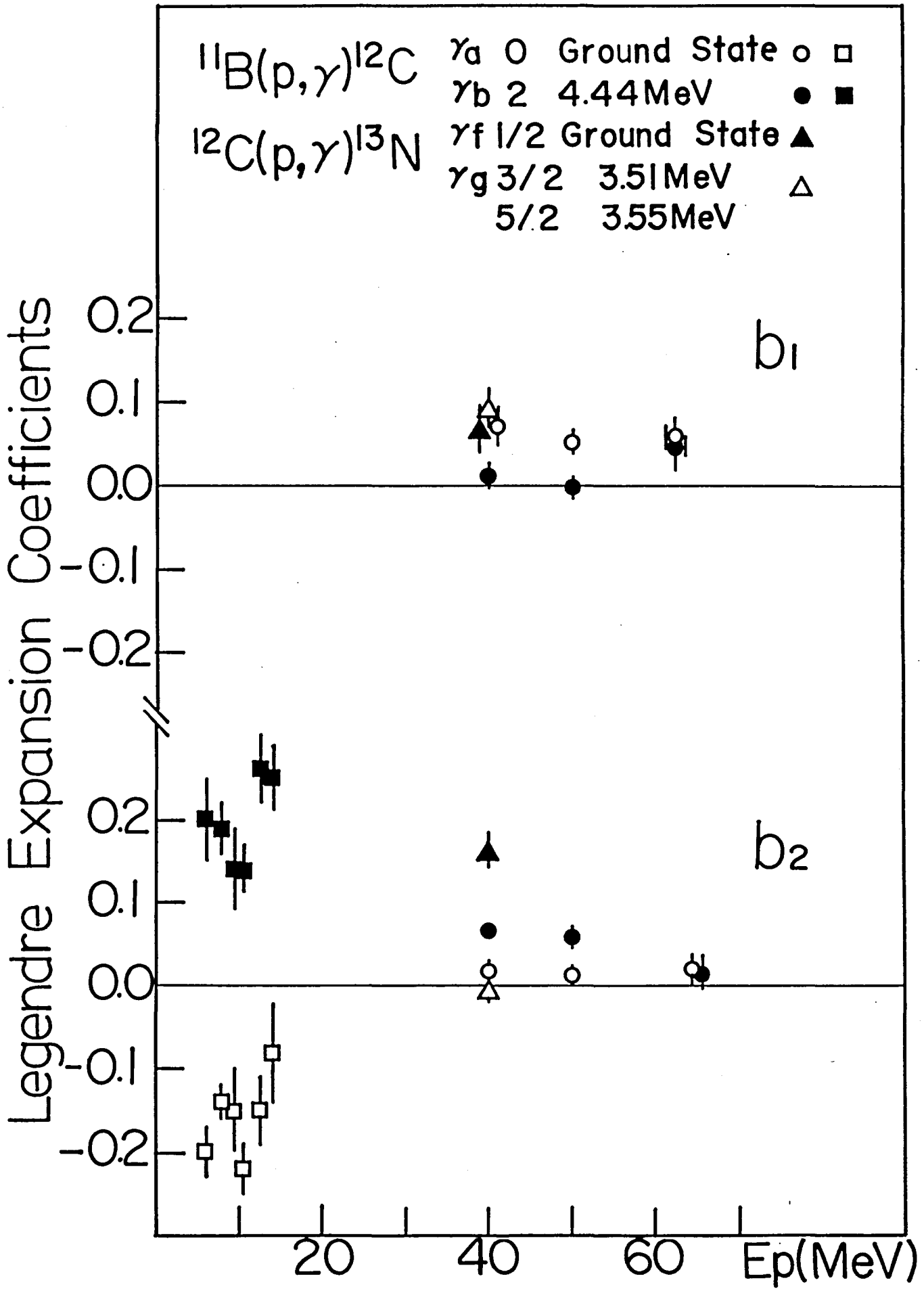
$^{11}B(p,\gamma)^{12}C$
$^{12}C(p,\gamma)^{13}N$
γ_a 0 Ground State
γ_b 2 4.44MeV
γ_f 1/2 Ground State
γ_g 3/2 3.51MeV
5/2 3.55MeV
Legendre Expansion Coefficients
b1
b2
0.2
0.1
0.0
-0.1
-0.2
20
40
60
Ep(MeV)

FIG. 4.13